A Micro-Mechanically Motivated Model for the Oxidative Ageing of Elastomers

Von der

Fakultät für Bauingenieurwesen und Geodäsie
der Gottfried Wilhelm Leibniz Universität Hannover
zur Erlangung des Grades

Doktor-Ingenieur (Dr.-Ing.)

genehmigte Dissertation von

Darcy Beurle, M.Eng.

Erscheinungsjahr 2020

Typeset in FreeSerif with LaTeX

Abstract

Oxidative ageing of elastomers is an irreversible process brought about by chemical reactions occuring within the molecular structure of a polymer network. Such reactions are facilitated by oxygen and are characterised by two competing reactions; chain scission and chain cross-linking. On the macro scale, the chain scission reaction can be observed in a stress softening of the material as the supporting polymer chains in the network are broken. In contrast, the chain cross-linking reaction increases the cross-link density to result in an overall stiffening of the material and the complex, deformation history permanent set effect. The scission and cross-linking reactions may not occur at the same rate, leading to an asymmetry in the degrees of stress softening, stiffening and of permanent set.

The link between the micro- and macro-scales for the description of oxidative ageing is the main focus of this dissertation. Several models exist in the literature for the modelling of oxidative ageing, but a micro-mechanical basis is missing and they instead rely on a phenomenological approach. Such phenomenological models can produce unphysical results and rely on simple exponential type equations for capturing the oxidative degradation of polymer networks. A micro-mechanical approach has the benefit of gaining deeper insight into the main drivers behind oxidative ageing and involve physically motivated material parameters.

Exploiting the statistical mechanical relationship between the shear modulus and the cross-link density, a network dynamics model capturing the oxidative ageing reactions is derived. A distinction is made between active cross-links that can support a load, and inactive cross-links which are unable to support a load. This results in a set of coupled non-linear differential equations describing the rate at which cross-links are created and destroyed. Using the two-network concept, a split of the polymer network is made into primary and secondary networks. Here the primary network is only permitted to decay and the secondary network is created stress-free with respect to the deformation at the time of creation. The mechanical model is based on the well-known microsphere model with modifications to include network dynamics.

Using the network dynamics model, a novel mapping procedure is introduced to capture the degradation state in terms of a dimensionless parameter. This mapping allows both the primary network to degrade and the continual decay of secondary networks to be captured. Capturing the permanent set effect is arguably the greatest challenge as the permanent set effect arises from the stress-free post-curing and the tension between different stress-free states inside the polymer network. Intermediate configurations are introduced continuously as cross-links are created in a given deformation frame. The pull-back operator allows convenient accumulation of these stresses in the reference configuration through an integral formulation. This allows very efficient computation of the secondary network stress and ensures the material model satisfies axioms of constitutive modelling.

Numerical tests and experiments were performed to showcase the strengths of the modelling approach including simple uniaxial tests and finite element simulations. A comparison of the proposed model with the state-of-the-art model demonstrates clear improvements in the modelling fidelity.

Funding: This research was funded by the German Research Foundation / Deutsche Forschungsgemeinschaft (DFG) through the International Research Training Group (IRTG) 1627.

Keywords: Oxidative ageing; Polymer dynamics; Microsphere model; Experimental oxidative ageing; Finite element method; Chain scission; Chain cross-linking; Permanent set

Zusammenfassung

Die oxidative Alterung von Elastomeren ist ein irreversibler Prozess, der durch chemische Reaktionen innerhalb der Molekularstruktur eines Polymernetzwerks hervorgerufen wird. Solche Reaktionen werden durch Sauerstoff ermöglicht und zeichnen sich durch zwei konkurrierende Reaktionen aus: Kettenspaltung und Kettenvernetzung. Auf der Makroskala kann die Kettenspaltungsreaktion bei einer Spannungserweichung des Materials beobachtet werden, da die tragenden Polymerketten im Netzwerk gebrochen werden. Im Gegensatz dazu erhöht die Kettenvernetzungsreaktion die Vernetzungsdichte, um eine Gesamtverstärkung des Materials und die Daueraushärtung zu erreichen. Die Spalt- und Vernetzungsreaktionen verlaufen möglicherweise nicht mit gleicher Geschwindigkeit, was zu einer Asymmetrie in den Graden der Spannungserweichung, Versteifung und des Dauereinsatzes führt.

In der Literatur gibt es mehrere Modelle zur Modellierung der Alterung, aber eine mikromechanische Grundlage fehlt und sie stützen sich stattdessen auf einen phänomenologischen Ansatz. Solche Modelle können unphysikalische Ergebnisse liefern und basieren auf einfachen Exponentialgleichungen zur Erfassung des oxidativen Abbaus von Polymernetzwerken. Ein mikromechanischer Ansatz hat den Vorteil, dass er einen tieferen Einblick in die Haupttreiber der oxidativen Alterung ermöglicht und physikalisch motivierte Materialparameter einbezieht.

Unter Ausnutzung der statistisch-mechanischen Beziehung zwischen dem Schermodul und der Vernetzungsdichte wird ein netzwerddynamisches Modell abgeleitet, das die oxidativen Alterungsreaktionen erfasst. Man unterscheidet zwischen aktiven Querverbindungen, die eine Last tragen können, und inaktiven Querverbindungen, die eine Last nicht tragen können. Dies führt zu einem Satz gekoppelter nichtlinearer Differentialgleichungen, die die Geschwindigkeit beschreiben, mit der Vernetzungen erzeugt und zerstört werden. Mit dem Zwei-Netzwerk Konzept wird eine Aufteilung des Polymernetzwerks in primäre und sekundäre Netzwerke vorgenommen. Dabei darf das primäre Netzwerk nur zerfallen und das sekundäre Netzwerk wird in Bezug auf die Verformung zum Zeitpunkt der Entstehung spannungsfrei aufgebaut. Das mechanische Modell basiert auf dem bekannten Microsphere-Modell mit Modifikationen zur Einbeziehung der Netzdynamik.

Mit Hilfe des Netzwerkdynamikmodells wird ein neuartiges Mapping-Verfahren eingeführt, um den Degradationszustand in Form eines dimensionslosen Parameters zu erfassen. Diese Zuordnung ermöglicht es, sowohl das primäre Netzwerk zu degradieren als auch den kontinuierlichen Abbau von sekundären Netzwerken zu erfassen. Die größte Herausforderung ist die Erfassung des Permanent Set Effektes, da der Permanent Set Effekt durch die spannungsfreie Nachhärtung und die Spannung zwischen verschiedenen spannungsfreien Zuständen innerhalb des Polymernetzwerks entsteht. Zwischenkonfigurationen werden kontinuierlich eingeführt, da in einem gegebenen Verformungsrahmen Querverbindungen entstehen. Der Pull-Back-Operator ermöglicht eine Akkumulation dieser Spannungen in der Ausgangskonfiguration durch eine integrierte Formulierung.

Numerische Tests und Experimente wurden durchgeführt, um die Stärken des unterschiedlichen Modellierungsansatzes aufzuzeigen, einschließlich einfacher uniaxialer Tests und Finite Elemente Simulationen. Ein Vergleich des vorgeschlagenen Modells mit dem neuesten Modell zeigt deutliche Verbesserungen in der Modellierungstreue.

Stichworte: Oxidative Alterung; Polymer Dynamik; Microsphere Modell; Alterung Versuch; Finite Elemente Methode; Kettenspaltung; Vernetzung; Restkrümmung

Contents

List of figures

List of tables

Chapter 1

Introduction

Elastomers have garnered considerable attention from researchers over the course of the early twentieth century due to their peculiar mechanical and chemical properties. Rubber is a naturally occurring elastomer originally extracted from the latex-containing sap of the tree *Hevea Braziliensis*. It was later synthesised on an industrial scale during the second world war due to difficulties obtaining raw materials from South East Asia. Elastomers have a comparatively recent history as a technical engineering material compared to their metallic counterparts, but now exist as critical components in domestic, automotive, aerospace and manufacturing industries as seals and provide vibration isolation [Treloar, 1975]. At the root of their success is their formability, customisability and large strain deformability. With a change of constituents during production, such as additional sulfur during mixing, elastomers can either be very soft and flexible, hard and strong, or anywhere in between depending on the demands of the application [Brown, 2007].

At the molecular level, elastomers are comprised of long chains of repeated polymer units which consist primarily of carbon-carbon bonds with various side-groups. Natural rubber is depicted in Figure 1.1, where single and double carbon-carbon bonds and methyl side-grounds are visible. Typically polymers are presented as a representative unit with n repeat units. These single polymer chains are sparsely cross-linked to neighbouring chains and these cross-links prevent chains from simply sliding past one another. The chains are randomly arranged to form a complex three-dimensional network topology.
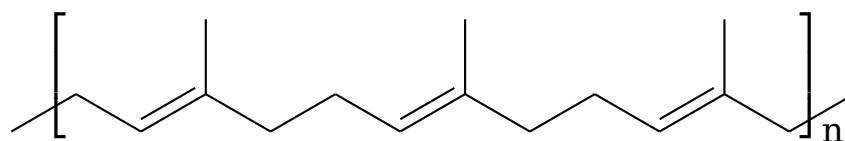
Figure 1.1: Natural rubber polymer unit

Technical elastomers often include filler particles to inhibit the motion of the chains thereby increasing the strength of the material. The polymers in filled elastomers interact with the filler particles leading to complex micro-scale behaviour. These and other micro-scale phenomena lead to several effects such as the Mullins effect, viscoelasticity, shrinkage, stress relaxation, stiffening, permanent set and crystallisation [Treloar, 1975, Maiti et al., 2014]. To compound the complexity, the polymer network undergoes changes over vastly different time scales of seconds to years.

The early constitutive modelling efforts of rubber failed due to a fundamentally incorrect approach. Researchers at the time did not exploit the curious entropic properties of elastomer deformation in their modelling approach. Taking this phenomena into account, the first successful attempts such as the well-known *entropy elasticity* model used to describe the force generated by a network of polymer chains under

load were realised in the early twentieth century. This was followed by the development of several important models including Gaussian and non-Gaussian chain theories [Treloar, 1944, Kuhn and Grün, 1942, Kuhn, 1952]. The force response of a non-idealised elastomer is not only due to the applied load, but also the interaction of the chains with other constituents in the elastomer leading to undesirable and complicated material behaviour.

A significant drawback of elastomers in practical applications is the physical degradation throughout the product lifetime, leading to an early and sometimes catastrophic failure. The reader is likely familiar with the degradation process where an elastomer becomes stiff and loses its highly sought-after elasticity. Examples of technical elastomers are encountered in several aspects of life such as tyres, O-rings, gaskets, surrounds in loudspeaker drivers and machinery mounting hardware. The diligent design engineer needs to account for the changes in material performance over the intended service life of the product to maintain product reliability.

There are two broadly defined categories of ageing; physical and chemical. Physical ageing involves the physical rearrangement of polymer bonds occurring over a smaller time scale and reversal is possible with a careful increase in temperature [Lion et al., 2011]. In contrast, chemical ageing involves topological changes to the polymer network that are irreversible, caused by oxidation and catalysed by temperature [Budzien et al., 2008]. The two main reactions that occur are scission and secondary cross-linking. Scission leads to an observable stress softening of the material, similar to viscoelastic effects, however it is irreversible and occurs over a longer period of time. Secondary cross-linking, or post-curing, leads to additional cross-linking thereby increasing the stiffness of the material over time and a corresponding loss of elasticity. A constitutive model of chemical ageing considering the micro-mechanical behaviour of polymers is the topic of this dissertation.

A brief exposé on the fundamentals of solid mechanics and the finite element method is presented in Chapter 2. Mechanical constitutive models commonly applied to model the finite deformation behaviour of elastomers are introduced in Chapter 3. An explanation of the mechanisms responsible for chemical ageing is given in Chapter 4, followed closely by a concise review of existing chemical ageing models. This provides the setting required to present the theoretical developments of a new constitutive model motivated by the micro-mechanical aspects of elastomer ageing. A series of numerical and experimental tests are presented and critically discussed in Chapters 5 and 6. Finally, a summary of the work and an outlook will be provided at the conclusion of this dissertation.

1.1   Polymer chemistry

The molecular polymer structure is responsible for the macroscopic behaviour of elastomer components. Understanding the molecular basis, at least from an engineering perspective, is advantageous for the development of a micro-mechanically motivated constitutive model. Elastomers consist of a large number of polymer chains sparsely cross-linked to form a complex network, involving interactions with neighbouring polymers and additives such as filler particles and anti-oxidants. The number of cross-links restrict the available configurations to the chain and thereby decrease the flexibility of the chains. Elastomers can be categorised into two main groups; thermosetting and themoplastic elastomers. Thermoplastic elastomers will soften upon heating and thermosetting polymers are constrained by their network and degrade at elevated temperature [Callister, 2007]. In this dissertation, only the oxidative ageing of thermosetting polymers will be examined.

An enormous amount of flexibility in the formulation of polymers has led to numerous types of elastomers, each with their own set of properties and mechanical performance. Natural rubber (NR) has already been introduced by means of Figure 1.1. As the name suggests, NR is derived from natural latex trees. A

popular synthetic elastomer is styrene-butadiene rubber (SBR), see Figure 1.2, and it is commonly found in pneumatic tyres due to its high abrasion resistance. Polymers are not inert materials and it has long been
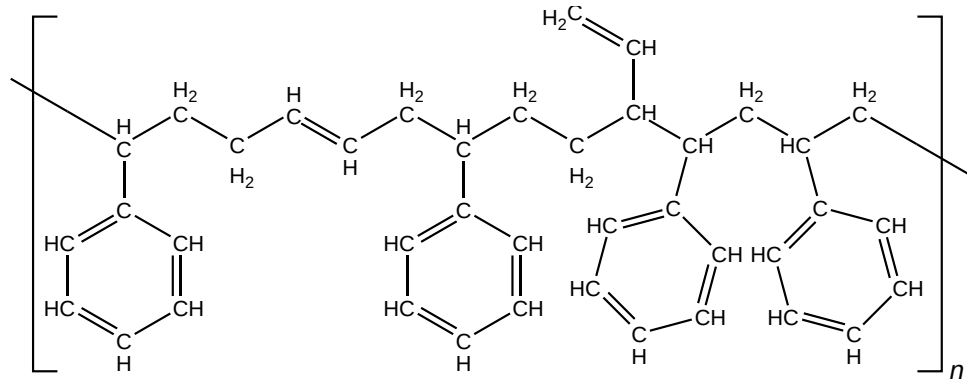
Figure 1.2: A single unit of a styrene-butadiene polymer. Note the additional aromatic side-groups cf. natural rubber

known that they are subject to numerous forms of attack due to environmental conditions, including immersion in reactive chemicals and exposure to oxygen and radiation [Williams, 1926]. The mechanisms behind oxidative ageing were first proposed by [Bolland, 1949] and are reproduced in [Gryn'ova et al., 2011] as

$$\text{Initiation} \begin{cases} \text{Polymer} \xrightarrow{\text{Initiator}} \text{R}^{\bullet} \\ \text{R}^{\bullet} \xrightarrow{\text{Fragmentation \& rearrangement}} \text{R}_{\text{X}}^{\bullet} \end{cases} \tag{1.1}$$

$$\text{Propagation} \begin{cases} \text{R}^{\bullet} + \text{O}_2 \longrightarrow \text{RO}_2^{\bullet} \\ \text{RO}_2^{\bullet} + \text{RH} \longrightarrow \text{ROOH} + \text{R}^{\bullet} \end{cases} \tag{1.2}$$

$$\text{Chain branching} \begin{cases} \text{ROOH} \longrightarrow \text{RO}^{\bullet} + \text{HO}^{\bullet} \\ 2\,\text{ROOH} \longrightarrow \text{RO}_2^{\bullet} + \text{RO}^{\bullet} + \text{H}_2\text{O} \\ \text{RO}^{\bullet} + \text{RH} \longrightarrow \text{ROH} + \text{R}^{\bullet} \\ \text{HO}^{\bullet} + \text{RH} \longrightarrow \text{R}^{\bullet} + \text{H}_2\text{O} \end{cases} \tag{1.3}$$

$$\text{Termination} \begin{cases} 2\,\text{RO}_2^{\bullet} \longrightarrow \text{Inert products} \\ \text{RO}_2^{\bullet} + \text{R}^{\bullet} \longrightarrow \text{ROOR} \\ 2\,\text{R}^{\bullet} \longrightarrow \text{R}{-}\text{R} \end{cases} \tag{1.4}$$
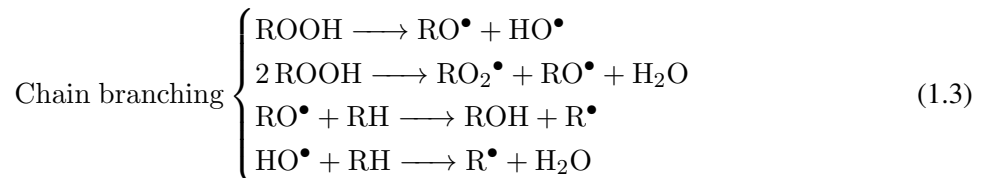
Note that a · represents a radical (an unpaired, and unbalanced, electron) which is extremely reactive and seeks to lower its energy through an additional chemical reaction. The classic mechanism of auto-oxidation in elastomers consists of four main stages. In the initiation stage, free radicals are created which can then fragment and / or rearrange. During propagation the free radicals react with other compounds such as oxygen or polymer end groups to form new free radicals. Chain branching leads to the formation of new chain branches without consuming the free radicals, and the termination stage consists of the combination of two free radicals to form nonreactive species.

The Bolland reactions can be described by a set of differential equations [Kreiselmaier et al., 2014] to obtain a high-fidelity model of the reaction process. Resolving the chemical reaction in its entirety is computationally expensive and a surrogate model will be introduced in a subsequent section to avoid the tedium of resolving each reaction, while retaining the first-order effects of oxidative ageing on the polymer network.

In this work the complexities of specific formulations will not be resolved explicitly. A simplified model of the network will be used instead in order to demonstrate a proof-of-concept. These assumptions can be revised with formulation specific reaction kinetics if so desired.

Chapter 2

Continuum mechanics

Continuum mechanics is the mathematical framework concerned with the description of motion, deformation and stress of a continuously defined material under external influences. This theory finds several applications in fluid and solid mechanics, where the medium obeys classical Newtonian mechanics. In this chapter, a concise exposition of finite-strain theory for solid bodies will be provided. The relevant deformation and stress measures required for understanding the constitutive models of elastomer materials will appear alongside the main concepts. What is presented in this chapter only scratches the surface of this vast and interesting field. The reader is referred to [de Souza Neto et al., 2011, Holzapfel, 2002, Belytschko et al., 2013, Wriggers, 2008] for further information.

2.1 Kinematics

Consider the deformation of a solid body in a Cartesian frame, see Figure 2.1. Let the body $\mathcal{B} \subset \mathbb{R}^3$ be the reference configuration and $\phi(\boldsymbol{X}, t) : \mathcal{B} \to \mathbb{R}^3$ be the non-linear deformation map from the reference to the current configuration $\boldsymbol{x} = \phi_t(\boldsymbol{X}) \in \phi_t(\mathcal{B})$, defined at some time t where $\{t \in \mathbb{R} \mid t > 0\}$. The displacement $\boldsymbol{u} \subset \mathbb{R}^3$ and the deformation gradient are defined as

$$\boldsymbol{u} = \boldsymbol{x} - \boldsymbol{X} \tag{2.1}$$
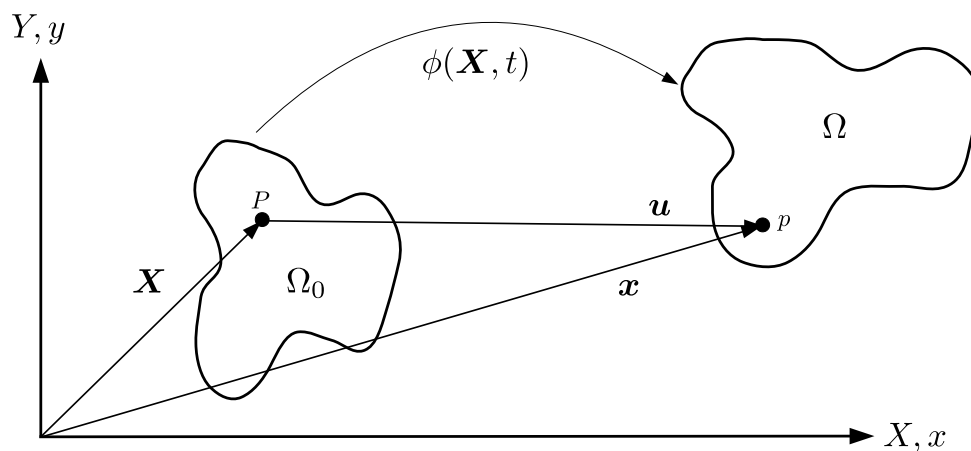
Figure 2.1: Initial and current configuration of a deformed body

and

$$\mathbf{F}(\boldsymbol{X}) = \nabla_{\boldsymbol{X}} \phi_t(\boldsymbol{X}) = \frac{\partial \phi_t(\boldsymbol{X})}{\partial \boldsymbol{X}} \tag{2.2}$$

respectively, where $\nabla_{\boldsymbol{X}}$ is the spatial gradient operator with respect to the reference coordinates. The Jacobian of the mapping is given as

$$J(\boldsymbol{X}) = \det \mathbf{F}(\boldsymbol{X}) > 0 \tag{2.3}$$

which must be strictly positive for the mapping to be valid [Miehe, 1994]. The deformation gradient is a two-point tensor, linking the reference and current configurations. This attractive property of the deformation gradient will be indispensable throughout the derivation of the material model.

In this dissertation, quantities of interest such as stress and strain are, for the most part, formulated in the current configuration, otherwise known as the spatial or Eulerian setting. The spatial velocity gradient tensor is defined as the gradient of the velocity field $\boldsymbol{v}$

$$\boldsymbol{l} = \frac{\partial \boldsymbol{v}}{\partial \boldsymbol{x}} = \dot{\mathbf{F}} \cdot \mathbf{F}^{-1} \, , \tag{2.4}$$

where $\cdot$ represents the single tensor contraction, commonly known as the matrix-matrix product when applied to second order tensors. The velocity gradient plays an important role when constitutive theory in the spatial setting is introduced and defined as the symmetric part of the rate of deformation tensor viz.,

$$\mathbf{d} = \operatorname{sym}(\boldsymbol{l}) = \frac{1}{2}\left(\boldsymbol{l} + \boldsymbol{l}^{\mathrm{T}}\right) \, . \tag{2.5}$$

Various strain measures defined in the reference configuration will be used throughout later derivations as required. The right Cauchy-Green deformation tensor is a symmetric second order tensor grounded in the reference configuration and is defined as

$$\mathbf{C} = \mathbf{F}^{\mathrm{T}} \cdot \mathbf{F} \, , \tag{2.6}$$

and the left Cauchy-Green tensor is given by

$$\mathbf{b} = \mathbf{F} \cdot \mathbf{F}^{\mathrm{T}} \, . \tag{2.7}$$

These two mathematically defined deformation measures do not provide a suitable strain measure as they are non-zero when the body is not deformed. A mathematically derived strain tensor, called the Green-Lagrange strain tensor, is defined as

$$\mathbf{E} = \frac{1}{2}\left(\mathbf{C} - \mathbf{1}\right) \tag{2.8}$$

which assumes a value of zero when the body is at rest. The linearisation of (2.8) gives the small-strain Euler strain tensor. It should be noted that transformations between these strain measures is possible through the Lie derivative and the deformation gradient and allows a certain degree of flexibility when selecting a deformation or strain measure.

2.2 Stress measures

In response to an externally applied load, a restrained body in a quasi-static setting will deform and develop internal stresses to resist the applied load. Stress measures are second order tensors and are formulated with respect to a particular configuration. In the spatial setting, the Cauchy stress (also termed *true stress*) is used with the rate of deformation as these are work-conjugate [Belytschko et al., 2013]. An important stress measure in the spatial setting is the Kirchhoff (or weighted Cauchy) stress. It is related to the Cauchy stress through the Jacobian J defined in (2.3), viz.,

$$\boldsymbol{\tau} = J\boldsymbol{\sigma} \, . \tag{2.9}$$

In the Lagrangian formulation, the second Piola-Kirchhoff stress $\mathbf{S}$ is heavily used as the work-conjugate stress tensor to the Green-Lagrange strain tensor $\mathbf{E}$. The second Piola-Kirchhoff stress can be readily transformed between manifolds through a push-forward operation. Both $\mathbf{S}$ and $\boldsymbol{\sigma}$ are attractive stress measures due to their symmetry, which make their usage in a finite element framework computationally advantageous compared to non-symmetric stress measures. Note that the symmetry of $\boldsymbol{\tau}$ follows trivially from (2.9).

Stress is typically related to the strain through an appropriate constitutive model. These relationships act to close the governing equations in continuum mechanics and are specific to the material being modelled. The use of the Cauchy stress incurs additional complexity with the addition of stress-rates that will become apparent when introducing constitutive models, which is a major topic in itself and it will be discussed in further detail in Section 2.5.

2.3 Conservation equations

There are four balance equations that are used in continuum mechanics

1. Mass conservation

2. Energy conservation

3. Conservation of angular momentum

4. Conservation of linear momentum

and these equations are supplemented by the Clausius-Duhem inequality to ensure the laws of thermodynamics are not violated. In this section, the conservation laws will be introduced however a detailed derivation is relegated to [Belytschko et al., 2013]. In this thesis, the Eulerian framework will be used and later the Updated Lagrange Finite Element Method will be employed to discretise the resulting equations.

2.3.1 Mass conservation

Mass is defined as the integral over space and time of the density ρ

$$m(\Omega) = \int_\Omega \rho(\boldsymbol{x}, t) \, \mathrm{d}\Omega \, , \tag{2.10}$$

where Ω is the volume. Ensuring that mass remains constant requires that

$$\frac{\mathrm{D}m}{\mathrm{D}t} = \frac{\mathrm{D}}{\mathrm{D}t} \int_\Omega \rho \, \mathrm{d}\Omega = 0 \, , \tag{2.11}$$

holds. Using the Reynold's transport theorem in the Eulerian context yields

$$\int_{\Omega} \left(\frac{\mathrm{D}\rho}{\mathrm{D}t} + \rho \nabla \boldsymbol{v} \right) \mathrm{d}\Omega = 0 \,, \tag{2.12}$$

where $\boldsymbol{v}$ is the velocity field. This implies that

$$\frac{\mathrm{D}\rho}{\mathrm{D}t} + \rho \nabla \boldsymbol{v} = 0 \,. \tag{2.13}$$

The mass conservation equation is not directly used in solid mechanics, however it is provided for completeness and is used heavily in the description of fluid behaviour.

2.3.2 Energy conservation

Conservation of energy is derived from the first law of thermodynamics, which states that the rate of change of the total energy (internal and kinetic energy) is equal to the work done by external forces and any changes due to heat flow

$$\mathcal{P}^{\text{int}} + \mathcal{P}^{\text{kin}} = \mathcal{P}^{\text{ext}} + \mathcal{P}^{Q} \tag{2.14}$$

where $\mathcal{P}^{\text{int}}$ is the internal power, $\mathcal{P}^{\text{kin}}$ is the kinetic energy, $\mathcal{P}^{\text{ext}}$ is the external load power and $\mathcal{P}^{Q}$ is the heat power. After introduction of some definitions and algebraic manipulations, the scalar conservation equation is given by

$$\rho \frac{\mathrm{D}w^{int}}{\mathrm{D}t} = \mathbf{d} : \boldsymbol{\sigma} - \nabla \cdot \boldsymbol{q} + \rho s \,, \tag{2.15}$$

where $\boldsymbol{q}$ is the heat flux area and s is the heat supplied to the body [Belytschko et al., 2013]. This conservation equation is provided for completeness and is not directly used in the material model, but rather through the Clausius-Duhem inequality to ensure thermodynamic consistency.

2.3.3 Conservation of angular momentum

The conservation of angular momentum implies that the stress tensor should be symmetric in order to satisfy the conservation of angular momentum

$$\frac{\mathrm{D}}{\mathrm{D}t} \int_{\Omega} \boldsymbol{x} \times \rho \boldsymbol{v} \, \mathrm{d}\Omega = \int_{\Gamma} \boldsymbol{x} \times \rho \boldsymbol{b} \, \mathrm{d}\Omega + \int_{\Gamma} \boldsymbol{x} \times \boldsymbol{t} \, \mathrm{d}\Gamma \,, \tag{2.16}$$

which (through Nanson's relationship and others) leads to the condition that

$$\boldsymbol{\sigma} = \boldsymbol{\sigma}^{\mathrm{T}} \,. \tag{2.17}$$

2.3.4 Conservation of linear momentum

The central problem in computational continuum mechanics is finding the solution to the balance of linear momentum. Based on Newton's second law of motion, the equation of linear momentum relates the sum of the forces acting on the body to the acceleration. The derivation will be provided in integral form, however the differential form can be written in an equivalent manner.

Consider the integral form of linear momentum

$$\boldsymbol{p} = \int_\Omega \rho\, \boldsymbol{v}(\boldsymbol{x}, t)\, \mathrm{d}\Omega\,, \tag{2.18}$$

where the body is also subject to the externally applied volume load $\boldsymbol{b}$ and surface tractions $\boldsymbol{t}$

$$\boldsymbol{f}(t) = \int_\Omega \rho\, \boldsymbol{b}(\boldsymbol{x}, t)\, \mathrm{d}\Omega + \int_\Gamma \boldsymbol{t}(\boldsymbol{x}, t)\, \mathrm{d}\Gamma\,. \tag{2.19}$$

Taking the material time derivative of the linear momentum (2.18) and equating that to the external forces (2.19) yields

$$\frac{\mathrm{D}\boldsymbol{p}}{\mathrm{D}t} = \boldsymbol{f}(t) = \int_\Omega \rho\, \boldsymbol{b}(\boldsymbol{x}, t)\, \mathrm{d}\Omega + \int_\Gamma \boldsymbol{t}(\boldsymbol{x}, t)\, \mathrm{d}\Gamma\,. \tag{2.20}$$

The material time derivative of the linear momentum can be written as

$$\frac{\mathrm{D}\boldsymbol{p}}{\mathrm{D}t} = \int_\Omega \rho\frac{\mathrm{D}\boldsymbol{v}}{\mathrm{D}t} + \boldsymbol{v} \cdot \underbrace{\left(\frac{\mathrm{D}\rho}{\mathrm{D}t} + \rho\nabla\boldsymbol{v} \right)}_{\text{vanishes due to (2.13)}} \mathrm{d}\Omega\,. \tag{2.21}$$

Using the Gauss divergence theorem it is possible to obtain the traction surface integral as an integral over the volume of the divergence of the Cauchy stress as

$$\int_\Omega \nabla \cdot \boldsymbol{\sigma}\, \mathrm{d}\Omega = \int_\Gamma \boldsymbol{t}\, \mathrm{d}\Gamma = \int_\Gamma \boldsymbol{\sigma} \cdot \boldsymbol{n}\, \mathrm{d}\Gamma\,. \tag{2.22}$$

Substituting (2.22) into (2.21) provides

$$\rho\frac{\mathrm{D}\boldsymbol{v}}{\mathrm{D}t} = \nabla \cdot \boldsymbol{\sigma} + \rho\boldsymbol{b}\,, \tag{2.23}$$

which is a hyperbolic partial differential equation for the description of conservation of linear momentum. For problems in steady-state, the time derivative vanishes and the solution of

$$\nabla \cdot \boldsymbol{\sigma} + \rho\boldsymbol{b} = \boldsymbol{0} \tag{2.24}$$

is all that is required. To complete the formulation, the boundary value problem in the strong form for linear momentum is summarised below.

Strong Form of Linear Momentum
Given $f_i : \Omega \to \mathbb{R}$, $g_i : \Gamma_{g_i} \to \mathbb{R}$ and $t_i : \Gamma_{t_i}$, determine $u_i : \Omega \to \mathbb{R}$ such that

$$\nabla \cdot \boldsymbol{\sigma} + \rho\boldsymbol{b} = \boldsymbol{0} \quad \text{in } \Omega \tag{2.25}$$

$$u_i = g_i \quad \text{on } \Gamma_{g_i} \tag{2.26}$$

$$\sigma_{ij} n_j = t_i \quad \text{on } \Gamma_{t_i} \tag{2.27}$$

holds, where i represents the component in three-dimensional space, i.e., $i \in \{1, 2, 3\}$, Γ_{t_i} is the surface subjected to the ith component of the prescribed traction t_i and finally Γ_{g_i} is the surface subject to the ith prescribed Dirichlet condition g_i. For simplicity, we assume

$$\Gamma_t \cap \Gamma_g = \varnothing\,. \tag{2.28}$$

2.4 Differential geometry

Before introducing constitutive theory, a slight detour into differential geometry is required. For reasons that will become obvious later, the role of the deformation gradient to map between configurations plays a central role in developing constitutive models in a finite-strain framework. Firstly, the metric will be briefly introduced, followed by the multiplicative split of the deformation gradient and the concept of the Lie derivative.

2.4.1 Generalised coordinates

For an in-depth understanding of the continuum mechanics framework in which the ageing model is constructed, it is useful to explore the theory in terms of a general basis framework rather than assuming a Cartesian basis. An important part of the general analysis of tensors on manifolds requires the introduction and understanding of the metric tensor and its role as a deformation measure in the current configuration. It is important to note, that if the theory remains in the Cartesian basis, then the reader can replace $\boldsymbol{g}$ in the following with the second order identity tensor and carry on blissfully unaware.

In this exposition, the covariant bases of the metric tensor are denoted with curly brace and a subscript

$$\{\boldsymbol{g}_i\}_{i \in \{1,2,3\}} \tag{2.29}$$

and are not required to be orthogonal or possess a unit length. The dual of this vector space is given by the contravariant basis and are written instead with a superscript

$$\{\boldsymbol{g}^i\}_{i \in \{1,2,3\}} \ . \tag{2.30}$$

The covariant and contravariant bases satisfy the condition

$$\{\boldsymbol{g}^i\} \cdot \{\boldsymbol{g}_j\} = \delta^i_j \tag{2.31}$$

where the sub- and superscripts behave in the same fashion as the well-known Kronecker delta and is called the mixed Kronecker delta, defined as

$$\delta^i_j = \begin{cases} 0 & i \neq j \\ 1 & i = j \end{cases} \ . \tag{2.32}$$

Following [Holzapfel, 2002] the identity for covariant bases

$$\{\boldsymbol{g}_i\} \cdot \{\boldsymbol{g}_j\} = g_{ij} \tag{2.33}$$

and the analogue for contravariant bases

$$\{\boldsymbol{g}^i\} \cdot \{\boldsymbol{g}^j\} = g^{ij} \tag{2.34}$$

hold as expected. These bases can provide additional geometric insight through the length of the associated basis vectors

$$|\{\boldsymbol{g}_i\}| = \sqrt{g_{ii}} \tag{2.35}$$

and the angle between two basis vectors i and j is given by

$$\cos\theta(\{\boldsymbol{g}_i\}, \{\boldsymbol{g}_j\}) = \frac{g_{ij}}{\sqrt{g_{ii}\, g_{jj}}} \ . \tag{2.36}$$

Another important result is the reciprocal property, which relates a basis and its dual as

$$g^{ij}g_{jk} = \delta^i_k \tag{2.37}$$

which can be interpreted as an inverse operation

$$g_{ij} = (g^{ij})^{-1} \ . \tag{2.38}$$

If we select an orthonormal basis then the tedium associated with super- and subscripts collapses to

$$\{\boldsymbol{g}_i\} = \{\boldsymbol{g}^i\} \tag{2.39}$$

which is satisfied by choosing a Cartesian basis. Employing a multiplicative split of the deformation gradient as seen in the next section introduces an intermediate configuration where the metric ($\boldsymbol{g} = \boldsymbol{1}$) is no longer valid.

2.4.2 Multiplicative split of the deformation gradient

It is very common to decompose the deformation gradient into elastic and plastic parts in the following manner

$$\mathbf{F} = \mathbf{F}^e \cdot \mathbf{F}^p \ , \tag{2.40}$$

especially in finite strain elastoplasticity [Lee, 1969, de Souza Neto et al., 2011]. The split of the deformation gradient is used to model a fictitious configuration where the body is considered to be stress-free, see Figure 2.2.
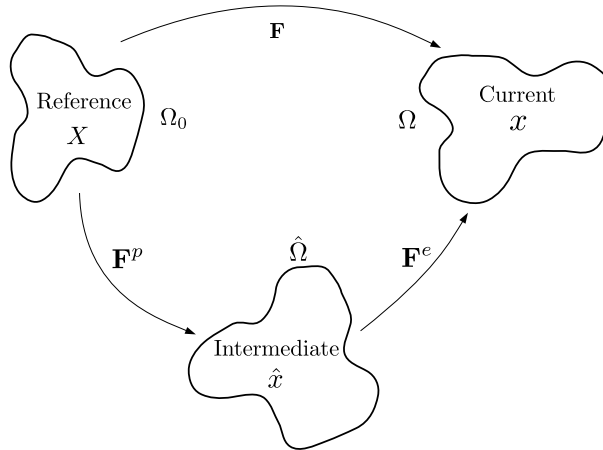
Figure 2.2: The reference, intermediate and current configurations and the corresponding decomposed deformation gradient transformations

Mapping between these configurations is accomplished with the deformation gradient. Expressions for mapping between configurations are summarised in Table 2.1, depending on whether the operation is applied to a covariant or contravariant tensor.

The insight provided by these mappings has a wide-reaching impact on the understanding of strain and stress measures. The second Piola-Kirchhoff stress is simply push forward to the current configuration to obtain the Kirchhoff stress. Similarly the metric $\boldsymbol{g}$ in the current configuration is the push forward of the right

Table 2.1: Pull back and push forward second order tensor operations [Belytschko et al., 2013]

Operation	Contravariant-Contravariant	Covariant-Covariant
Push forward $\phi_* \left(\cdot \right)$	$\phi_* \left(\mathbf{S} \right) = \mathbf{F} \cdot \mathbf{S} \cdot \mathbf{F}^{\mathrm{T}} = \boldsymbol{\tau}$	$\phi_* \left(\mathbf{C} \right) = \mathbf{F}^{-\mathrm{T}} \cdot \mathbf{C} \cdot \mathbf{F}^{-1} = \boldsymbol{g}$
Pull back $\phi^* \left(\cdot \right)$	$\phi^* \left(\boldsymbol{\tau} \right) = \mathbf{F}^{-1} \cdot \boldsymbol{\tau} \cdot \mathbf{F}^{-\mathrm{T}} = \mathbf{S}$	$\phi^* \left(\boldsymbol{g} \right) = \mathbf{F}^{\mathrm{T}} \cdot \boldsymbol{g} \cdot \mathbf{F} = \mathbf{C}$

Cauchy-Green deformation tensor in the reference configuration. Pull back and push forward operations can be viewed as nothing more than transformations between manifolds. Further information in an elasticity setting can be found in [Marsden and Hughes, 1994]. Mapping between the intermediate and the reference (or current configuration) is provided by the elastic and plastic deformation gradients in the same manner as Table 2.1.

2.4.3 The Lie derivative

The Lie derivative, alongside the pull-back and push-forward operators, provides a mathematically consistent definition for computing the time derivatives of tensors. Consider a second order tensor defined in the current configuration. Taking the Lie derivative entails pulling the result back to the reference configuration, performing the material time derivative and pushing the result forward to the current configuration. For example, the Lie derivative of the Kirchhoff stress is given by

$$\mathcal{L}_{\boldsymbol{v}} \left(\boldsymbol{\tau} \right) = \phi_* \left(\frac{\mathrm{D}}{\mathrm{D}t} \phi^* \left(\boldsymbol{\tau} \right) \right) \,, \tag{2.41}$$

and evaluating the Lie derivative results in

$$\mathcal{L}_{\boldsymbol{v}} \left(\boldsymbol{\tau} \right) = \dot{\boldsymbol{\tau}} - \boldsymbol{l} \cdot \boldsymbol{\tau} - \boldsymbol{\tau} \cdot \boldsymbol{l}^{\mathrm{T}} \,. \tag{2.42}$$

The definition in (2.42) is equivalent to the convected rate of the Truesdell stress rate [Belytschko et al., 2013]. This fact will be elaborated in Section 2.5.1. The definition of the Lie derivative for a covariant tensor (e.g. the metric in the current configuration) is given by

$$\mathcal{L}_{\boldsymbol{v}} \left(\boldsymbol{g} \right) = \phi_* \left(\frac{\mathrm{D}}{\mathrm{D}t} \phi^* \left(\boldsymbol{g} \right) \right) \tag{2.43}$$

$$= \mathbf{F}^{-\mathrm{T}} \cdot \frac{\mathrm{D}}{\mathrm{D}t} \left(\mathbf{F}^{\mathrm{T}} \cdot \boldsymbol{g} \cdot \mathbf{F} \right) \cdot \mathbf{F}^{-1} \tag{2.44}$$

$$= \mathbf{F}^{-\mathrm{T}} \cdot \dot{\mathbf{C}} \cdot \mathbf{F}^{-1} = 2\mathbf{d} \,, \tag{2.45}$$

which relates the Lie derivative of the metric to the rate of deformation tensor. The elastic Lie derivative can be introduced as a means to derive the plastic contribution to the material tangent operator [Belytschko et al., 2013]. Let the elastic Lie derivative of the Kirchhoff stress be defined as

$$\mathcal{L}_{\boldsymbol{v}}^{e} \left(\boldsymbol{\tau} \right) = \phi_*^{e} \left(\frac{\mathrm{D}\phi_e^* \left(\boldsymbol{\tau} \right)}{\mathrm{D}t} \right) = \mathbf{F}^e \cdot \frac{\mathrm{D}}{\mathrm{D}t} \left(\left(\mathbf{F}^e \right)^{-1} \cdot \boldsymbol{\tau} \cdot \left(\mathbf{F}^e \right)^{-\mathrm{T}} \right) \cdot \left(\mathbf{F}^e \right)^{\mathrm{T}} \tag{2.46}$$

which can also be expressed as

$$\mathcal{L}_{\boldsymbol{v}}^{e} \left(\boldsymbol{\tau} \right) = \mathbf{F}^e \cdot \dot{\hat{\mathbf{S}}} \cdot \left(\mathbf{F}^e \right)^{\mathrm{T}} \tag{2.47}$$

12

where $\dot{\bar{\mathbf{S}}}$ is the time derivative of the second Piola-Kirchhoff stress defined on the intermediate configuration. Taking the derivative with respect to time yields

$$\mathcal{L}_{v}^{e}\left(\boldsymbol{\tau}\right) = \dot{\boldsymbol{\tau}} - \boldsymbol{l}^{e} \cdot \boldsymbol{\tau} - \boldsymbol{\tau} \cdot (\boldsymbol{l}^{e})^{\mathrm{T}} = \boldsymbol{\tau}^{\nabla ce} \tag{2.48}$$

with the elastic Lie derivative leading to the interpretation of equivalence of the elastic convected rate of stress. The definition of the Truesdell rate of the Cauchy stress as the Lie derivative of the Kirchhoff stress (multiplied by the Jacobian determinant) is given as

$$J\boldsymbol{\sigma}^{\nabla T} = \mathcal{L}_{v}\left(\boldsymbol{\tau}\right) = \dot{\boldsymbol{\tau}} - \boldsymbol{l} \cdot \boldsymbol{\tau} - \boldsymbol{\tau} \cdot \boldsymbol{l}^{\mathrm{T}} \ . \tag{2.49}$$

In Appendix C, the Lie derivative is applied judiciously during the derivation of the constitutive model in the spatial setting.

2.5 Constitutive theory

Constitutive theory is required to provide the crucial link between the strain measure and the stress measure in the balance of linear momentum. As one would imagine, constitutive modelling is one of the most contentious subjects in solid mechanics, partly due wide variety of complex behaviour that it needs to mathematically describe. These models are proposed, derived and tested against available experimental data whilst simultaneously ensuring that particular theoretical criteria are met.

A valid constitutive model should possess or be:

1. Physical admissibility (thermodynamic consistency)

2. Deterministic

3. Equipresence

4. Local (smoothness)

5. Material objectivity

6. Material symmetry

according to [de Souza Neto et al., 2011, Chung, 2007]. These properties are to be confirmed for each proposed material model. One of the most critical is the thermodynamic consistency, which implies that the model satisfies the requirements of the Clausius-Duhem inequality

$$\boldsymbol{\sigma} : \mathbf{d} - \left(\dot{\Psi} + s\rho\dot{\theta} - \frac{1}{\theta}\boldsymbol{q} \cdot \nabla_{\boldsymbol{x}}\theta \right) \geq 0 \ , \tag{2.50}$$

where $\boldsymbol{q}$ is the heat flux vector, θ is the absolute temperature and Ψ is the free energy per unit volume [de Souza Neto et al., 2011]. The objectivity axiom is satisfied if the material response does not change with a change of observer. In other words, an arbitrary translation $\boldsymbol{y}(t)$ and rotation $\boldsymbol{Q}(t)$ of the observer must not influence the deformation map for all time, viz.,

$$\phi_{t}^{'}(\boldsymbol{p}) = \boldsymbol{y}(t) + \boldsymbol{Q}(t)\left[\phi_{t}(\boldsymbol{p}) - \boldsymbol{x}_{0}\right] \ . \tag{2.51}$$

For materials that undergo finite elastic deformations, the constitutive model is typically hyperelastic in nature, meaning it is derived from a potential function. The theoretical validity of constitutive models in the

finite strain framework depends on whether it is objective and possesses frame invariance. For hyperelastic models it is possible to prove this property by applying a rotation $\boldsymbol{Q} \in \mathrm{SO}(3)$, where

$$\mathrm{SO}(3) := \{\boldsymbol{R} \in \mathbb{R}^{3 \times 3} : \boldsymbol{R}^{\mathrm{T}} \cdot \boldsymbol{R} = \boldsymbol{1}, \det \boldsymbol{R} = 1\}\,, \tag{2.52}$$

and showing that the free energy

$$\Psi(\mathbf{F}) = \Psi(\boldsymbol{Q} \cdot \mathbf{F}) \tag{2.53}$$

remains invariant to any rotation in $\mathrm{SO}(3)$.

The introduction of a free energy function means that an analytical expression for the stress can be derived. For example, the Kirchhoff stress can be related through the Doyle-Erickson formula [Doyle and Erickson, 1959] by

$$\boldsymbol{\tau} = 2\frac{\partial \Psi(\boldsymbol{g}, \mathbf{F})}{\partial \boldsymbol{g}}\,, \tag{2.54}$$

where Ψ is the free energy as a function of the metric and the deformation gradient. Alternative methods for computing the Kirchhoff stress exist, including differentiating the free energy function with respect to a Lagrangian strain tensor and then a push-forward to obtain the Kirchhoff stress. Differentiating twice with respect to the metric leads to the material tangent operator

$$\mathbb{C} = 4\frac{\partial^2 \Psi(\boldsymbol{g}, \mathbf{F})}{\partial \boldsymbol{g} \partial \boldsymbol{g}} = 2\frac{\partial \boldsymbol{\tau}}{\partial \boldsymbol{g}}\,, \tag{2.55}$$

as required for the implementation of a model in an implicit finite element framework.

2.5.1 Objective stress rates

Objective stress rates are required to ensure that rigid body motion does not cause a fictitious change in stress when a change of observer is made. Consider the rotation of a solid body under some predefined stress and the following constitutive law from [Belytschko et al., 2013]

$$\frac{\mathrm{D}\boldsymbol{\sigma}}{\mathrm{D}t} = \mathbb{C} : \mathbf{d}\,. \tag{2.56}$$

In this case, the Cauchy stress values will change according to the rotation but the rate of deformation tensor is $\boldsymbol{0}$ during rigid body motion. To correct this issue, an objective rate of the Cauchy stress is introduced. There are several choices available

1. Jaumann rate

2. Oldroyd rate

3. Truesdell rate

4. Green-Naghdi rate

however it is important to note that the material properties obtained with one particular stress-rate cannot be used in another constitutive model based on a different stress rate without the appropriate transformations, if applicable [Ji et al., 2013].

The choice of the objective stress-rate used in this work is the Oldroyd rate due to its use in the governing mechanical constitutive model. Since the Oldroyd rate is the definition of the Lie time derivative of the

Cauchy stress (denoted with $\sharp$), material frame indifference is automatically obtained as the Lie derivative of spatial tensor fields are themselves also objective spatial tensor fields, viz.,

$$\mathcal{L}_v(\boldsymbol{\sigma}^\sharp) = \mathbf{F} \cdot \left(\frac{\mathrm{D}}{\mathrm{D}t}(\mathbf{F}^{-1} \cdot \boldsymbol{\sigma} \cdot \mathbf{F}^{-\mathrm{T}}) \right) \cdot \mathbf{F}^{\mathrm{T}} \tag{2.57}$$

$$= \dot{\boldsymbol{\sigma}} - \boldsymbol{l} \cdot \boldsymbol{\sigma} - \boldsymbol{\sigma} \cdot \boldsymbol{l}^{\mathrm{T}} , \tag{2.58}$$

where $\boldsymbol{l}$ is the velocity gradient. This makes the Oldroyd rate a natural objective rate to use due to its relationship with the Lie derivative.

2.6 Non-linear finite element formulation

Complexities arising from the geometry or properties of a partial differential equation (PDE) often result in the absence of an analytical closed-form solution. Therefore, a numerical method is the best option to obtain an approximate solution without resorting to experimental techniques (depending on availability feasibility of techniques). The finite element method is arguably the most successful and widespread numerical method for the solution of PDEs, especially those arising from the field of solid mechanics. The entire branch of computational solid mechanics is dedicated to formulating and solving the linear momentum equation for different mechanical problems, with extensions to include fluid-solid interaction, heat diffusion and contact problems. With the increase in computational power and the development of robust algorithms, non-linearities arising from the choice of finite strain measures and complex material models can be routinely simulated in engineering practice and aid tremendously with advanced research and design tasks.

In this section, the weak form of the momentum equation is introduced followed closely by the finite element discretisation. An introductory text on the basics of linear finite elements can be found in [Hughes, 2012]. Material and geometric non-linearities encountered in advanced models require an incremental approach to their solution, namely using the Newton-Raphson procedure for the linearisation and the solution of the arising linear system of equations. This exposition follows the classical texts [Hughes, 2012, Wriggers, 2008, Belytschko et al., 2013, de Souza Neto et al., 2011], however only the key ideas are reproduced here for completeness.

2.6.1 Variational form

The fundamental principal behind the finite element method is the conversion of the strong form of a PDE into a variational form. The resulting integral form often has a weaker requirement on the differentiability of the solution, such that an approximation solution can be searched for in a function space consisting of simple polynomial functions [Strang and Fix, 2008].

Consider that we wish to solve a PDE for an unknown u. For reasons outside the scope of this thesis, the chosen function spaces must satisfy

$$\int_{\mathcal{B}} (u_{,x})^2 \, \mathrm{d}x < \infty \tag{2.59}$$

i.e., the function spaces must be square-integrable. A convenient choice is the Sobolev space of degree one and we restrict our search to $u \in H^1$, where u represents the velocity in the updated Lagrange framework. Let $\mathcal{S}$ and $\mathcal{V}$ be the function spaces containing the trial and weighting functions respectively. We require the trial solutions to fulfill the non-homogeneous Dirichlet boundary condition

$$\mathcal{S} = \{u \mid u \in H^1, u(\Gamma_{g_i}) = g_i\} . \tag{2.60}$$

Weighting functions are built in much the same fashion but are required to satisfy the homogeneous part of the Dirichlet condition

$$\mathcal{V} = \{w \mid w \in H^1, w(\Gamma_{g_i}) = 0\} \ . \tag{2.61}$$

Proceeding in the usual manner, the residual of the strong form of the balance of linear momentum in Section 2.3.4 is forced to vanish over the domain

$$\int_\Omega w_i \left(\frac{\partial \sigma_{ji}}{\partial x_j} + \rho b_i \right) \mathrm{d}\Omega = 0 \ , \tag{2.62}$$

where $i \in \{1, 2, 3\}$ and $j \in \{1, 2, 3\}$ for three dimensional Cartesian space. Note that the derivatives and integrals are defined with respect to the current configuration. Through the application of integration by parts and Gauss's theorem, the following form can be obtained in index form

$$\int_\Omega \frac{\partial w_i}{\partial x_j} \sigma_{ji} \, \mathrm{d}\Omega - \int_\Omega w_i \rho \, b_i \, \mathrm{d}\Omega - \sum_{i=1}^{3} \int_{\Gamma_{t_i}} w_i t_i \, \mathrm{d}\Gamma = 0 \ . \tag{2.63}$$

Recall the principle of virtual power

$$0 = \delta\mathcal{P} = \delta\mathcal{P}^{\mathrm{int}} - \delta\mathcal{P}^{\mathrm{ext}} + \delta\mathcal{P}^{\mathrm{kin}} \ . \tag{2.64}$$

The terms in the weak form are equivalent to those in the virtual power statement, namely the virtual internal power

$$\mathcal{P}^{\mathrm{int}} = \int_\Omega \frac{\partial w_i}{\partial x_j} \sigma_{ji} \, \mathrm{d}\Omega \ , \tag{2.65}$$

and the virtual external power

$$\mathcal{P}^{\mathrm{ext}} = - \int_\Omega w_i \rho \, b_i \, \mathrm{d}\Omega - \sum_{i=1}^{3} \int_{\Gamma_{t_i}} w_i t_i \, \mathrm{d}\Gamma \tag{2.66}$$

omitting the contribution from the inertial power due to mass. Note that in the total Lagrangian formulation, u represents the displacement and the terms associated with power are instead associated with the energy, although this is not the only possible formulation.

2.6.2   Galerkin approximation method

The Galerkin method begins with constructing a finite-dimensional approximation of the sets in (2.60) and (2.61). These are denoted with a superscript h and are defined as $\mathcal{S}^h \subset \mathcal{S}$ and $\mathcal{V}^h \subset \mathcal{V}$. The members of the set are $u^h \in \mathcal{S}^h$ and $w^h \in \mathcal{V}^h$ for the trial solution and weighting functions respectively. Provided $\mathcal{V}^h$ is known, then the member $v^h \in \mathcal{V}^h$ can be used to write

$$u^h = v^h + g^h \tag{2.67}$$

which satisfies the Dirichlet boundary conditions based on the original definitions of $\mathcal{S}$ and $\mathcal{V}$ [Hughes, 2012]. We introduce the shape function discretisation for the solution and the weighting functions as

$$u_i^h = \sum_{a=1}^{n} N_a u_{i,a} \ \ \text{for} \ \ i \in \{1, 2, 3\} \tag{2.68}$$

$$w_i^h = \sum_{a=1}^{n} N_a w_{i,a} \ \ \text{for} \ \ i \in \{1, 2, 3\} \tag{2.69}$$

respectively, where N_a are the shape functions at node a and n is the number of nodes per element. Applying the discretisation to the weak form leads to

$$\int_\Omega \frac{\partial N_a}{\partial x_j} \sigma_{ji} \; \mathrm{d}\Omega - \int_\Omega N_a \rho \, b_i \; \mathrm{d}\Omega - \sum_{j=1}^{3} \int_{\Gamma_{t_i}} N_a t_i \; \mathrm{d}\Gamma = 0 \; . \tag{2.70}$$

In complex material models, the relationship between the displacement and the stress itself depends non-linearly on the displacement and can also depend on the state of internal variables. Therefore a linear relationship cannot be drawn and the linearisation and incremental solution of these equations is required.

The residual of a quasi-static problem can be formulated as the difference between internal and external force vectors

$$\boldsymbol{r} = \boldsymbol{f}^{\mathrm{int}} - \boldsymbol{f}^{\mathrm{ext}} \; . \tag{2.71}$$

In a state of equilibrium, the internal and external forces should balance and the residual should approach zero. Without delving into details, the discretised element form of the virtual internal power is given by the numerical integration over the mesh as

$$(\boldsymbol{f}_a^{\mathrm{int}})^{\mathrm{T}} = \int_\Omega \boldsymbol{B}_a^{\mathrm{T}} \boldsymbol{\sigma} \; \mathrm{d}\Omega \tag{2.72}$$

where $\boldsymbol{B}$ is the gradient of the shape functions discretising the velocity, expressed in index notation as

$$B_{ja} = \frac{\partial N_a}{\partial x_j} \; . \tag{2.73}$$

The applied body forces are denoted by the vector field $\boldsymbol{b}$. Surfaces are subjected to a traction vector $\boldsymbol{t}$. In this work, only tractions defined in the reference configuration will be considered. Tractions that are defined in the current configuration require linearisation and contribute terms to the so-called external load stiffness matrix. The external forces are computed as

$$\boldsymbol{f}_a^{\mathrm{ext}} = \int_\Omega N_a \rho \, \boldsymbol{b} \; \mathrm{d}\Omega + \int_\Gamma N_a \boldsymbol{t} \; \mathrm{d}\Gamma \; . \tag{2.74}$$

An integration procedure for the element internal and external nodal forces can now be performed with numerical quadrature and assembled into the global internal and external forces vector. For implicit methods, the non-linear equations can be linearised with the aid of the Newton-Raphson method

$$\boldsymbol{0} = \boldsymbol{r} + \frac{\partial \boldsymbol{r}}{\partial \boldsymbol{u}} \Delta \boldsymbol{u} \tag{2.75}$$

to obtain the material and geometric stiffness matrices that require evaluation at each iteration. The material stiffness matrix from the linearisation is defined as

$$\boldsymbol{K}^{\mathrm{mat}} = \int_\Omega \boldsymbol{B}^{\mathrm{T}} \boldsymbol{D} \, \boldsymbol{B} \; \mathrm{d}\Omega \tag{2.76}$$

where the material tangent operator $\boldsymbol{D}$ is determined through the constitutive model and $\boldsymbol{B}$ takes on the same structure as the symmetric gradient operator in infinitesimal strain theory [Hughes, 2012, Belytschko et al., 2013]. The geometric stiffness matrix is given by

$$\boldsymbol{K}^{\mathrm{geo}} = \int_{\Omega_e} \boldsymbol{L}^{\mathrm{T}} \boldsymbol{1}_{3\times3} \boldsymbol{\sigma} \, \boldsymbol{L} \; \mathrm{d}\Omega_e \; , \tag{2.77}$$

and captures the effect that changes in geometry have on the stiffness of the structure [Belytschko et al., 2013]. Note that the fundamental meaning of $\boldsymbol{L}$ is the same as in the material stiffness matrix, but the structure is changed to reflect the structure of $\boldsymbol{\sigma}$. This matrix is sometimes referred to as the *initial stress matrix*. For the sake of clarity, the matrix representation of $\mathbf{1}_{3\times3}\boldsymbol{\sigma}$ in three-dimensions is represented by

$$\mathbf{1}_{3\times3}\boldsymbol{\sigma} = \begin{bmatrix} \boldsymbol{\sigma} & \mathbf{0} & \mathbf{0} \\ \mathbf{0} & \boldsymbol{\sigma} & \mathbf{0} \\ \mathbf{0} & \mathbf{0} & \boldsymbol{\sigma} \end{bmatrix} . \tag{2.78}$$

Both the material and geometric stiffness matrices are computed element-by-element and the integrals are evaluated with the aid of numerical quadrature. Element contributions are assembled, using the direct stiffness method, into a sparse matrix to form the *tangent stiffness* matrix

$$\frac{\partial \boldsymbol{r}}{\partial \boldsymbol{u}} = \boldsymbol{K} = \boldsymbol{K}^{\mathrm{mat}} + \boldsymbol{K}^{\mathrm{geo}} , \tag{2.79}$$

resulting in a large and sparse system of equations in the form

$$\boldsymbol{K}\Delta\boldsymbol{u} = -\boldsymbol{r} \tag{2.80}$$

where the solution gives the increment in the displacement field. The implementation is covered briefly in Section 2.6.3.

2.6.3   Newton-Raphson algorithm

In comparison to the linear case, the non-linear algorithm requires additional steps in the assembly of the material and geometric stiffness matrices, internal and external forces and the internal variable update. The basic algorithm is given in Algorithm 1.

Note that several passes through the linear solver are required and termination depends on a user-specified tolerance on the relative displacement and residual two-norm. The associated computational cost increases considerably, depending heavily on the severity of the non-linearities encountered during the solution routine.

A well-known property of the Newton-Raphson procedure is that it exhibits quadratic convergence in the neighbourhood of the solution. This property is essential in ensuring rapid convergence and acts as a guide for correct implementation of the material tangent operator. It should be noted that the material tangent is only a mathematical relationship and it can be numerically approximated. In contrast to implicit algorithms, explicit finite element methods avoid the computation of the material tangent which saves considerably on storage cost. Modifications to the base Newton-Raphson algorithm can be employed to improve computational performance for some classes of problems, see [Belytschko et al., 2013] for additional information.

Result: Update of $\boldsymbol{u}$, $\boldsymbol{\sigma}$

$\boldsymbol{u} = \boldsymbol{u}_0$;

$\boldsymbol{\sigma} = \boldsymbol{\sigma}_0$;

for *each load step* **do**

    Compute $\boldsymbol{f}^{\text{ext}}$;

    Set $k = 1$;

    while $||\Delta\boldsymbol{u}|| > tol$ *or* $||\boldsymbol{r}|| > tol$ **do**

        Compute and assemble material stiffness $\boldsymbol{K} \leftarrow \boldsymbol{K}^{\text{mat}}$;

        Compute and assemble geometric stiffness $\boldsymbol{K} \leftarrow \boldsymbol{K} + \boldsymbol{K}^{\text{geo}}$;

        Compute and assemble internal force $\boldsymbol{f}^{\text{int}}$;

        if $k = 1$ **then**

            Update $\boldsymbol{f}^{\text{ext}}$ with Dirichlet condition;

            Enforce Dirichlet boundaries in $\boldsymbol{K}$;

        end

        Compute residual $\boldsymbol{r} = \boldsymbol{f}^{\text{int}} - \boldsymbol{f}^{\text{ext}}$;

        Solve $\Delta\boldsymbol{u} = -\boldsymbol{K}^{-1}\boldsymbol{r}$;

        Update displacement $\boldsymbol{u}_{k+1} = \boldsymbol{u}_k + \Delta\boldsymbol{u}$

        Update coordinates $\boldsymbol{x}_{k+1} = \boldsymbol{X} + \boldsymbol{u}_{k+1}$;

        Update internal variables;

        $k = k + 1$;

    end

end

Algorithm 1: Basic Newton Raphson algorithm (Implicit)

Chapter 3

Constitutive models of elastomers

Constitutive models of elastomers can be categorised into two distinct types based on their origins; phenomenological and micro-mechanical models. Phenomenological models are derived by including invariants associated with the deformation tensor and introduce material constants in order to replicate the response of a sample during uniaxial and biaxial experiments. These models often have very little or no physical motivation but can be recovered from micro-mechanical models as special cases [Arruda and Boyce, 1993]. In addition, the material parameters often have no physical meaning and must be fit for a given set of experimental data with the risk of obtaining unstable material properties.

Conversely, micro-mechanically based models are derived by considering the physics of a single polymer chain and the associated statistical mechanics. Early models, such as the Neo-Hooke model, were derived from this basis. These models offer insight into the molecular structure of polymers and provide a powerful basis for designing virtual materials. Their material parameters are physically based and can involve less parameters in order to replicate the equivalent behaviour of their phenomenological counterparts.

There are multiple constitutive models for elastomer behaviour with varying degrees of accuracy for given loading conditions but they are subject to more complex parameter fitting procedures. A review of all constitutive models is beyond the scope of this dissertation, however the interested reader is directed to [Boyce and Arruda, 2000] and the excellent comparison of hyperelastic models by [Marckmann and Verron, 2006]. This chapter will briefly introduce the most common phenomenological models and then review the major micro-mechanically motivated elastomer models in Section 3.3.

To accommodate the quasi-incompressibility condition exhibited by elastomers, a decomposition of the free energy function into isochoric and volumetric contributions is commonly performed

$$\Psi = \bar{\Psi} + U(J) , \tag{3.1}$$

where $U(J)$ is the volumetric free energy and the isochoric contribution is given by $\bar{\Psi}$. The stresses and the material tangent follow on from the free energy function in the same decomposed manner. Available volumetric strain energy functions are provided in Section 3.1. Determining the form of the isochoric free energy function is heavily dependent on the material and the physics under investigation. The development of a suitable constitutive model for chemical ageing of elastomers is the topic of the remainder of this dissertation.

3.1   Volumetric strain energy

For the selection of the volumetric strain energy $U(J)$ there are multiple possibilities. The commonly available functions are summarised in Table 3.1 and depicted in Figure 3.1 as reviewed by [Doll and Schweizer-
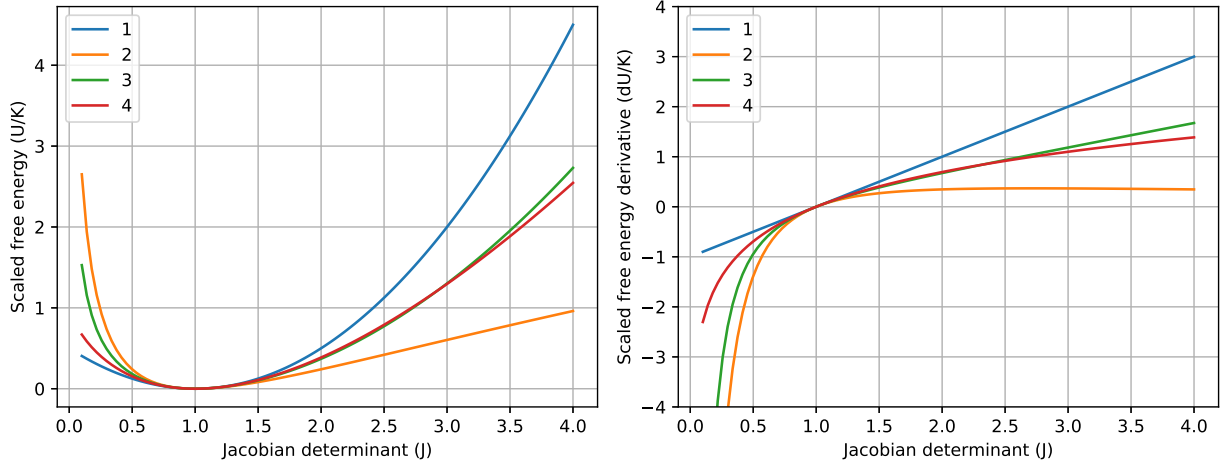
Figure 3.1: Comparison of volumetric strain energy function and the derivative. Note all functions behave the same in the neighbourhood of $J = 1$ which is consistent with the incompressibility constraint

Table 3.1: Functions for volumetric strain function

Author	Volumetric strain energy	Figure
1	$K(J-1)^2/2$	3.1 (1)
2	$K(\ln J)^2/2$	3.1 (2)
3	$K[(J-1)^2 + (\ln J)^2]/4$	3.1 (3)
4	$K\theta^{-2}(\theta \ln J + J^{-\theta} - 1)$	-
5	$K(J \ln J - J + 1)$	3.1 (4)

Inspection of Figure 3.1 indicates that the choice of the free energy function is not of critical importance in the neighbourhood of $J = 1$. However, the consequences for the choice of a particular free energy function are realised when implementing these functions into a finite element framework, where modified weak forms designed to deal with incompressibility constraints place requirements on the form of the volumetric free energy model [de Souza Neto et al., 2011, Belytschko et al., 2013, Horgan and Murphy, 2009].

3.2 Phenomenological models

Phenomenological models are not usually derived from a physical background and do not have parameters that correspond with a physical quantity. Such models are commonly implemented in commercial finite element codes and enjoy widespread use in the modelling community, due to their ease of parameter fitting. However, phenomenological models limit the understanding and development of more advanced constitutive models that include micro-mechanical effects. This section will briefly detail some of the more popular and widely used phenomenological models, as these are used in oxidative ageing constitutive models.

3.2.1 Neo-Hooke

The Neo-Hooke model is one of the earliest hyperelastic material models for elastomer materials. The free energy function is actually derived from micro-mechanical basis and averaged, or homogenised, to the macroscale. Despite this, it remains a relatively simple and popular hyperelastic model for geometric non-linearity modelling and is defined as

$$\Psi(\mathbf{C}) = \underbrace{\frac{1}{2}\mu_0(\mathrm{I}_{\bar{\mathbf{C}}} - 3)}_{\text{isochoric}} + \underbrace{\frac{1}{2}\lambda_0(\ln J)^2 - \mu_0 \ln J}_{\text{volumetric}}, \tag{3.2}$$

where $\mathrm{I}_{\bar{\mathbf{C}}} = \mathrm{tr}\left(\bar{\mathbf{C}}\right)$ is the trace of the unimodular right Cauchy-Green deformation tensor, μ_0 is the shear modulus, λ_0 is the Lamé parameter and J is the determinant of the deformation gradient. The volumetric free energy term is added after the isochoric term and can be changed to achieve different model properties, see Section 3.1 for additional details. In order to compute the stress and the material tangent for the Neo-Hooke model, the free energy can be differentiated once and twice with respect to the strain measure for the stress and the material tangent respectively. This is an exercise in tensor differentiation and the results can be found in [Belytschko et al., 2013].

3.2.2 Mooney-Rivlin

By specialising the general form of the isotropic hyperelastic material model, [Mooney, 1940] and [Rivlin, 1948] rewrote the isochoric free energy function in terms of first and second invariants of the unimodular right Cauchy-Green deformation tensor as

$$\bar{\Psi}_{\mathrm{MR}}(\mathrm{I}_{\bar{\mathbf{C}}}, \mathrm{II}_{\bar{\mathbf{C}}}) = c_{10}(\mathrm{I}_{\bar{\mathbf{C}}} - 3) + c_{20}(\mathrm{II}_{\bar{\mathbf{C}}} - 3), \tag{3.3}$$

where c_{10} and c_{20} are material parameters. This particular form includes the $\mathrm{II}_{\bar{\mathbf{C}}}$ effect associated with the surface deformation on a unit cube. An advantage of this model is that it approximates the mechanical response curve of a test specimen in uniaxial tension with better accuracy compared to the Neo-Hooke model. However, the increase in fidelity comes at the cost of fitting an additional material parameter, usually involving not only uni-axial test results but also a more complicated and expensive bi-axial test. A complete view of the free energy function requires an additional volumetric free energy term, as did the Neo-Hooke model. This can be added simply by choosing an appropriate volumetric strain energy function.

3.3 Micro-mechanical models

Elastomers have been subjected to micro-mechanical investigations in order to explain their peculiar mechanical behaviour since the development of the Neo-Hooke material model. Chief amongst these peculiar properties is elastomers' ability to *release* heat during tension and *absorb* heat as they return to their original position. This is attributed to their molecular composition and is caused by changes to the entropy of the underlying polymer network [Edwards, 1967a, Edwards, 1967b, Penrose, 1969]. Micro-mechanical approaches exploit this observation and apply thermodynamic laws to a single elastomer chain, always seeking to characterise the entropy and relating that to the work performed in order to derive stresses and material tangent operators suitable for implementation in a finite element code.

For a single polymer chain, the kinematics are described by the chain stretch represented here by λ [Kuhn and Grün, 1942]. This quantity represents the deformation of a single polymer chain and is related

to the chain end-to-end distance r and initial chain end-to-end distance r_0.

$$\lambda = \frac{r}{r_0} \ . \tag{3.4}$$

Using the root-mean square distance of the polymer chain, r_0 can be expressed as $r_0 = \sqrt{N}l$, where N is the average number of segments per chain and l is the length of a segment. The contour length can then be expressed as $L = Nl$. The stretch is defined to be valid in the interval $\lambda \in [0, \sqrt{N})$, where $\sqrt{N}$ is not theoretically obtainable due to finite extensibility constraints. In addition to the stretch, a *relative stretch* can be defined as

$$\lambda_r = \frac{r}{L} = \frac{r_0\lambda}{L} = \frac{r_0\lambda}{Nl} = \frac{\lambda}{\sqrt{N}} \ , \tag{3.5}$$

where L is the contour length of the polymer chain and λ_r is defined on the interval $[0, 1)$.

The Gaussian probability function

$$p_f(\lambda) = p_0 \exp\left(-\frac{3}{2}\lambda^2\right) , \tag{3.6}$$

describes the likelihood of finding the chain with a given stretch λ. The relationship between the chain free energy ψ_f and the stretch λ is expressed as

$$\psi_f(\lambda) = -k\theta \ln p_f(\lambda) \ , \tag{3.7}$$

where the Boltzmann equation relates the number of micro-states (the available configurations) of the polymer chain to the entropy. Furthermore it can be written in the case of Gaussian statistics that

$$\psi_f = \frac{3}{2}k\theta\lambda^2 + \psi_0 \ . \tag{3.8}$$

The relationship between chain force F_f and the chain free energy is provided by thermodynamics and is given by

$$F_f = \frac{\mathrm{d}\psi_f(\lambda)}{\mathrm{d}\lambda} \ , \tag{3.9}$$

leading to the simple expression of chain force as

$$F_f = 3kT\lambda \ , \tag{3.10}$$

where T is the absolute temperature in Kelvin, k is the Boltzmann constant and λ is the stretch [Treloar, 1975]. Instead of using a Gaussian probability distribution, a non-Gaussian approach can be made based on the Langevin chain statistics. This form provides a more faithful representation of the finite-extensibility condition evidenced by experimental results [Treloar, 1944].

Sophisticated approaches have been employed to model the mechanical response of the polymer network, including the three, four and eight chain models, whereby the arrangement of polymer chains in space is assumed and the resulting continuum model is extracted. Additional effects specific to polymers can also be modelled, for example strain crystallisation [Mistry and Govindjee, 2014], viscoelasticity [Göktepe and Miehe, 2004, Miehe and Göktepe, 2005] and the Mullins effect [Govindjee and Simo, 1992a, Govindjee and Simo, 1992b, Göktepe and Miehe, 2005, Stegen, 2014]. A sketch of the different approaches is given in Figure 3.2.

(a) Three chain model

(b) Four chain model

(c) Eight chain model

(d) Microsphere model
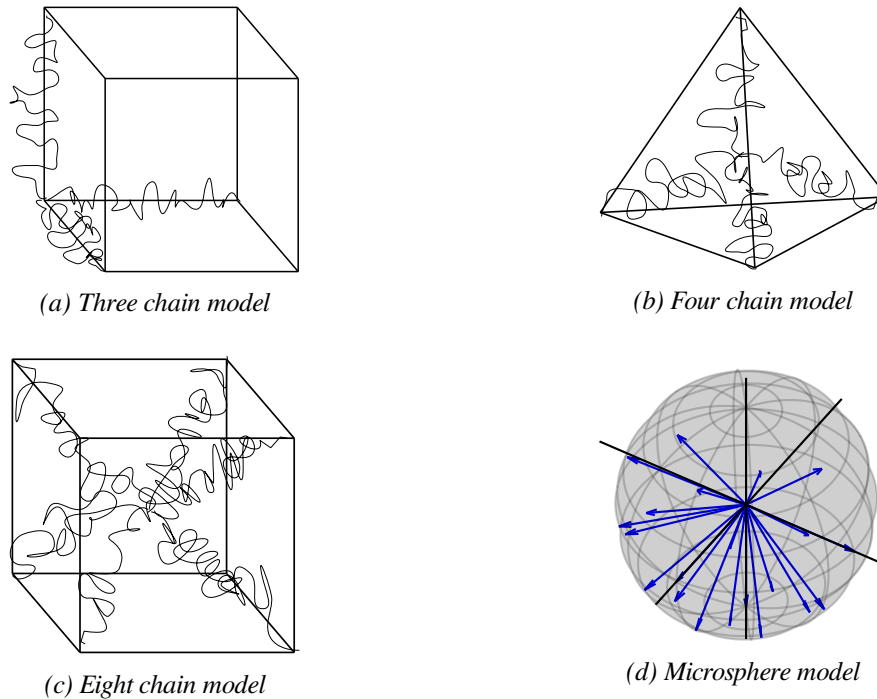
Figure 3.2: Chain homogenisation techniques

In perhaps the most intuitive arrangement of chains, the three chain model aligns non-Gaussian chains parallel to the coordinate system and uses two strain invariants in its description of deformation [Wang and Guth, 1952]. An alternative topology, proposed by [Flory and Jr., 1943], is to arrange four chains with equal contour length from the centre of a tetrahedron to the four vertices. This choice of structure mimics the structure of natural rubber with four chains emanating from a given cross-link. The tetrahedron becomes irregular under load and consequently the deformation entropy can be formulated. Mild anisotropy is however introduced by the tetrahedral arrangement and it is not common to see the four-chain model implemented in finite element codes. The eight chain model extends the ideas of the previous two works to consider a cube with chains emanating from the central point to the vertices [Arruda and Boyce, 1993].

These models exploit properties of *idealised* chains, in that interactions with neighbouring chains do not play a role in determining the available conformations. To incorporate this effect, the work by [Heinrich and Kaliske, 1997] introduced the so-called tube model, where a tube is placed around a polymer chain to restrict the number of available conformational states. This work was extended by [Behnke and Kaliske, 2017] and agrees well with experimental observations [Pyckhout-Hintzen et al., 2013]. A generalisation of the structural models to remove reliance on discrete direction would be advantageous. The topic of such a model is presented in the subsequent section.

3.3.1 Microsphere model

The microsphere model represents a generalisation of the three, four and eight chain models introduced by [Kuhn and Grün, 1942], [James and Guth, 1943] and [Arruda and Boyce, 1993] respectively. A key property of the microsphere model, first introduced by [Miehe et al., 2004], is that the polymer chains are oriented in every direction to the surface of a unit sphere. In addition, assumptions about the deformation on the macroscale and microscale are separated into two groups; affine and non-affine chain deformation.

The affine chain assumption implies that the stretch in a given direction on the macroscale is identical to that on the microscale, i.e. a single chain stretch. This assumption is not strictly valid due to neighbouring chains, and therefore the non-affine assumption assumes that the relationship between the micro- and macro-scale can be described by a *flux* about a mean state.

Affine model with Gaussian chains

In the microsphere model, an Eulerian setting is used to derive the Kirchhoff stress and the material tangent operator using the Oldroyd rate. This leads to the following definition for the Kirchhoff stress

$$\boldsymbol{\tau} = 2\frac{\partial \Psi(\bar{\mathbf{F}}, \boldsymbol{g})}{\partial \boldsymbol{g}} \tag{3.11}$$

and the material tangent operator

$$\mathbb{C} = 4\frac{\partial \Psi(\bar{\mathbf{F}}, \boldsymbol{g})}{\partial \boldsymbol{g} \partial \boldsymbol{g}} \; . \tag{3.12}$$

The microsphere model presented by [Miehe et al., 2004] is derived using the free energy function for a non-Gaussian chain. In the current presentation, the non-Gaussian chain adds additional complexity, so a rederivation of the microsphere model enabling the use of Gaussian chains is provided here. This requires prior knowledge of the microsphere model and follows the notation in [Miehe et al., 2004].

It is useful to repeat the notation of the unit sphere homogenisation operator. This is denoted by angled brackets and homogenises a quantity over the unit sphere

$$\langle (\cdot) \rangle = \frac{1}{A_s} \int_0^{A_s} (\cdot) \, \mathrm{d}A \; , \tag{3.13}$$

where A_s is the surface area of a sphere. Computer implementation requires the discretisation of the integral over the unit sphere and this is typically accomplished with Gaussian type quadrature schemes of the form

$$\bar{\boldsymbol{\tau}}_f = 3nkT \sum_{i=0}^{m} \boldsymbol{t}_i \otimes \boldsymbol{t}_i w_i \; , \tag{3.14}$$

where m is the number of integration points on the surface of the unit sphere. It should be noted that several publications caution against using unit sphere integration models due to concerns regarding the introduction of anisotropy and inaccuracy [Verron, 2015, Itskov, 2016]. This was observed in numerical experiments to some degree, but with the appropriate selection of integration scheme the error can be kept well below 1%. See Appendix C.3 for a comparison of numerical error and anisotropy introduced by different numerical integration schemes, model types and strain states.

To begin, consider the macro-Kirchhoff stress

$$\bar{\boldsymbol{\tau}}_f = \left\langle n\frac{\mathrm{d}\psi_f(\lambda)}{\mathrm{d}\lambda}\bar{\lambda}^{-1} \, \boldsymbol{t} \otimes \boldsymbol{t} \right\rangle \tag{3.15}$$

where n is the cross-link density, $\boldsymbol{t} = \bar{\mathbf{F}} \cdot \boldsymbol{r}$ and $\boldsymbol{r}$ are the Lagrangian direction vectors to a point on the surface on the unit sphere, see Figure 3.2d and $\bar{\lambda}$ is the so called *macro-stretch* about which the micro-stretches fluctuate [Miehe et al., 2004]. Here $\bar{\mathbf{F}}$ is the unimodular deformation gradient, viz.,

$$\bar{\mathbf{F}} = (\det \mathbf{F})^{-\frac{1}{3}} \, \mathbf{F} \; . \tag{3.16}$$

The departure from non-Gaussian theory occurs in the choice of the derivative of the chain free energy function, where the derivative term becomes

$$\frac{\mathrm{d}\psi_f(\lambda)}{\mathrm{d}\lambda} = 3kT\lambda \tag{3.17}$$

which results in

$$\bar{\boldsymbol{\tau}}_f = \left\langle 3nkT\lambda\,\bar{\lambda}^{-1}\,\boldsymbol{t}\otimes\boldsymbol{t}\right\rangle . \tag{3.18}$$

Using the affine assumption that $\bar{\lambda} = \lambda$, the Kirchhoff expression becomes

$$\bar{\boldsymbol{\tau}}_f = 3nkT\left\langle \boldsymbol{t}\otimes\boldsymbol{t}\right\rangle , \tag{3.19}$$

which involves only the homogenisation of the deformation through $\boldsymbol{t}\otimes\boldsymbol{t}$. The micro material tangent is expressed as

$$\bar{\mathbb{C}}_f = \left\langle n\left(\frac{\mathrm{d}^2\psi_f}{\mathrm{d}\lambda^2} - \frac{\mathrm{d}\psi_f}{\mathrm{d}\lambda}\bar{\lambda}^{-1}\right)\bar{\lambda}^{-2}\,\boldsymbol{t}\otimes\boldsymbol{t}\otimes\boldsymbol{t}\otimes\boldsymbol{t}\right\rangle \tag{3.20}$$

where the second derivative is no longer dependent on the stretch

$$\frac{\mathrm{d}^2\psi_f}{\mathrm{d}\lambda^2} = 3kT \tag{3.21}$$

and

$$\frac{\mathrm{d}\psi_f}{\mathrm{d}\lambda}\bar{\lambda}^{-1} = 3kT\lambda\,\lambda^{-1} = 3kT . \tag{3.22}$$

The difference between these two expressions is zero and leads to the key result

$$\bar{\mathbb{C}}_f = \boldsymbol{0} . \tag{3.23}$$

In other words, Gaussian chains do not contribute a stiffness term and the material tangent is comprised entirely of the volumetric free energy term and the contribution from the Lie derivative, viz.,

$$\mathbb{C} = (\kappa + p)\boldsymbol{g}^{-1}\otimes\boldsymbol{g}^{-1} - 2\,p\mathbb{I}$$
$$+ \mathbb{P} : \left(\bar{\mathbb{C}}_f + \frac{2}{3}(\bar{\boldsymbol{\tau}} : \boldsymbol{g})\mathbb{I} - \frac{2}{3}(\bar{\boldsymbol{\tau}}\otimes\boldsymbol{g}^{-1} + \boldsymbol{g}^{-1}\otimes\bar{\boldsymbol{\tau}})\right) : \mathbb{P} . \tag{3.24}$$

A detailed derivation of the Kirchhoff stress and the material tangent is provided in Appendix C.

The standard microsphere model uses the Langevin chain theory in order to compute the free energy function and the corresponding Kirchhoff stress and material tangent representation. This probability function does not necessarily need to be non-Gaussian and can be substituted for a Gaussian distribution, which results in simplified expressions for stress and the material tangent, as already seen. Despite the shortcomings of the Gaussian model, the simplified representation will be advantageous when coupling the microsphere model with the ageing formulation in the Gaussian chain framework.

Non-affine network model

Since the ability for the Gaussian statistics to account for the finite extensibility of the polymer chains is very limited, the extension to non-Gaussian chain statistics is commonly made by the use of the so-called *Inverse Langevin* probability density function

$$p_f(\lambda) = p_0 \exp\left[-N\left(\lambda_r \beta + \ln \frac{\beta}{\sinh \beta}\right)\right] \tag{3.25}$$

where $\beta = \mathscr{L}^{-1}(\lambda_r)$ and is given by the Padé approximation

$$\mathscr{L}^{-1}(\lambda_r) = \lambda_r \frac{3 - \lambda_r^2}{1 - \lambda_r^2} \ . \tag{3.26}$$

Other approximations of the inverse Langevin function and a comparison of their relative accuracy are given in [Jedynak, 2015].

The non-affine micro-sphere model introduces a split of the micro free energy as

$$\psi = \psi_f + \psi_c \tag{3.27}$$

where ψ_f is the micro free energy associated with the chain force and ψ_c is the micro free energy associated with the tube constraint. The non-affine microsphere model introduces a term to include the tube given as a probability density function

$$p_c(\nu) = p_o \exp\left[-\alpha \left(\frac{r_0}{d_0}\right)^2 \nu\right] \ . \tag{3.28}$$

Computing the relationship to the free energy is the same as before

$$\psi_c = -k\theta \ln p_c(\nu) \tag{3.29}$$

$$= \alpha k\theta \left(\frac{r_0}{d_0}\right)^2 \nu + \psi_0 \tag{3.30}$$

where d_0 is the tube diameter in the initial configuration. Recall that $r_0 = \sqrt{N}l$ and this simplifies (3.30) to

$$\psi_c = \alpha k\theta N \left(\frac{l}{d_0}\right)^2 \nu + \psi_0 \ . \tag{3.31}$$

The force from the forest chains can be computed through differentiation of the free energy function

$$F_c = \frac{\mathrm{d}\psi_c}{\mathrm{d}\nu} = \alpha k\theta N \left(\frac{l}{d_0}\right)^2 \ . \tag{3.32}$$

The resulting increase in complexity is well rewarded, as the non-affine Langevin microsphere model is able to closely reproduce the complex behaviour of elastomers [Miehe et al., 2004].

Chapter 4

Oxidative ageing

Elastomers are subject to several forms of attack which negatively and irreversibly affect the material properties. These forms of attack are grouped into various categories, but the main concern of this dissertation is chemical ageing whereby the internal structure of the elastomer is changed through the action of radiation and oxygen ingress which modifies the internal molecular network. It is primarily driven by two main factors; chain scission and cross-link formation which are represented schematically in Figure 4.1. These two main effects are in competition and act to cause softening and stiffening respectively. Phenomena such as permanent set and stiffening of rubber components can be linked to these two mechanisms, but they are not the only source. Both chemical processes can be modelled by an Arrhenius term, which describe the relationship between the temperature and activation energy required in order for a reaction to proceed. These are predominately first order reactions and depending on the molecular structure will exhibit different ageing behaviour [Hossain, 2010].

(a) Polymer network with oxygen

(b) Oxygen attack resulting in scission and cross-linking
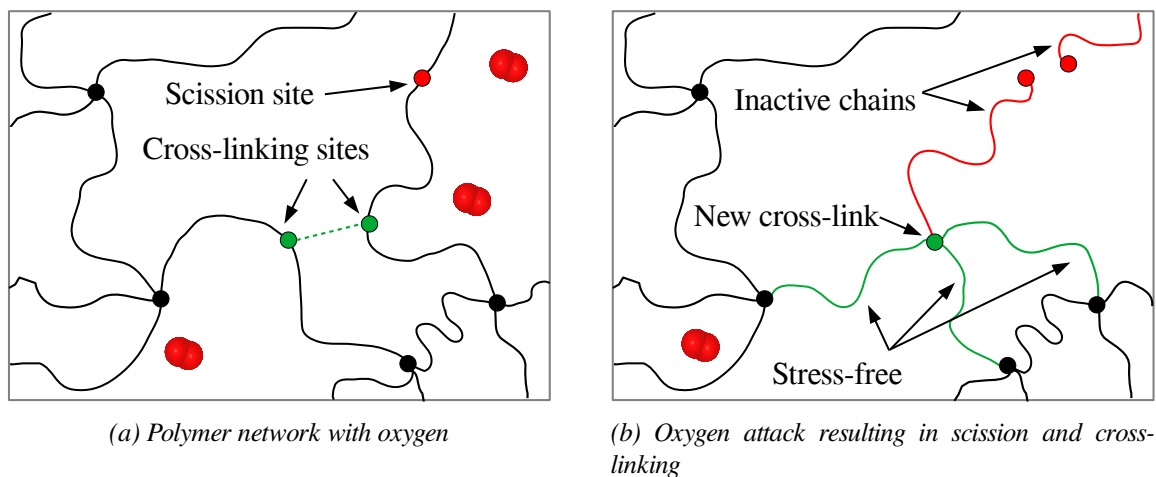
Figure 4.1: Cross-linking and chain scission process

Earlier experimental work demonstrated that the degree of stress relaxation, permanent set and stiffness changes vary for different elastomer recipes. It has long been postulated that a particular reaction mechanism, such as scission or cross-linking, could dominate the overall mechanical response [Tobolsky et al., 1944]. The rate at which these reactions proceed is heavily dependent on the available oxygen and temperature, especially for components where a gradient exists between regions with excess oxygen and no oxygen. An experimental methodology was proposed in [Herzig et al., 2015] in order to quantify the up-

take of oxygen. In this contribution, a homogeneous state of ageing will be assumed, where the sample has excess oxygen in order to drive the oxidative ageing reactions. Extensions to include heterogeneous ageing are possible but increase model complexity and experimental validation is very difficult.

4.1 Chain scission

Chain scission involves the destruction of chemical bonds in the presence of heat or radiation. It can occur via a radical or non-radical process. An example of chain scission by oxygen attack with elevated temperature that proceeds via a non-radical process is shown in Figure 4.2. When a bond is broken, free radicals may form situated at the new free end. The free radical chain reaction will continue until the free radicals are quenched by forming a bond with another free radical which often causes chain cross-linking, see Figure 4.4.
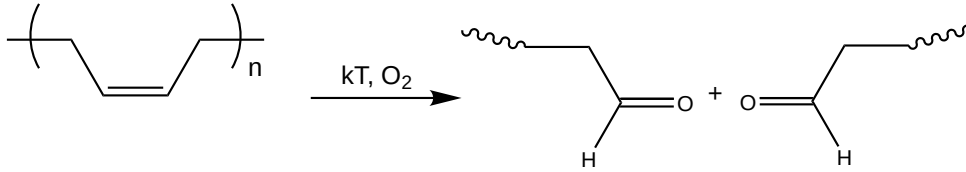
Figure 4.2: Proposed mechanism for chain scission

Oxygen availability and temperature T cause the carbon-carbon double bond to be broken and replaced with oxygen at the two ends according to some rate k. These reactions directly effect the statistical distribution of the number of segments per chain N. Such modelling has been performed using random scission and recombination processes resulting in a set of differential equations, albeit with a focus on volatile production, see [Staggs, 2002, Staggs, 2004].

Suppose that between any two cross-links there is an average rate that a chain segment scission event will occur for each segment as represented by p_s. The probability density function of a single chain with N segments surviving a scission is given by an exponential distribution as

$$R_{cs}(t) = [\exp(-p_s t)]^N = \exp(-p_s N t) \ . \tag{4.1}$$

This is interpreted as the probability at time t that the chain has not been scissioned when subject to a constant scission rate p_s. Note that the exponential distribution has been selected, in part, due to its memoryless property which mimics the physics behind indiscriminate reactions excluding capping effects. The complementary probability of (4.1) is probability density function for a chain failure, viz.,

$$P_{cs}(t) = 1 - \exp(-p_s N t) \ . \tag{4.2}$$

A failure density function can be introduced as the time derivative of (4.2) as

$$\frac{\mathrm{d}P_{cs}}{\mathrm{d}t} = p_s(N + \dot{N}t) \exp\left(-p_s N t\right) \ . \tag{4.3}$$

Integrating the failure density function between two times provides the probability that at least one chain has failed during the integrated time period. For the sake of simplicity, it is assumed that only one event can occur in a time period Δt. The instantaneous rate of failures is given then by (4.3).

The probability distribution function of a chain scission event is non-linearly dependent on the number of segments. In Figure 4.3, the influence of the number of segments on the probability of a chain scission
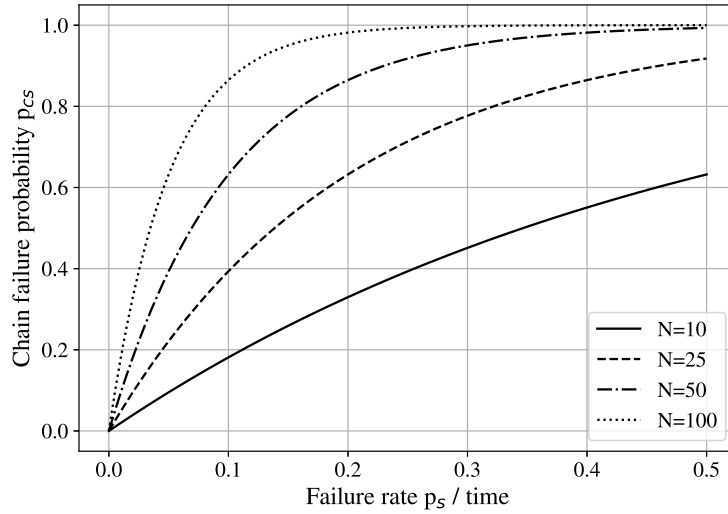
Figure 4.3: Effect of single failure rate and number of segments per chain on chain failure probability after a unit time

can be observed for different chain lengths and rates. Even for small values of p_s, the effect of increasing the number of segments per chain causes the probability of a given chain to undergo scission to increase. The average failure rate depends strongly on external factors, such as temperature and oxygen concentration, and the composition of the elastomer including any anti-ageing additives. For the purposes of this simplified theory these effects are ignored but can be included through a modification of p_s.

In polymer networks with a statistical distribution of segment lengths, the longer segments will be aggressively targeted for particular events. The original chain length distribution will then skew towards shorter chain lengths. A corollary of this model is that polymers with shorter chains will have less likelihood of undergoing an event. This highlights a deficiency in this model, where the probability also needs to include the cross-link points.

4.2 Secondary network formation

A particular challenge with the ageing process is the formation of the secondary network as shown in Figure 4.1. During secondary network formation, polymer bonds are formed in a zero stress state in reference to the deformation at their instance of creation. To further complicate the modelling effort, this process occurs continuously over time with new bonds potentially forming in reference to multiple deformation states. This introduces a strong dependence on the deformation history, however as will be seen later this can be mitigated through the use of Gaussian chain theory.

This secondary network formation has been previously handled in phenomenological models with convolution integrals [Lion and Johlitz, 2012] or through a two-network approach [Naumann, 2017]. Secondary network formation is observed through *permanent set*, whereby a sample does not return to its original configuration upon release after being loaded over a period of time [Andrews et al., 1946]. The percentage difference between the initial and the final stress-free deformation is recorded as the permanent set of the sample.

From a micro-mechanical standpoint, cross-links can form at particular sites along the polymer chain depending on the cross-linking mechanism, e.g., the free-radical process resulting in an oxygen cross-link in Figure 4.4. The reaction is split into multiple mechanisms starting with elevated temperature T and a
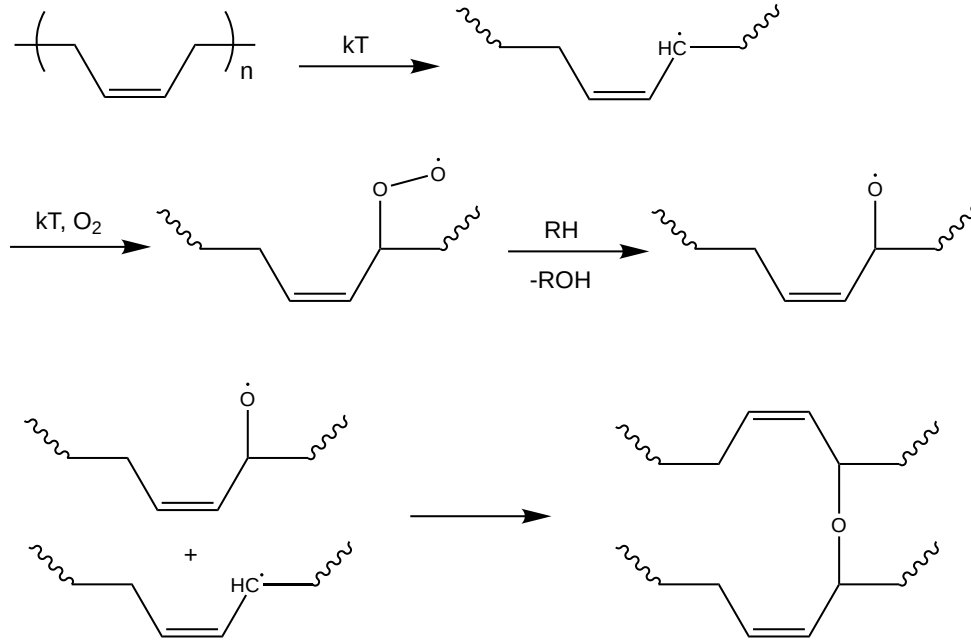
Figure 4.4: Proposed multistage mechanism for cross-linking reaction resulting in oxygen cross-link

reaction rate of k. This leads to the introduction of an unpaired electron (radical) on the carbon adjacent to the carbon-carbon double bond. In the next step, oxygen is introduced and seeks to lower the energy through a bond with the unbalanced electron. Further reaction with an organic compound or side group (RH) and loss of an organic alcohol compound (ROH) breaks the oxygen-oxygen bond and leads to a single oxygen radical. Finally, the oxygen radical lowers its energy by bonding with a free radical on a neighbouring chain and an oxygen cross-link is formed.

Additional cross-links can be viewed as geometric constraints of the newly formed chain. These additional constraints are referred to as forest chains, as they weave around the single chain forming complex structural interactions. The non-affine microsphere model and variants of the tube model include the effect of these forest chains which act as a radial constraint to chain deformation [Heinrich and Kaliske, 1997, Miehe et al., 2004, Behnke and Kaliske, 2017]. The cross-linking process is similar to the inclusion of forest chains, in that it introduces constraints to chain movement that were not previously present [Edwards, 1965]. A Gaussian based statistical mechanics view of the cross-linking process is given in Appendix B.

Consider a deformed polymer network at some time τ_c with a stretch $\lambda(t)$. Let a chain be created in a stress-free configuration with an end-to-end distance $r(\tau_c)$. The stretch experienced by the newly created chain, denoted by $\hat{\lambda}(t, \tau_c)$, with respect to the deformed (or current) configuration can be expressed using (3.4) as

$$\hat{\lambda}(t, \tau_c) = \frac{r(t)}{\hat{r}(\tau_c)} \, , \tag{4.4}$$

where $\hat{r}(\tau_c)$ is the end-to-end distance at the instance when the chain is created and is equivalent to $r(t)$. This ratio can be represented in terms of the global stretch when the chain was created and the current stretch through a multiplicative decomposition

$$\hat{\lambda} = \lambda \, \hat{\lambda}_0^{-1} = \left(\frac{r}{r_0} \right) / \left(\frac{\hat{r}}{r_0} \right) = \frac{r}{\hat{r}} \, . \tag{4.5}$$

31

Chains created at different deformation states are expected to exhibit a different force-stretch behaviour. For example, a chain that is created in the rest state exerts less force than a chain created in a smaller stretch state. This effect is clearly shown in Figure 4.5. Here a fictitious specimen is ramped to a stretch of 5 and then returned to the original stretch. A series of chains are created during the initial ramp stage (indicated by circles in Figure 4.5) and held for a period of time and returned to the original position. A key
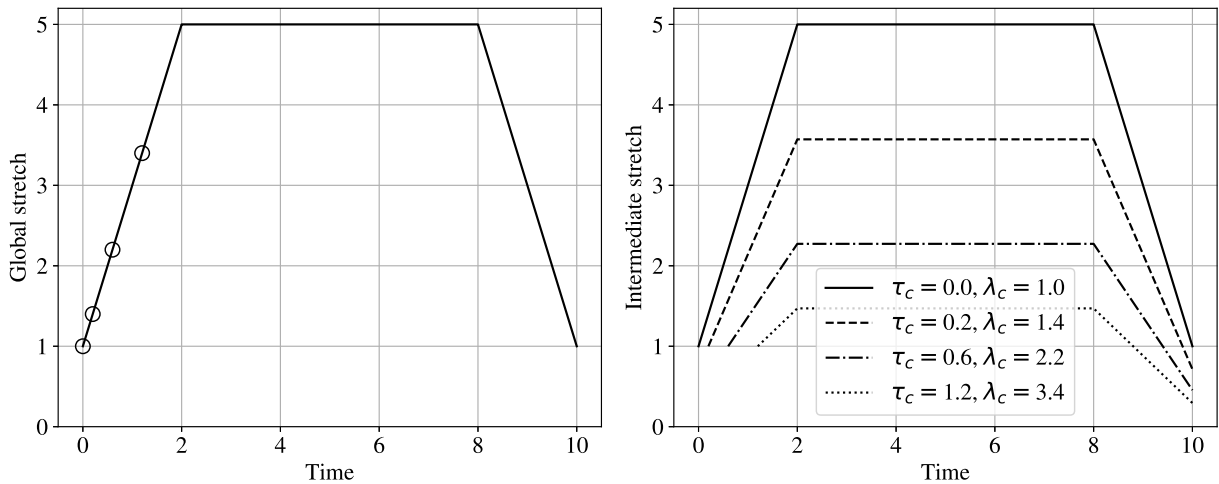
Figure 4.5: Global and intermediate stretch history for chains created at different times and stretches λ_c. Circles indicate creation time of secondary networks and units are omitted for illustration purposes

feature of the intermediate stretch is the development of a residual stretch, where the stretch becomes less than unity indicating that chains created at later time points are in a state of compression when returned to a stretch of one, see Figure 4.5. These intermediate stretches appear to model the *permanent set* phenomenon, where chains created under a deformation other than at the initial configuration will resist a move back to the original position of the initial chain. This concept will be used in the development of one and three dimensional models in the following sections.

4.3 A review of oxidative ageing models

A clear distinction between phenomenological and micro-mechanically motivated models in the realm of oxidative ageing is difficult to make. Due to the very nature of the physics, some level of knowledge of the underlying process is required in order to reproduce the desired effects. In this section, the following definition is used. Phenomenological models draw their motivation from rheological models or purely mathematical constructs and incorporate parameters which have no underlying physical meaning in order to match the expected material response. In contrast, micro-mechanically motivated models constantly refer to the underlying processes throughout their derivation and material parameters have a physical meaning. Whether the parameters represent the true underlying physics is a matter of model fidelity. Micro-mechanical models begin at the level of chain statistics and attempt to characterise the entropy associated with ageing. However, these models are not typically applied in finite element modelling and industrially relevant models are derived based on phenomenological approaches.

4.3.1 Phenomenological approaches

There are several publications based on a phenomenological approach that attempt to predict the response of elastomers undergoing oxidative ageing. Most of the recent publications trace their origins back to the work of [Hossain et al., 2009b]. Their basic premise is to introduce a rheological type model for small strain curing and then extend this work to a finite strain framework [Hossain et al., 2009a]. Several proposed models tackling the multiphysical aspects of ageing are based on this model, including contributions by [Johlitz et al., 2014, Steinke et al., 2011, Lion and Johlitz, 2012, Johlitz and Lion, 2013, Dippel et al., 2014] and [Herzig et al., 2017].

The general approach in phenomenological models is to decompose the specific free energy function into three parts; a volumetric contribution, an isochoric scission contribution and an isochoric recombination (or secondary network) contribution according to

$$\psi = \psi_{\text{vol}} + \psi_s + \psi_r \ , \tag{4.6}$$

respectively. An appropriate expression for the volumetric contribution ψ_{vol} is covered in Section 3.1. The scission and network reformation can be modelled, for example, through an internal variable p based on a modified Arrhenius law that evolves according to

$$\dot{p} = \nu_p \exp\left(-\frac{E_p}{R\theta}\right)(1-p) \ , \tag{4.7}$$

where ν_p is the prefactor, E_p is the activation energy of the particular reaction, R is the universal gas constant and θ is the absolute temperature. The evolution of p is subject to the following requirements

$$\dot{p} \geq 0, \ 0 \leq p \leq 1, \ p(0) = 0 \ . \tag{4.8}$$

These conditions can be physically motivated as given in [Johlitz et al., 2014].

The scission term ψ_s is provided using the Neo-Hooke free energy function with the time varying material parameter c_{10} as

$$\rho_0 \psi_s = c_{10}(q_s)\left(\text{I}_{\bar{\mathbf{C}}} - 3\right) \ , \tag{4.9}$$

where c_{10} is a material parameter (which in the case of a Neo-Hooke model represents the shear modulus), $\text{I}_{\bar{\mathbf{C}}}$ is the first invariant of the isochoric right Cauchy-Green deformation tensor and q_s is the scission parameter ($0 \leq q_s \leq 1$). The functional form of q_s is taken from (4.7) and given explicitly by

$$\dot{q}_s = \nu_s \exp\left(-\frac{E_s}{R\theta}\right)(1-q_s) \ , \tag{4.10}$$

where q_s is the scission parameter and E_s is the activation energy for the scission reaction. The degradation (scission) of the chains is governed by changes to c_{10}, which is equivalent to the modification of the shear modulus in the Neo-Hooke model. To compute the stress, one can differentiate (4.9) with respect to $\mathbf{C}$ to obtain

$$\mathbf{S}_s = c_{10}(q_s)\mathbf{1} : \frac{\partial \mathbf{C}}{\partial \bar{\mathbf{C}}} \ . \tag{4.11}$$

The secondary network formation is modelled by the introduction of the free energy function

$$\rho_0 \psi_r = \frac{1}{2}\int_0^t \left(\mathbf{\Gamma}^4 : (\mathbf{E}(t) - \mathbf{E}(s))\right) : (\mathbf{E}(t) - \mathbf{E}(s)) \ \text{d}s \tag{4.12}$$

33

where a fourth order tensor is introduced as

$$\mathbf{\Gamma}^4(t) = 2q_r(t)\frac{\partial^2 \omega}{\partial \mathbf{C} \, \partial \mathbf{C}} \; . \tag{4.13}$$

with the free energy function of the secondary network denoted by ω. Note that q_r is the reformation parameter and is computed by replacing q_s, ν_s and E_s with q_r, ν_r and E_r in (4.10) and free energy function ω is taken to be the Neo-Hooke model

$$\omega = d_{10} \left(\mathrm{I}_{\bar{\mathbf{C}}} - 3 \right) \; , \tag{4.14}$$

with an introduction of another material constant d_{10} as the shear modulus of the secondary network. The second Piola-Kirchhoff stresses for the secondary network are given as

$$\mathbf{S}_r = \int_0^t \mathbf{\Gamma}^4(s) : (\mathbf{E}(t) - \mathbf{E}(s)) \, \mathrm{d}s \; . \tag{4.15}$$

After mathematical manipulations the stress rate is expressed as

$$\dot{\mathbf{S}}_r = \mathbf{\Gamma}^4 : \dot{\mathbf{E}}$$
$$= q_r(t)d_{10}\left[-\frac{J^{-\frac{2}{3}}}{3}(\mathbf{C}^{-1} : \dot{\mathbf{C}})\left(\mathbf{1} - \frac{1}{3}\mathrm{I}_{\mathbf{C}}\mathbf{C}^{-1} + \frac{J^{-\frac{2}{3}}}{3}\left(-\mathrm{tr}\left(\dot{\mathbf{C}}\right)\mathbf{C}^{-1} + \mathrm{I}_{\mathbf{C}}\mathbf{C}^{-1}\cdot\dot{\mathbf{C}}\cdot\mathbf{C}^{-1}\right)\right)\right] \tag{4.16}$$

as reported by [Dippel et al., 2014]. Note from (4.16), the creation of the secondary network is stress-free, in the sense that constant strain ($\dot{\mathbf{C}} = \mathbf{0}$) doesn't change the stress. With this formulation q_r plays the role of reducing the influence of the earlier networks. However, there is no explicit degradation of the previously created secondary networks through scission. Using an implicit Euler discretisation of (4.16) we obtain

$$\mathbf{S}_r = \mathbf{S}_r^n + q_r d_{10}\left[-\frac{1}{3}J^{-\frac{2}{3}}\left(\mathbf{C}^{-1} : (\mathbf{C} - \mathbf{C}^n)\right)\left(\mathbf{1} - \frac{1}{3}\mathrm{I}_{\mathbf{C}}\mathbf{C}^{-1}\right)\right.$$
$$\left. + \frac{1}{3}J^{-\frac{2}{3}}\left((\mathrm{tr}\left(\mathbf{C}^n\right) - \mathrm{tr}\left(\mathbf{C}\right))\mathbf{C}^{-1} + \mathrm{I}_{\mathbf{C}}\mathbf{C}^{-1}\cdot(\mathbf{C} - \mathbf{C}^n)\cdot\mathbf{C}^{-1}\right)\right] \tag{4.17}$$

with the explicit $n + 1$ time step notation for $\mathbf{C}$ dropped for simplicity.

A comparison between a model based on this approach and experimental results has been carried out in [Johlitz et al., 2014]. Intermittent stress tests were performed at $60\,^{\circ}\mathrm{C}$, $80\,^{\circ}\mathrm{C}$ and $100\,^{\circ}\mathrm{C}$ for natural rubber with 60 phr (parts per hundred rubber) of carbon black. Difficulty was encountered in fitting the model to the initial period (up until 8.3 hours) but good results were obtained until chemical shrinkage effects occur. Ageing effects were assumed to be homogeneous, ignoring the diffusion limited oxidation (DLO) effect.

Inclusion of the DLO effect was shown in an extension of this work by [Dippel et al., 2014]. The mechanical formulation remained the same, however a reaction-diffusion type reaction, based on Fick's law, was coupled with the evolution equations for q_s and q_r. Experimental work has been presented in [Herzig et al., 2017], where the oxygen consumption results are input into the reaction-diffusion equation that is ultimately entered into the internal variable evolution in (4.7) as

$$\dot{p} = \nu_p \exp\left(-\frac{E_p}{R\theta}\right)(1 - p)r_{\mathrm{ox}} \; , \tag{4.18}$$

where r_{ox} is the oxidation reaction parameter. The DLO effect was clearly depicted through the gradient of oxygen between the outer boundaries of the elastomer and the innermost part. An extensive treatment of linear and non-linear reaction-diffusion equations including saturation effects as applied to oxidative ageing is covered in [Nasdala et al., 2005].

4.3.2 Micro-mechanical approaches

Micro-mechanical approaches typically allow for interpretation of individual mechanisms through physically motivated material parameters. The physics of the underlying problem is typically modelled on a smaller scale than the continuum scale and then homogenised to a continuum level model. A compact summary of the difficulties encountered with micro-mechanical models of oxidative ageing is provided in [Budzien et al., 2008].

The proposed model in [Budzien et al., 2008] will be summarised briefly to highlight the features of the model. The standard decomposition of the Cauchy stress into chemical, physical and volumetric parts is performed. A physical entanglement contribution to the stress is taken from the Slip-Tube model [Rubinstein and Panyukov, 2002]. In order to compute the total stress, the summation over past deformation states in a discrete manner is performed and the state of decay of the network is modelled by a stress-transfer function in [Budzien et al., 2008]. The discrete sum technique leads to a computationally expensive approach, requiring traversal of the entire load history at each new time step in order to compute the contributions of secondary networks to the current stress state. Through the use of the slip-tube model, geometric and loading specific off-line initialisation stage are required, making this method unsuitable for generic large scale finite element simulations.

Recently, a statistically based continuum theory for modelling transient polymer networks was proposed by [Vernerey, 2018]. The statistical mechanics are based on the affine Gaussian chain theory. An evolution equation based on association and deassociation of polymer bonds was introduced to describe changes in the underlying probability distribution. The resulting model was able to reproduce viscoelastic effects. It holds promise as a micro-mechanical oxidative ageing model, where cross-linking causes the chains to become shorter and the corresponding probability distribution will become skewed.

A precursor to the proposed model in this dissertation has been developed by [Rajagopal and Wineman, 1992]. The authors provide insightful motivation behind the two-network theory and use this to introduce basic network dynamics to capture chain movement from scission to secondary network in a one-to-one fashion. However, the secondary networks were not permitted to undergo scission reactions over time. An additional assumption in this model is the fixed number of scission reactions that occur at a particular deformation state. Secondary network formation occurs when the deformation reaches a certain threshold, according to an activation function. The Cauchy stress based on the Neo-Hooke model is decomposed into contributions

$$\boldsymbol{\sigma}_\alpha(t) = b(t)\mu\,\mathbf{b}(t,0) \tag{4.19}$$

and

$$\boldsymbol{\sigma}_\beta(t) = \int_{t_a}^{t} \mu\,a(s)\,\mathbf{b}(s)\,\mathrm{d}s \tag{4.20}$$

from the primary and secondary network respectively. Note that $\mathbf{b}$ is the left Cauchy-Green deformation tensor and $b(t)$ is the volume fraction of remaining portion of original network. It is defined as

$$b(t) = 1 - \int_{t_a}^{t} a(s)\,\mathrm{d}s\,, \tag{4.21}$$

where $a(s)$ is the rate at which chains in the original polymer network undergo scission.

Inspection of the primary network stress reveals a very simple form, where stress-softening behaviour can be recovered by ensuring that $b(t)$ is monotonically decreasing. The secondary network stress does not include a dynamically evolving shear modulus, but rather captured through a change of a. Unfortunately, the paper presented by [Rajagopal and Wineman, 1992] does not present a procedure to include this model in a finite element framework.

4.4 Network dynamics model

To model the changes in the material due to scission and cross-linking, we begin by introducing two sets of polymer chains; active and inactive polymer chains. Chains in the active set are able to support a load whereas inactive chains are not connected at both ends to another chain and cannot support a load. These inactive chains are available to cross-link and move back into the active set, or further undergo a scission reaction. A compartment diagram of these processes is presented in Figure 4.6.
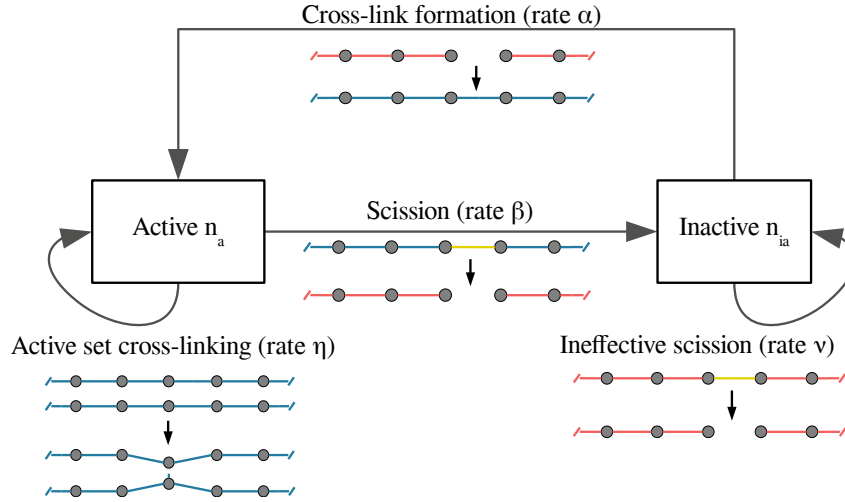
Figure 4.6: Compartment model showing flows between active and inactive sets

To derive a mathematical model of the network dynamics, we let n_a and n_{ia} be the cross-link density in the active set and inactive set respectively. Due to the act of scission and cross-linking changing the length of the chain, N_a and N_{ia} are introduced as the average segment count per chain in the active and inactive sets, respectively. The rates of change between each of the compartments are denoted in Table 4.1.

Table 4.1: Compartment model rate nomenclature

Rate	Symbol
Cross-link formation of an inactive chain	α
Scission of active chain	β
Cross-linking of active chains	η
Scission of inactive chain	ν

Four rate parameters are required to model the movement of chains between sets according to the simplified dynamics presented here. However, it can be shown that these rates are related to two parameters; the rate of a scission reaction p_s and the rate of a cross-linking reaction p_c.

Let p be the average reaction (either scission or cross-linking) event per unit time. The exponential distribution for the probability that a chain with N segments will survive up until time t is given by

$$R_c(t) = [\exp(-pt)]^N \ . \tag{4.22}$$

The complementary probability provides the probability of a chain failure (succumbing to a reaction event)

$$P_c(t) = 1 - R_c(t) = 1 - \exp(-pNt) \tag{4.23}$$

and the failure density function for a single chain with N segments undergoing a reaction (P_{cs}) is given as the time derivative

$$\frac{\mathrm{d}P_c(p, N, \dot{N})}{\mathrm{d}t} = p(N + \dot{N}t)\exp(-pNt) \ , \tag{4.24}$$

with p as the probability of a reaction, be it scission or cross-linking and N as the average segments per chain for either the active or inactive set. We may then write the rates as

$$\alpha = \frac{\mathrm{d}P_c(p_c, N_{ia}, \dot{N}_{ia})}{\mathrm{d}t} \tag{4.25}$$

$$\beta = \frac{\mathrm{d}P_c(p_s, N_a, \dot{N}_a)}{\mathrm{d}t} \tag{4.26}$$

$$\eta = \frac{\mathrm{d}P_c(p_c, N_a, \dot{N}_a)}{\mathrm{d}t} \tag{4.27}$$

$$\nu = \frac{\mathrm{d}P_c(p_s, N_{ia}, \dot{N}_{ia})}{\mathrm{d}t} \ . \tag{4.28}$$

With these results in hand, we can begin by writing the differential equations for the flux between the compartments. Consider the flux from the active set. For active set cross-linking, two chains leave the set and four are created. Likewise, for scission one chain leaves and cross-link formation creates one new cross-link from two inactive chains. Performing the flux balance and accounting for the number of chains moving across the active and inactive sets leads to

$$\frac{\mathrm{d}n_a}{\mathrm{d}t} = -\beta n_a + \alpha n_{ia} + 2\eta n_a \ , \tag{4.29}$$

$$\frac{\mathrm{d}n_{ia}}{\mathrm{d}t} = 2(\beta n_a - \alpha n_{ia}) + \nu n_{ia} \ . \tag{4.30}$$

Up until this point, evolution equations for the average segments per chain have not been considered. Given we have an initial number of segments per chain N_0, and an initial number of chains n_0, the constraint due to mass conservation reads

$$N_a(t)n_a(t) + N_{ia}(t)n_{ia}(t) = N_0 n_0 \ , \tag{4.31}$$

in conjunction with the requirement that

$$\frac{\mathrm{d}}{\mathrm{d}t}\left(N_a(t)n_a(t) + N_{ia}(t)n_{ia}(t)\right) = 0 \ . \tag{4.32}$$

Dropping the explicit dependence on time and expanding (4.32) results in

$$n_a\frac{\mathrm{d}N_a}{\mathrm{d}t} + N_a\frac{\mathrm{d}n_a}{\mathrm{d}t} + n_{ia}\frac{\mathrm{d}N_{ia}}{\mathrm{d}t} + N_{ia}\frac{\mathrm{d}n_{ia}}{\mathrm{d}t} = 0 \ , \tag{4.33}$$

or alternatively

$$n_a\frac{\mathrm{d}N_a}{\mathrm{d}t} + N_a\frac{\mathrm{d}n_a}{\mathrm{d}t} = -n_{ia}\frac{\mathrm{d}N_{ia}}{\mathrm{d}t} - N_{ia}\frac{\mathrm{d}n_{ia}}{\mathrm{d}t} \ . \tag{4.34}$$

This equation does not explicitly provide an evolution equation for N_a or N_{ia}, therefore the compartment diagram is again consulted to perform a molecular mass balance around each set. Performing this balance,

we obtain

$$\frac{\mathrm{d}n_a N_a}{\mathrm{d}t} = -\beta n_a N_a + 2\alpha n_{ia} N_{ia} \tag{4.35}$$

$$\frac{\mathrm{d}n_{ia} N_{ia}}{\mathrm{d}t} = \beta n_a N_a - 2\alpha n_{ia} N_{ia} \ , \tag{4.36}$$

noting that mass is automatically conserved by reactions entering and leaving the same set. Using the product rule to expand the derivatives on the left hand side of (4.35) and (4.36) leads to

$$\frac{\mathrm{d}N_a}{\mathrm{d}t} = \frac{1}{n_a} \left(-\beta n_a N_a + 2\alpha n_{ia} N_{ia} - N_a \frac{\mathrm{d}n_a}{\mathrm{d}t} \right) \tag{4.37}$$

$$\frac{\mathrm{d}N_{ia}}{\mathrm{d}t} = \frac{1}{n_{ia}} \left(\beta n_a N_a - 2\alpha n_{ia} N_{ia} - N_{ia} \frac{\mathrm{d}n_{ia}}{\mathrm{d}t} \right) \ . \tag{4.38}$$

A keen reader will note the singularity encountered for $n_a = 0$ and $n_{ia} = 0$. While theoretically permissible, elastomers are rarely cured to completion and inactive chains, to the amount of a few percent, will exist which prevent numerical instabilities in practical computations[1].

Using these equations, a simplified network model is introduced resulting in a set of coupled non-linear differential equations amounting to the following initial value problem:

$$\frac{\mathrm{d}n_a}{\mathrm{d}t} = \alpha n_{ia} + 2\eta n_a - \beta n_a \tag{4.39}$$

$$\frac{\mathrm{d}n_{ia}}{\mathrm{d}t} = 2\beta n_a + (\nu - 2\alpha)n_{ia} \tag{4.40}$$

$$\frac{\mathrm{d}N_a}{\mathrm{d}t} = \frac{1}{n_a} \left(-\beta N_a n_a + 2\alpha N_{ia} n_{ia} - N_a \frac{\mathrm{d}n_a}{\mathrm{d}t} \right) \tag{4.41}$$

$$\frac{\mathrm{d}N_{ia}}{\mathrm{d}t} = \frac{1}{n_{ia}} \left(\beta N_a n_a - 2\alpha N_{ia} n_{ia} - N_{ia} \frac{\mathrm{d}n_{ia}}{\mathrm{d}t} \right) \tag{4.42}$$

alongside the creation rate

$$\frac{\mathrm{d}n_c}{\mathrm{d}t} = \alpha n_{ia} + 4\eta n_a \ , \tag{4.43}$$

where n_c is the number of created chains per unit volume. The importance of (4.43) will become apparent when the amount of secondary network formation enters into the mechanical model. Before (4.39) to (4.42) can be solved, the matter of suitable initial values must be settled. For simplicity, the active cross-link density can be determined from the shear modulus relationship $\mu = nkT$. The inactive cross-link density is assumed to be a small value of the active cross-link density. Several alternate initial values are possible. For example, polymers are typically not fully cured, rather they are cured to some percentage of full cure, such as T95 (95% cured). Therefore a suitable non-zero initial value for n_{ia} can be computed from the shear modulus. The initial number of average segments per chain in the active and inactive set is selected as 60 and 0 respectively. Selection of physically realistic initial conditions for N_a and N_{ia} is postponed until a later section.

For the time discretisation an adaptive explicit fourth-fifth order Runge-Kutta method has been chosen. The results of holding the rate of scission p_s constant and varying the rate of cross-linking p_c are provided in Figure 4.7.

---

[1]The correctness of (4.37) and (4.38) can be verified by substitution into (4.33)
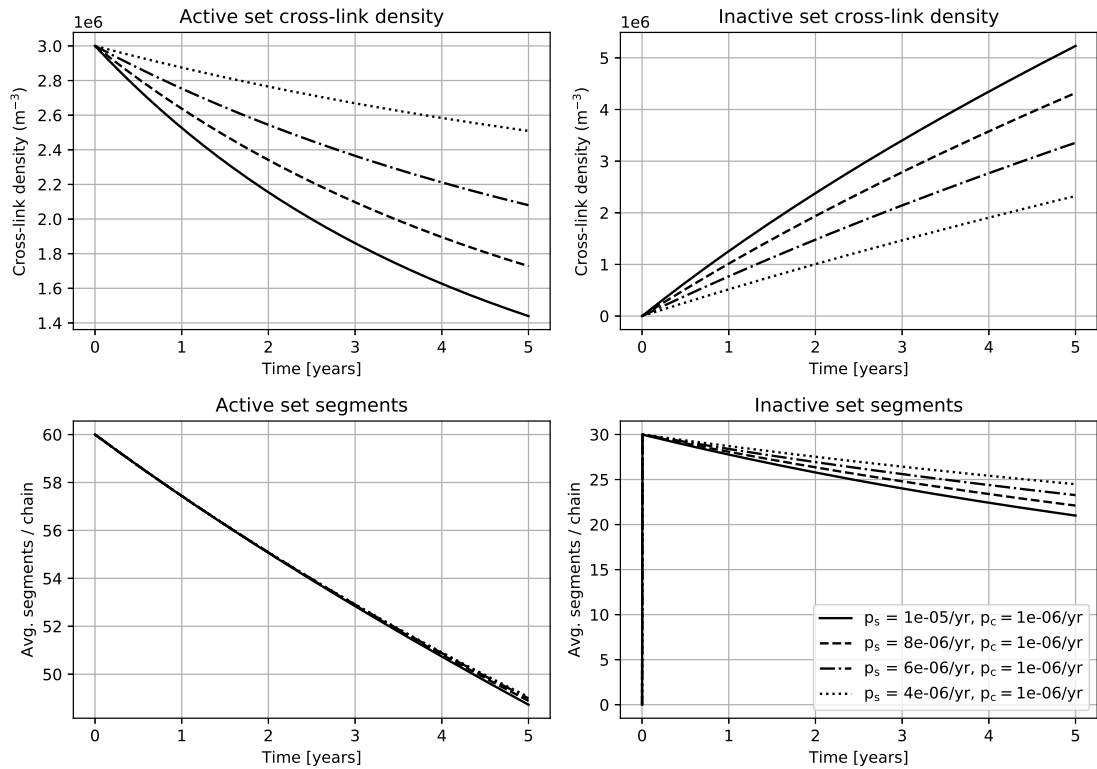
Figure 4.7: Cross-link density and average segment length evolution varying p_c

Varying the rate of cross-linking demonstrates a strong influence of p_c on the cross-link density in the active set as chains are cross-linked with neighbouring chains. The active cross-link density increases while the average segments per chain in the active set decreases in order to maintain mass balance. Scission of active chains leads to the creation of inactive chains, which accumulate in the inactive compartment depending on the value of p_c. Higher values of p_c result in fewer inactive chains as these undergo cross-linking reactions to move back into the active set. The overall effect of higher values of p_c is to increase the rate at which the cross-link and average segments per chain decrease.

By holding the rate of cross-linking constant and varying the rate of scission the effect of scission on the cross-link density and average segments per chain is shown in Figure 4.8. Higher rates of scission strongly influence the cross-link density of the active set by moving chains into the inactive set. However, with low enough rates, the cross-linking will dominate and cause an increase of the cross-link density in the active set. Inspection of the average segments per chain indicates a weak dependence of the average segments per chain evolution on the scission probability.

To determine the suitability of numerical methods to the solution of this initial value problem, a comparison between an implicit Euler method and the adaptive fourth order Runga-Kutta (RK45) method will be carried out. Details pertaining to the linearisation of the network equations for the implicit method are provided in Appendix D. A comparison of implicit and explicit first order methods and the multistep methods in the Runga-Kutta family of integrators is provided in Figure 4.9.

The first order explicit and implicit method appear to under and over estimate the solution, respectively, compared to the adaptive RK23 and RK45 methods for relatively large time step sizes. No significant difference between the Runga-Kutta integrators can be observed. The deviation of the first order methods reduces as the time step decreases, see Figure 4.10, however the loose coupling of these equations to the
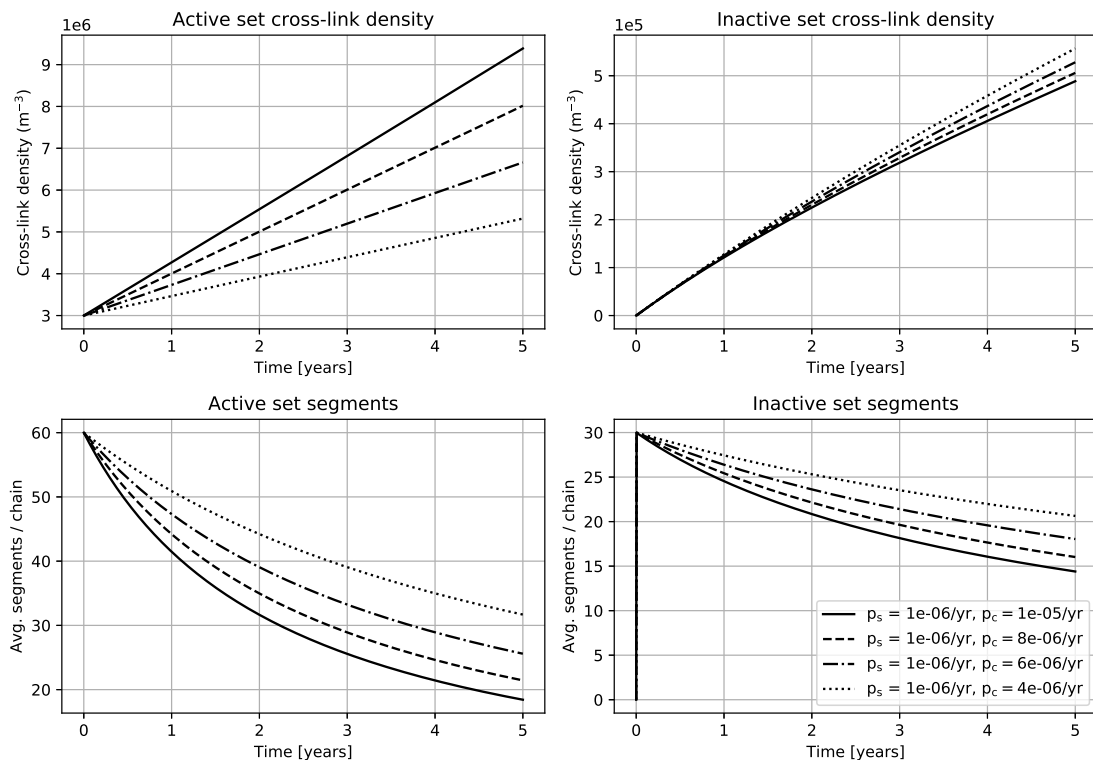
Figure 4.8: Cross-link density and average segment length evolution varying p_c

mechanical model affords flexibility in the choice of time integrator.

Chemical ageing computations involve vastly different time scales between the mechanical and chemical dynamics. Typical time scales for mechanical models are in the order of seconds (e.g. cyclic loading), while chemical ageing operates on the order of months to years (at moderate temperature). A conservative estimate of time step sizes of a single day demonstrate little difference between time integration schemes owing to the slow chemical dynamics. It can be concluded that lower order methods provide acceptable accuracy when time steps are sufficiently small, although explicit methods, such as RK23, can be used to reduce computational cost compared to the linear solves required by implicit methods. The compartment model presented here will be extended in Section 4.5 to accommodate the mechanical model.

4.5 One dimensional model

Before attempting to derive a continuum model for chemical ageing, a simplified one-dimensional model will be presented. Many concepts explored here will be reused during the derivation of the continuum model. From Section 4.4, it has been seen that changes to both the cross-link density and the average segments per chain occur over time. How these changes effect the force developed by a group of one-dimensional polymer chains is the topic of this section.

Recall the force of a single chain derived from Gaussian chain statistics

$$f_c(\lambda) = 3kT\lambda . \tag{4.44}$$

The primary deformation measure here is the stretch λ. At a rest state, $\lambda = 1$ and the force in the chain is
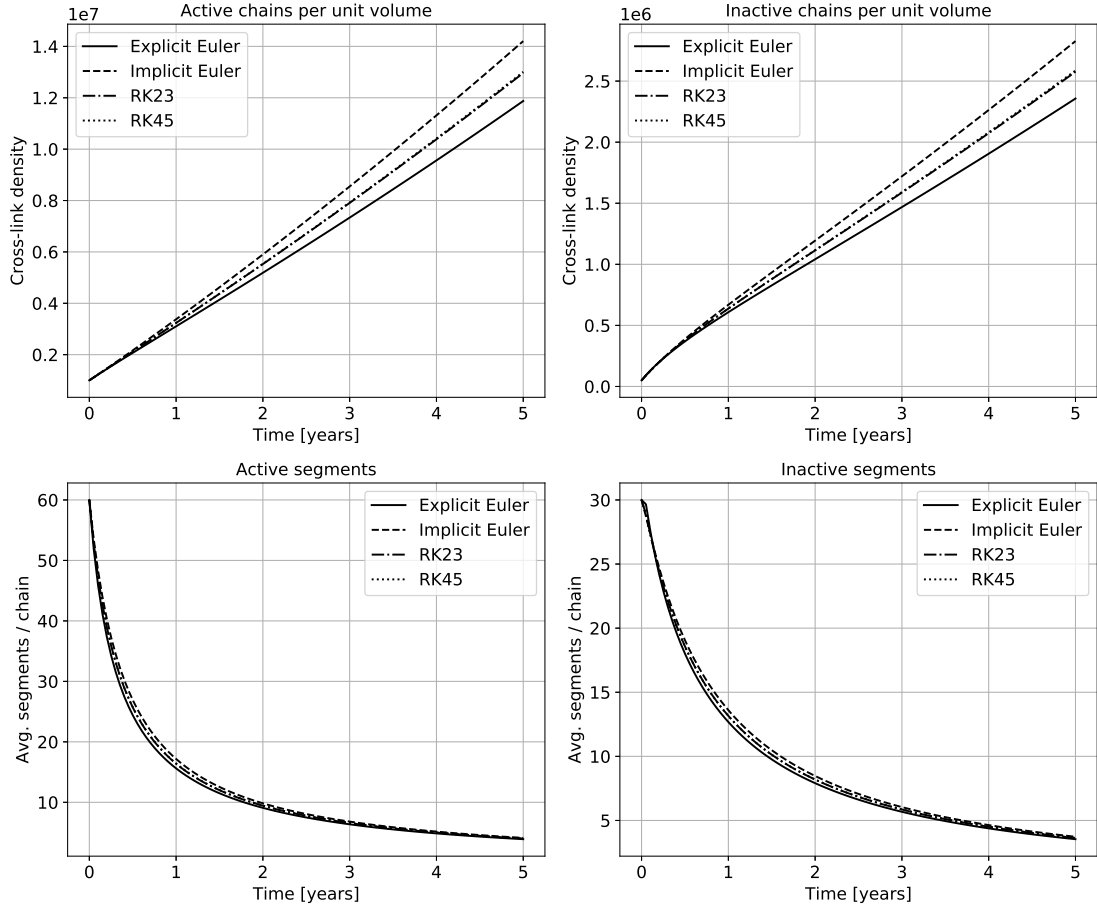
Figure 4.9: Comparison of implicit and explicit time integration with $\Delta t = 18.5$ days, $n_a(0) = 1.0 \cdot 10^6$ cross-links / volume, $n_{ia}(0) = 5.0 \cdot 10^4$ cross-links / volume, $N_a(0) = 60$ segments, $N_{ia}(0) = 30$ segments, $p_s = 2.0 \cdot 10^{-5}$ / year and $p_c = 6.0 \cdot 10^{-5}$ / year

non-zero. A group (or bundle) of polymer chain develops a force according to

$$F_c = 3nkT\lambda \tag{4.45}$$

where n is the cross-link density. In the parlay of this dissertation a more appropriate definition is

$$F_c = 3n_akT\lambda \ . \tag{4.46}$$

The forces developed by this chain group are highly dependent on n_a, and the force follows similar curves to those found in Figures 4.7 and 4.8 for constant k, T and λ. At this stage, the stress softening behaviour seen in experiments should be readily reproducible with suitable network parameters p_s and p_c, and the resulting n_a in (4.46). An underlying assumption of the Gaussian statistics is that the chains are sufficiently long and the number of segments N_a does not play a role. The Gaussian assumption is not able to account for increases in stiffness due to decreases in the number of segments per chain. The non-Gaussian (Langevin) statistical theory is better suited to model the so-called *up turn* that is observed when polymer chains reach their finite extensibility limits or the force changes due to changes of segment length. The chain force from non-Gaussian theory is given by

$$f_c = kT\sqrt{N_a}\mathcal{L}^{-1}(\lambda_r) \tag{4.47}$$
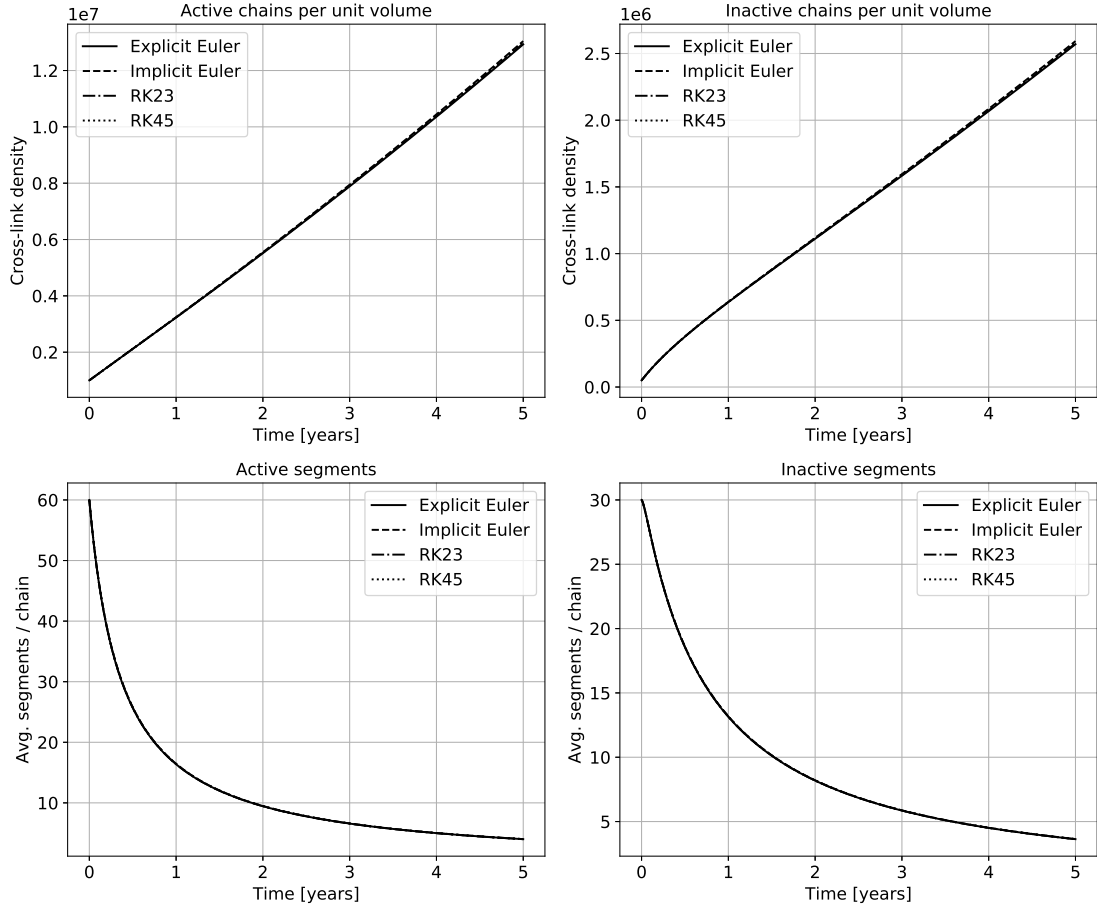
Figure 4.10: Comparison of implicit and explicit time integration with $\Delta t = 1$ day, $n_a(0) = 1.0 \cdot 10^6$ cross-links / volume, $n_{ia}(0) = 5.0 \cdot 10^4$ cross-links / volume, $N_a(0) = 60$ segments, $N_{ia}(0) = 30$ segments, $p_s = 2.0 \cdot 10^{-5}$ / year and $p_c = 6.0 \cdot 10^{-5}$ / year

where $\lambda_r = \lambda/\sqrt{N_a}$. The inverse Langevin function is difficult to evaluate directly, so the Padé approximation

$$\mathcal{L}^{-1}(\lambda_r) = \lambda_r \frac{3 - \lambda_r^2}{1 - \lambda_r^2} \tag{4.48}$$

can be used instead. An analysis of the error for this choice can be found in [Jedynak, 2015]. This expression can capture the changes in force associated with changes in average segments per chain. As will be seen later, the role of N_a in the force expression leads to complexities in the secondary network formation.

In order to treat the chain scission and cross link formation, the effects will be split and handled separately. It makes sense to first develop a simple Gaussian based model so the physics behind cross-linking can be explored in a simplified framework without the appearance of N_a. With the stress-softening effect handled as previously discussed, the major challenge is the inclusion of the continuous creation of a secondary network in a stress-free state [Tobolsky et al., 1961, Dippel et al., 2014].

The basis of this formulation relies on the Gaussian chain statistics [Treloar, 1975], [Doi and Edwards, 1988]. Recall the free energy of an idealised single Gaussian chain (omitting the dependence on time)

$$\psi_f = \frac{3}{2} kT \hat{\lambda}^2 + \psi_0 \tag{4.49}$$

42

where k is the Boltzmann constant, T is the absolute temperature and $\hat{\lambda}$ is the stretch relative to the configuration where the chain was created, see (4.5). Note that the intermediate stretch decays to the stretch when the chain was created in the reference (or initial) configuration. The force of a single chain created in an arbitrary intermediate configuration is then

$$f_c = \frac{\partial \psi_f}{\partial \lambda} = 3kT\hat{\lambda} \ . \tag{4.50}$$

By introducing a polymer network comprised of n_a initial active chains we obtain an expression for n_a chains as

$$F = 3n_a kT\hat{\lambda} \ . \tag{4.51}$$

Let a secondary network be formed at time τ_c where $0 < \tau_c \leq t$. The secondary network at time τ_c is created with $n_c(\tau_c)$ chains. To simplify the derivation, we introduce a vertical bar that represents a quantity at a given time instant. Here we set the number of chains created at τ_c to be $n_c\Big|_{\tau_c}$ and let the number of remaining active chains at time τ from the group of chains created at τ_c be $n_a\Big|_{\tau_c}$.

Using the compartment model, the current number of chains per unit volume is given as the initial created amount minus the chains removed through scission or further cross-linking. Expressing this as an integral we obtain an equation for the remaining active chains per unit volume as

$$n_a(t)\Big|_{\tau_c} = n_c\Big|_{\tau_c} - \int_{\tau_c}^{t} [\beta + 2\eta] n_a(\tau)\Big|_{\tau_c} \ \mathrm{d}\tau \ . \tag{4.52}$$

A crucial observation made by [Tobolsky et al., 1944] is that the secondary network is created in a stress-free configuration. This effect can be captured by introducing an intermediate configuration (as in Figure 2.2), where the deformation that the chains experience is based on the intermediate configuration upon which it was created.

By multiplicatively decomposing the chain stretch as

$$\lambda = \hat{\lambda}(t)\lambda(\tau_c) \ , \tag{4.53}$$

we are able to substitute (4.52) and (4.53) into (4.51) to obtain an expression of the force from a secondary network created on an intermediate configuration at τ_c as

$$f(t) = 3kT \left(n_c\Big|_{\tau_c} - \int_{\tau_c}^{t} [\beta + 2\eta] n_a(\tau)\Big|_{\tau_c} \ \mathrm{d}\tau \right) \hat{\lambda} \ , \tag{4.54}$$

and factoring out $n_c\Big|_{\tau_c}$ provides

$$f(t) = 3kT n_c\Big|_{\tau_c} \left(1 - \int_{\tau_c}^{t} [\beta + 2\eta] \frac{n_a(\tau)}{n_c}\Big|_{\tau_c} \ \mathrm{d}\tau \right) \hat{\lambda} \ . \tag{4.55}$$

At this point it is useful to define a dimensionless value γ that represents the fraction of active chains remaining from the original number of chains created in a secondary network as

$$\gamma(\tau) = \frac{n_a(\tau)}{n_c}\Big|_{\tau_c} \ , \tag{4.56}$$

by assuming $n_c > 0$, which then provides an expression for the force in a single secondary network created at τ_c as

$$f(t) = 3kTn_c\Big|_{\tau_c} \left(1 - \int_{\tau_c}^t [\beta + 2\eta]\gamma(\tau) \ \mathrm{d}\tau\right)\hat{\lambda} \ . \tag{4.57}$$

To simplify further expressions, a local reduction factor, denoted by Γ, is defined by

$$\Gamma(t,\tau) = 1 - \int_{\tau_c}^t [\beta + 2\eta]\gamma(\tau) \ \mathrm{d}\tau \ . \tag{4.58}$$

The force contribution from a single secondary network can be written compactly as

$$f(t) = 3kTn_c\Big|_{\tau_c} \Gamma(t,\tau_c)\hat{\lambda} \ . \tag{4.59}$$

Recognising that the term $n_c\Big|_{\tau_c} \Gamma(t,\tau_c)$ is nothing more than the number of active chains per unit volume in the secondary network created at τ_c, we can simplify (4.59) using (4.52) to yield the intuitive expression

$$f(t) = 3kTn_a(t)\Big|_{\tau_c} \hat{\lambda} \ . \tag{4.60}$$

The decay rate of a secondary network created at time τ_c, according to the compartment model in Figure 4.6, is only permitted to decay through chain scission. This assumption generates an expression for the change of active chains in a secondary network (without loss of generality) as

$$\dot{n}_a(\tau)\Big|_{\tau_c} = -n_a(\tau)\Big|_{\tau_c} (\beta + 2\eta) \tag{4.61}$$

which is solved subject to the initial conditions $n_a(\tau_c)\Big|_{\tau_c} = n_c\Big|_{\tau_c}$. Using (4.56), we can write (4.61) in terms of γ

$$\dot{\gamma}(\tau)\Big|_{\tau_c} = -\gamma(\tau)\Big|_{\tau_c} (\beta + 2\eta) \tag{4.62}$$

subject to initial condition $\gamma(\tau_c)\Big|_{\tau_c} = 1$. Since the term $\beta + 2\eta$ is identical across secondary networks for a given time τ, we select two arbitrary times $\tau_c^{(1)}$ and $\tau_c^{(2)}$, where $\tau_c^{(1)} < \tau_c^{(2)}$ which allows us to write

$$\frac{\dot{\gamma}(\tau)}{\gamma(\tau)}\Big|_{\tau_c^{(1)}} = \frac{\dot{\gamma}(\tau)}{\gamma(\tau)}\Big|_{\tau_c^{(2)}}$$
$$= -(\beta + 2\eta) \ . \tag{4.63}$$

With this information we observe only the relative changes are significant which allows us to construct a global function such that

$$\dot{\hat{\gamma}}(t) = -\hat{\gamma}(t)(\beta + 2\eta) \tag{4.64}$$

with an initial condition $\hat{\gamma}(0) = 1$. A mapping from the global to the local non-dimensionalised chain decay can be constructed as

$$\gamma(\tau)\Big|_{\tau_c} = \frac{\hat{\gamma}(\tau)}{\hat{\gamma}(\tau_c)} \ , \tag{4.65}$$
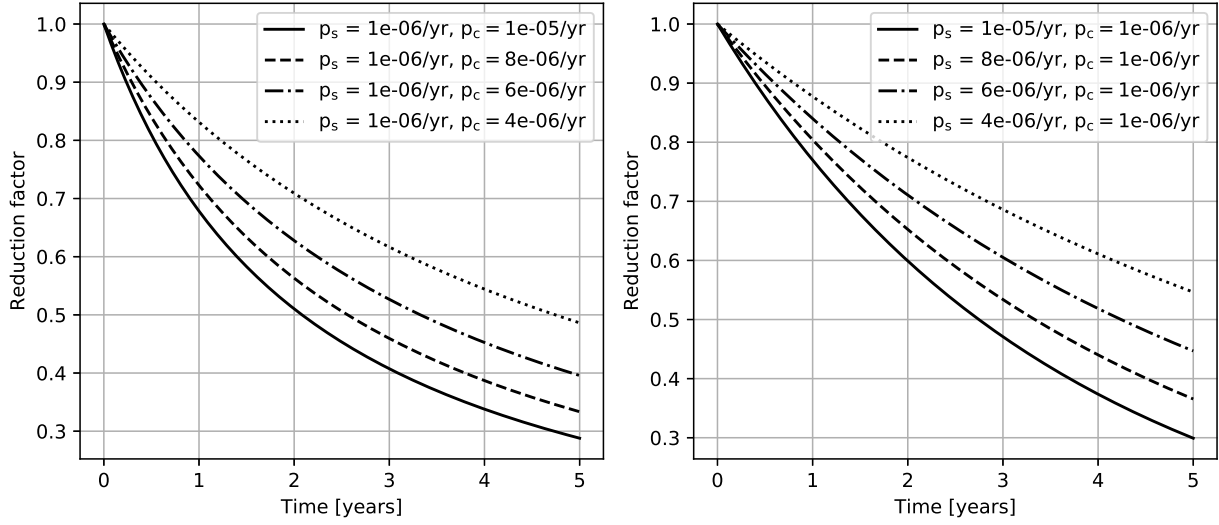
Figure 4.11: Reduction factor for various network parameters

or alternatively in rate form

$$\dot{\gamma}(\tau)\Big|_{\tau_c} = \frac{\dot{\hat{\gamma}}(\tau)}{\hat{\gamma}(\tau_c)} \ . \tag{4.66}$$

The solution of the reduction factor is shown in Figure 4.11 for initial conditions $n_a = 3.4 \cdot 10^6$ chains / volume, $n_{ia} = 0$ chains / volume, $N_a = 60$ segments per chain, $N_{ia} = 0$ segments per chain and $\gamma(0) = 0$.

Compared to previous oxidative ageing models, the reduction factor plays the role of exponential decay for both the scission and network reformation parameters, see (4.10). Both p_s and p_c have a similar effect on accelerating network degradation. The reduction factor is significantly more than merely a measure of the network decay, it opens the gateway to computing the amount an arbitrary secondary network has decayed at time t since its construction at time $\tau < t$.

Rewriting the reduction factor in (4.58) using (4.62) gives

$$\Gamma(t, \tau_c) = 1 - \int_{\tau_c}^{t} (\beta + 2\eta)\gamma(\tau) \ \mathrm{d}\tau \tag{4.67}$$

$$= 1 + \int_{\tau_c}^{t} \dot{\gamma}(\tau) \ \mathrm{d}\tau \ . \tag{4.68}$$

By substituting (4.66) into (4.68) we obtain an expression valid for any secondary network given by

$$\Gamma(t, \tau_c) = 1 + \frac{1}{\hat{\gamma}(\tau_c)} \int_{\tau_c}^{t} \dot{\hat{\gamma}} \ \mathrm{d}\tau \ . \tag{4.69}$$

Applying the first fundamental theorem of calculus to (4.69) simplifies the reduction factor to

$$\Gamma(t, \tau_c) = 1 + \frac{1}{\hat{\gamma}(\tau_c)} \left[\hat{\gamma}(t) - \hat{\gamma}(\tau_c)\right] = \frac{\hat{\gamma}(t)}{\hat{\gamma}(\tau_c)} \ . \tag{4.70}$$

Substituting in (4.53) for $\hat{\lambda}$ into (4.59) and performing an integral over time to capture the continuous formation of the secondary network, provides an expression for the force of a chain bundle

$$f_\beta(t) = 3kT \left[\int_0^t \dot{n}_c\Big|_{\tau_c} \Gamma(t, \tau_c)\lambda^{-1}(\tau_c) \ \mathrm{d}\tau_c\right] \lambda(t) \ . \tag{4.71}$$

45

where subscript β denotes the secondary network contribution to the force. Substituting (4.70) into (4.71) yields the force contribution from the continuously forming secondary network

$$f_\beta(t) = 3kT \left[\int_0^t \dot{n}_c \Big|_{\tau_c} \hat{\gamma}^{-1}(\tau_c)\lambda^{-1}(\tau_c) \ \mathrm{d}\tau_c \right] \hat{\gamma}(t) \ \lambda(t) \ . \tag{4.72}$$

It is now possible to write an expression for the force from the initial network as

$$f_\alpha(t) = 3kT\hat{\gamma}(t)n_a(0)\lambda \ . \tag{4.73}$$

Exploiting superposition of forces in a polymer network can be written as

$$f(t) = f_\alpha(t) + f_\beta(t) \tag{4.74}$$

and for completeness

$$f(t) = 3kT \left(n_a(0) + \int_0^t \dot{n}_c(\tau_c)\hat{\gamma}^{-1}(\tau_c)\lambda^{-1}(\tau_c) \ \mathrm{d}\tau_c \right) \hat{\gamma}(t)\lambda(t) \ . \tag{4.75}$$

For the purposes of a one-dimensional model, the chains are arranged into an impromptu three-dimensional structure to mimic the structure in the Neo-Hooke model. Insight can be gained by plotting the force-stretch response of the primary and secondary network. However, the forces must be post-processed as in the rest state. The force exerted by a chain is non-zero and adding new chains to the system will appear to increase the force of the sample. An adhoc deviatoric form is introduced for values of $i = \{1, 2, 3\}$ and is expressed by

$$\bar{f}_i = f_i - \frac{1}{3}(f_1 + f_2 + f_3) \ . \tag{4.76}$$

Force in the primary network follows the increase in stretch, decays over time and then returns to the zero (rest) force state. The decay in the primary network is purely driven by changes to n_a. Inspection of the secondary deviatoric force reveals that the secondary networks are formed in a force-free state and the secondary network only provides a force reaction when attempting to return the sample to the original position when the network was created in the deformed configuration. Superposition of the primary and secondary networks demonstrates stress softening followed by a permanent set effect, whereby the force is negative, indicating compression, when the sampled is returned to its original configuration. If the sample was not required to return to the original position, then the secondary network would work against the primary network and the new equilibrium position would lie between the original and deformed configuration. The decay in the force can be attributed to the reduction factor and the exponential type decay observed in Figure 4.12d. Creation of new secondary networks is initially high and decays over time.

For the purposes of deriving the general three-dimensional theory, the one-dimensional model provides an excellent introduction to the concepts of intermediate stretches, network dynamics coupling and history integration. However, serious challenges were encountered when attempting to translate the one-dimensional theory into a suitable micro-mechanical constitutive model as the influence of an arbitrary deformation history is not captured by this one-dimensional approach. An extension to include the deformation gradient is the topic of the subsequent sections.

4.6 Continuum model

As eluded to in the previous section, the derivation of the three-dimensional model deviates very slightly from the one-dimensional model. For the generalised model, the microsphere model will be used. This model is not strictly required, however the flexibility provided by this model means that other effects, such as Mullins effect, can be introduced by using off-the-shelf models from the literature.

(a) Stretch (uniaxial)

(b) Nominal force of primary and secondary network

(c) Creation rate of new cross-links

(d) Reduction factor
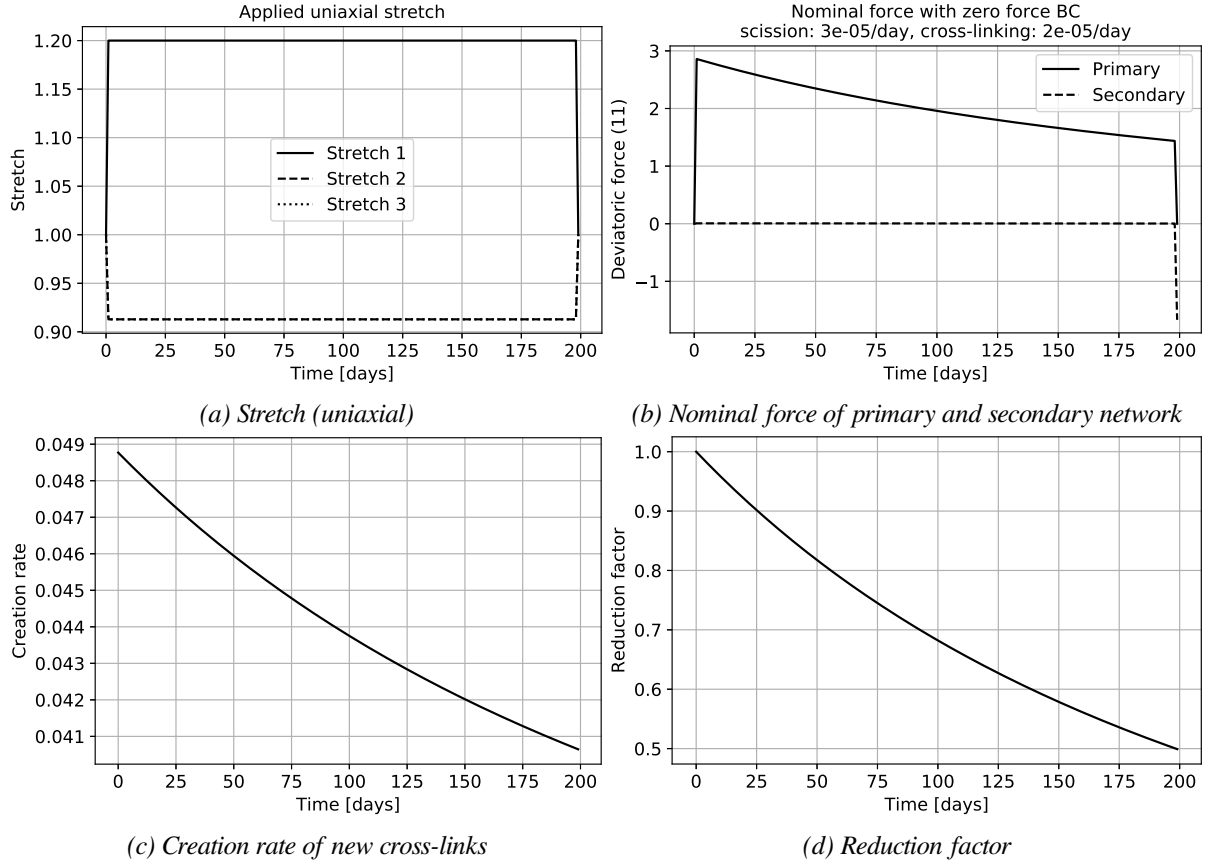
Figure 4.12: Load and force response for primary and secondary network in deviatoric space with initial conditions $n_a(0) = 10.0$ cross-links / volume, $n_{ia}(0) = 0.01$ cross-links / volume, $N_a(0) = 60$ segments, $N_{ia}(0) = 30$ segments, $p_s = 3.0 \cdot 10^{-5} \mathrm{d}^{-1}$, $p_c = 2.0 \cdot 10^{-5} \mathrm{d}^{-1}$

4.6.1 Intermediate configuration

Following on from the previous section, let the intermediate deformation gradient be given by $\hat{\mathbf{F}}$ as the generalisation of $\hat{\lambda}$. Let $\hat{\bar{\mathbf{S}}}_\beta \big|_{\tau_c}$ be the macro-second Piola-Kirchhoff stress of a secondary network on an intermediate configuration at time τ_c. The expression for macro-second Piola-Kirchhoff at the point of creation $\mathbf{F} = \mathbf{1}$ on some intermediate configuration is given by

$$\hat{\bar{\mathbf{S}}}_\beta \Big|_{\tau_c} = 3n_c(\tau_c)kT \langle \boldsymbol{r} \otimes \boldsymbol{r} \rangle \ , \tag{4.77}$$

where $n_c(\tau_c)$ is the created cross-link density at time τ_c. Note that the homogenisation of $\boldsymbol{r}$ around the sphere is given by

$$\langle \boldsymbol{r} \otimes \boldsymbol{r} \rangle = \frac{1}{3} \mathbf{1} \tag{4.78}$$

leading to a simplified form of the macro-second Piola-Kirchhoff stress on an intermediate stress-free configuration as

$$\hat{\bar{\mathbf{S}}}_\beta \Big|_{\tau_c} = n_c(\tau_c)kT \mathbf{1} \ . \tag{4.79}$$

47

If a substitution for the shear modulus $\mu_c = n_c(\tau_c)kT$ is made, then the expression becomes

$$\hat{\bar{\mathbf{S}}}_\beta \Big|_{\tau_c} = \mu_c(\tau_c)\,\mathbf{1} \; , \tag{4.80}$$

which is nothing more than the second Piola-Kirchhoff stress before a deviatoric projection for the compressible Neo-Hooke model. At some point in time, the push forward of $\hat{\bar{\mathbf{S}}}\Big|_{\tau_c}$ using the elastic part of the deformation gradient leads to

$$\bar{\boldsymbol{\tau}}_\beta \Big|_{\tau_c} = \hat{\gamma}^{-1}(\tau_c)\mu(\tau_c)\,\bar{\mathbf{F}}_e \cdot \bar{\mathbf{F}}_e^{\mathrm{T}} \; , \tag{4.81}$$

as the stress contribution of a secondary network created at time τ_c. Note that as before, we can write

$$\bar{\mathbf{F}}(t) = \bar{\mathbf{F}}_e \cdot \bar{\mathbf{F}}(\tau) \tag{4.82}$$

or equivalently

$$\bar{\mathbf{F}}_e = \bar{\mathbf{F}}(t) \cdot \bar{\mathbf{F}}(\tau)^{-1} \; . \tag{4.83}$$

Proceeding with the substitution of (4.83) into (4.81) furnishes

$$\bar{\boldsymbol{\tau}}_\beta \Big|_{\tau_c} = \bar{\mathbf{F}}(t) \cdot \bar{\mathbf{F}}^{-1}(\tau_c)\hat{\gamma}^{-1}(\tau_c)\mu_c(\tau_c) \cdot \bar{\mathbf{F}}(\tau_c)^{-\mathrm{T}} \cdot \bar{\mathbf{F}}(t)^{\mathrm{T}} \; . \tag{4.84}$$

Each secondary network contribution is integrated over time to form the secondary Kirchhoff stress

$$\bar{\boldsymbol{\tau}}_\beta(t) = \hat{\gamma}(t)\bar{\mathbf{F}}(t) \cdot \left[\int_0^t \hat{\gamma}^{-1}(\tau)\dot{\mu}_c(\tau)\,\bar{\mathbf{F}}^{-1}(\tau) \cdot \bar{\mathbf{F}}^{-\mathrm{T}}(\tau)\,\mathrm{d}\tau \right] \cdot \bar{\mathbf{F}}(t)^{\mathrm{T}} \; . \tag{4.85}$$

where the mapping of the reduction factor in (4.65) was used. For the purposes of simplification, let $\bar{\mathbf{S}}_\beta(t)$ be defined as

$$\bar{\mathbf{S}}_\beta(t) = \int_0^t \hat{\gamma}^{-1}(\tau)\dot{\mu}_c\,\bar{\mathbf{C}}^{-1}(\tau)\,\mathrm{d}\tau \; , \tag{4.86}$$

where $\bar{\mathbf{C}}^{-1} = \bar{\mathbf{F}}^{-1} \cdot \bar{\mathbf{F}}^{-\mathrm{T}}$. This enables the compact representation

$$\bar{\boldsymbol{\tau}}_\beta(t) = \hat{\gamma}(t)\bar{\mathbf{F}}(t) \cdot \bar{\mathbf{S}}_\beta(t) \cdot \bar{\mathbf{F}}(t)^{\mathrm{T}} \; . \tag{4.87}$$

Application of the chain rule and the first theorem of calculus allows the alternative representation of (4.86) as

$$\frac{\mathrm{d}\bar{\mathbf{S}}_\beta(t)}{\mathrm{d}t} = \dot{\mu}_c(t)\,\hat{\gamma}^{-1}(t)\,\bar{\mathbf{C}}^{-1}(t) \; , \tag{4.88}$$

to be solved subject to the initial condition

$$\bar{\mathbf{S}}_\beta(0) = \mathbf{0} \; . \tag{4.89}$$

The topic of the implementation and solution of these equations in a finite element setting is covered in a subsequent section.

4.6.2 Thermodynamic consistency

For a constitutive model to be thermodynamically valid the Clausius-Duhem theorem must be satisfied. The constitutive model presented in Section 4.6.1 must be analysed to ensure it is thermodynamically consistent. Consider the isochoric free energy in the reference configuration of the primary network

$$\bar{\Psi}_\alpha = \hat{\gamma}(t)\mu_a(0)(\mathrm{I}_{\bar{\mathbf{C}}} - 3) \ . \tag{4.90}$$

Application of the Clausius-Duhem inequality to (4.90) in the reference configuration leads to the expression

$$\mathbf{P}_\alpha : \dot{\mathbf{F}} - \dot{\Psi}_\alpha \geq 0 \tag{4.91}$$

$$\mathbf{P}_\alpha : \dot{\mathbf{F}} - \left(\frac{\partial \Psi_\alpha}{\partial \hat{\gamma}} \dot{\hat{\gamma}} + \frac{\partial \Psi_\alpha}{\partial \mathbf{F}} : \dot{\mathbf{F}} \right) \geq 0 \tag{4.92}$$

and with the usual arguments, namely

$$\mathbf{P}_\alpha : \dot{\mathbf{F}} = \frac{\partial \Psi_\alpha}{\partial \mathbf{F}} : \dot{\mathbf{F}} \tag{4.93}$$

we obtain

$$- \left[\mu_a(0)(\mathrm{I}_{\bar{\mathbf{C}}} - 3) \right] \dot{\hat{\gamma}} \geq 0 \ , \tag{4.94}$$

which satisfies the Clausius-Duhem inequality if

$$\dot{\hat{\gamma}} \leq 0 \tag{4.95}$$

since the standard free energy function for the Neo-Hooke model is positive. For the proposed network dynamics model, this requires that

$$\beta + 2\eta \geq 0 \tag{4.96}$$

which leads to inequality

$$\left(N_a + \dot{N}_a t \right) \left[\underbrace{p_s \exp\left(-p_s N_a t \right) + 2p_c \exp\left(-p_c N_a t \right)}_{\geq 0} \right] \geq 0 \ . \tag{4.97}$$

Consequently, thermodynamic consistency demands that

$$N_a + \dot{N}_a t \geq 0 \ , \tag{4.98}$$

for which a closed-form inequality is not readily obtainable due to the coupled and non-linear structure of the network dynamics equations. The value for t should be considered as a characteristic time from the beginning of a time step to the end. That is it applies locally to the time step inasmuch it applies to the entire simulation where the limit of (4.98) as $t \to \infty$ are no longer of principle concern. From an implementation perspective, the negativity of $\dot{\hat{\gamma}}$ should be asserted during the computation and in the unlikely scenario the sign is positive the computation should be terminated. Likewise, time step sizes are now constrained to ensure that initially high rates of N_a or N_{ia} are captured properly by sufficiently small time step sizes. Experience with practical computations has shown that reasonable parameters and time step sizes do not cause problems.

For the secondary network, the task is slightly more arduous due to the nature of the integral. From (4.85) the second Piola-Kirchhoff stress is computed by the pull back of the metric $\boldsymbol{g} = \mathbf{1}$ on the intermediate configuration to the reference configuration by

$$\bar{\mathbf{S}}_\beta = \hat{\gamma}(t) \int_0^t \hat{\gamma}^{-1}(\tau)\dot{\mu}_c(\tau)\, \bar{\mathbf{F}}^{-1}(\tau) \cdot \boldsymbol{g} \cdot \bar{\mathbf{F}}^{-\mathrm{T}}(\tau)\, \mathrm{d}\tau \tag{4.99}$$

and replacing the pull back of the metric with the right isochoric Cauchy Green tensor

$$\bar{\mathbf{S}}_\beta = \hat{\gamma}(t) \int_0^t \hat{\gamma}^{-1}(\tau)\dot{\mu}_c(\tau)\, \bar{\mathbf{C}}^{-1}(\tau)\, \mathrm{d}\tau \tag{4.100}$$

or in terms of the first Piola-Kirchhoff stress

$$\bar{\mathbf{P}}_\beta = \bar{\mathbf{S}}_\beta \cdot \bar{\mathbf{F}}^{\mathrm{T}}(t) = \int_0^t \hat{\gamma}^{-1}(\tau)\dot{\mu}_c(\tau)\, \bar{\mathbf{C}}(\tau)^{-1}\, \mathrm{d}\tau \cdot \bar{\mathbf{F}}^{\mathrm{T}}(t) \;. \tag{4.101}$$

The second Piola-Kirchhoff stress can be pushed forward to the current configuration if desired. Performing the thermodynamic analysis on (4.99) yields

$$\mathbf{P} : \dot{\mathbf{F}} - \dot{\Psi} \geq 0 \tag{4.102}$$

with the isochoric part of the free energy function postulated to be

$$\bar{\Psi}_\beta = \frac{1}{2} \int_0^t \hat{\gamma}^{-1}(\tau)\dot{\mu}_c(\tau) \det \bar{\mathbf{C}}(\tau)\, \mathrm{d}\tau \;. \tag{4.103}$$

Writing the inequality assuming the volumetric part of the free energy function is well behaved yields

$$\mathbf{P} : \dot{\mathbf{F}} - \left(\frac{\partial \bar{\Psi}_\beta}{\partial \hat{\gamma}}\dot{\hat{\gamma}} + \frac{\partial \bar{\Psi}_\beta}{\partial \det \bar{\mathbf{C}}} : \frac{\partial \det \bar{\mathbf{C}}}{\partial \bar{\mathbf{C}}} : \frac{\partial \bar{\mathbf{C}}}{\partial \mathbf{C}} : \frac{\partial \mathbf{C}}{\partial \mathbf{F}} : \dot{\mathbf{F}} \right) \geq 0 \tag{4.104}$$

allows the term $\mathbf{P} : \dot{\mathbf{F}}$ to cancel and the inequality becomes

$$-\dot{\gamma}(t) \int_0^t \hat{\gamma}^{-1}(\tau)\dot{\mu}_c(\tau) \det \bar{\mathbf{C}}(\tau)\, \mathrm{d}\tau \geq 0 \tag{4.105}$$

Provided that $\dot{\gamma}(t) \leq 0 \; \forall \, t$ and that

$$\int_0^t \hat{\gamma}^{-1}(\tau)\dot{\mu}_c(\tau) \det \bar{\mathbf{C}}(\tau)\, \mathrm{d}\tau \geq 0 \tag{4.106}$$

holds, then the inequality holds. The strain tensor relation $\det \bar{\mathbf{C}}$ is always positive. Assuming that $\gamma(t)$ does not reach zero, $\hat{\gamma}^{-1}(t)$ is always positive. However, $\dot{\mu}_c$ may not always be positive. Although thermodynamic consistency requires the integral to be positive, transients into negative rates could pose a problem. Consider the following inequality arising from the requirement $\dot{\mu}_c \geq 0$:

$$\left(N_{ia} + \dot{N}_{ia}t \right) \underbrace{\exp\left(-p_c N_{ia} t\right) n_{ia}}_{\geq 0} + 4 \left(N_a + \dot{N}_a t \right) \underbrace{\exp\left(-p_c N_a t\right) n_a}_{\geq 0} \geq 0 \;. \tag{4.107}$$

Requirements placed on the primary network, namely $N_a + \dot{N}_a t \geq 0$, mean that one additional constraint

$$N_{ia} + \dot{N}_{ia}t \geq 0 \;, \tag{4.108}$$

is required since all other terms are greater than zero. This completes the proof that this model is thermodynamically consistent, provided the network model ensures that the reduction factor rate is strictly negative and that $N_{ia} + \dot{N}_{ia}t \geq 0$ holds with the choice of appropriate time step sizes.

4.6.3 Implementation

The network dynamics equations (4.39) to (4.42) and (4.64) need to be solved as a coupled system of equations. For convenience, the cross-link density will be converted into a shear modulus with the relationship $\mu = nkT$, viz.,

$$\frac{\mathrm{d}\mu_a}{\mathrm{d}t} = \alpha\mu_{ia} + 2\eta\mu_a - \beta\mu_a \tag{4.109}$$

$$\frac{\mathrm{d}\mu_{ia}}{\mathrm{d}t} = 2\beta\mu_a + (\nu - 2\alpha)\mu_{ia} \tag{4.110}$$

$$\frac{\mathrm{d}N_a}{\mathrm{d}t} = \frac{1}{\mu_a}\left(-\beta N_a\mu_a + 2\alpha N_{ia}\mu_{ia} - N_a\frac{\mathrm{d}\mu_a}{\mathrm{d}t}\right) \tag{4.111}$$

$$\frac{\mathrm{d}N_{ia}}{\mathrm{d}t} = \frac{1}{\mu_{ia}}\left(\beta N_a\mu_a - 2\alpha N_{ia}\mu_{ia} - N_{ia}\frac{\mathrm{d}\mu_{ia}}{\mathrm{d}t}\right) \tag{4.112}$$

$$\frac{\mathrm{d}\hat{\gamma}}{\mathrm{d}t} = -\hat{\gamma}(\beta + 2\eta) \ . \tag{4.113}$$

The values used in the constitutive model are μ_c (see (4.43)) and $\hat{\gamma}$ and the remaining equations are for numerical book keeping. Explicit methods are able to handle the non-linearities of the right hand side with ease. However an implicit method leads to Newton-Raphson iterations involving the solution of a 5x5 system of equations. Naturally, this is computationally more expensive and because there is no evidence to suggest that these equations are stiff, the use of an implicit time integration scheme is not required.

The computer implementation of (4.88) involves the discretisation of the differential operator. For simplicity, the implicit Euler discretisation is given for a time n to $n + 1$ as

$$\bar{\mathbf{S}}_\beta^{n+1} = \Delta t\,(\gamma^{-1})^{n+1}\,\dot{\mu}_c^{n+1}\,\left(\bar{\mathbf{C}}^{-1}\right)^{n+1} + \bar{\mathbf{S}}_\beta^n \tag{4.114}$$

where the terms on the right hand side are evaluated with the updated values. The rate $\dot{\mu}_c^{n+1}$ is given by the evaluation of the right hand side of (4.43). The total secondary stress is finally computed through

$$\bar{\boldsymbol{\tau}}_\beta^{n+1} = \gamma^{n+1}\bar{\mathbf{F}}^{n+1} \cdot \bar{\mathbf{S}}_\beta^{n+1} \cdot \left(\bar{\mathbf{F}}^{\mathrm{T}}\right)^{n+1} \tag{4.115}$$

Performing the discretisation on the primary network Kirchhoff stress gives

$$\bar{\boldsymbol{\tau}}_\alpha^{n+1} = 3\mu_0\gamma^{n+1}\langle\boldsymbol{t}^{n+1} \otimes \boldsymbol{t}^{n+1}\rangle \tag{4.116}$$

with $\boldsymbol{t}^{n+1} = \bar{\mathbf{F}}^{n+1} \cdot \boldsymbol{r}$. The total Kirchhoff stress is given by

$$\bar{\boldsymbol{\tau}}^{n+1} = \bar{\boldsymbol{\tau}}_\alpha^{n+1} + \bar{\boldsymbol{\tau}}_\beta^{n+1} \ . \tag{4.117}$$

The material tangent is evaluated directly from (3.24) using the updated total macro-Kirchhoff stress in (4.117). No modifications are required to the material tangent due to the nature of Gaussian chains. The push forward of a zero micro-tangent in an intermediate configuration will result in a zero micro-tangent in the current configuration. An interested reader can review C.2 for a derivation to confirm this is correct.

Inspection of (4.117) reveals the high computational efficiency of this method. The secondary network requires the storage of the previous secondary Kirchhoff stress and only two matrix multiplications and two matrix additions. In the finite element method, these stresses are integrated at each Newton-Raphson iteration. This formulation leads to a very computationally inexpensive internal variable update, which is advantageous for the potentially expensive ageing simulations with the finite element method. Algorithm 2 details the quadrature point update procedure.

The total storage cost of the internal variables in this proposed method is:

Algorithm 2: Internal variable update

1   Given Δt, $\mathbf{F}^{n+1}$, $\hat{\bar{\boldsymbol{\tau}}}_{\beta}^{n}$, μ_a^n, μ_{ia}^n, N_a^n, N_{ia}^n and γ^n

2   **foreach** *Quadrature Point* **do**

3   Integrate to obtain μ_a^{n+1}, μ_{ia}^{n+1}, N_a^{n+1}, N_{ia}^{n+1} and γ^{n+1} from (4.39) to (4.42) and (4.64)

4   Evaluate creation rate $\dot{\mu}_c^{n+1}$ from (4.43)

5   Compute primary Kirchhoff stress $\bar{\tau}_\alpha^{n+1}$ from (4.116)

6   Compute and store secondary PK2 stress $\bar{\mathbf{S}}_\beta^{n+1}$ from (4.114)

7   Compute secondary Kirchhoff stress $\bar{\tau}_\beta^{n+1}$ from (4.115)

8   Evaluate Kirchhoff stress $\bar{\tau}^{n+1}$ from (4.117)

9   Use updated Kirchhoff stress $\bar{\tau}^{n+1}$ to evaluate material tangent $\mathbb{C}$ from (3.24)

10   **end**

- Five (5) scalar values μ_a, μ_{ia}, N_a, N_{ia} and γ

- One (1) second order symmetric tensor $\bar{\mathbf{S}}_\beta$

for a total of 11 double precision floating point values per element integration point. This cost does not scale with the number of integration points on the unit sphere. The computational effort is equally low, at each element integration point:

- Eleven (11) scalar multiplications, one (1) 3x3 matrix multiplication and one (1) 3x3 matrix addition

- One (1) inverse of a 3x3 matrix $\bar{\mathbf{F}}^{-1}$

- Two (2) 3x3 matrix multiplications and one (1) scalar multiplication.

Note that these operations occur on (compile time known) fixed sized matrices. This enables loop unrolling and vectorisation (SIMD) compiler optimisations. Furthermore, the internal variable update constitutes an embarrassingly parallel problem and the workload can be shared over multiple processors. These optimisations allow for a very computationally efficient algorithm for large scale simulation of the oxidative ageing effect in the finite element framework.

4.7   Non-Gaussian extension

If the primary network constitutes a large percentage of the elastomer response, a higher fidelity model can be used for the primary network. In this case, the primary deviatoric Kirchhoff stress can be taken as the affine non-Gaussian microsphere model

$$\bar{\boldsymbol{\tau}}_\alpha(t) = \gamma(t)\mu_a(0)\left\langle \frac{3N_a(0) - \lambda^2}{N_a(0) - \lambda^2}\boldsymbol{t} \otimes \boldsymbol{t} \right\rangle \tag{4.118}$$

where $\boldsymbol{t} = \bar{\mathbf{F}} \cdot \boldsymbol{r}$ and $\lambda = ||\boldsymbol{t}||_2$ with $\boldsymbol{r}$ representing the vector to the surface of the unit sphere. The material tangent can be written as

$$\bar{\mathbb{C}}_{f,\alpha} = \gamma(t)\mu_a(0)\left\langle \left[\frac{\lambda^4 + 3N_a(0)^2}{(N_a(0) - \lambda^2)^2}\lambda^{-2} - \frac{3N_a(0) - \lambda^2}{N_a(0) - \lambda^2}\lambda^{-2} \right] \boldsymbol{t} \otimes \boldsymbol{t} \otimes \boldsymbol{t} \otimes \boldsymbol{t} \right\rangle \tag{4.119}$$

and the deviatoric projection is consequently performed according to (3.24). Note that the initial number of segments per chain plays a role in the mechanical response of the material. The procedure for the non-affine non-Gaussian model is identical to [Miehe et al., 2004]. Note that higher order integration schemes for the discretisation of the homogenisation integral can be required depending on convergence criteria. Further information about integration schemes is available in Appendix C.3.

Chapter 5

Numerical examples

In this chapter, a collection of numerical examples will be presented and the results discussed. Firstly, a simple uniaxial test specimen will be analysed and the influence of the parameters on the stress softening and permanent set will be investigated under simplified loading. Secondly, two finite element examples of an automotive engine mount and an extruded seal example will be presented alongside computational performance metrics. These numerical examples will prove the industrial relevancy of the proposed model and the ability to perform large scale finite element simulations of ageing components.

5.1 Uniaxial test specimen

The uniaxial test specimen is a building block in experimental procedures for determining the mechanical properties of elastomer compounds. During this test, a sample is stretched to a fixed position, held and then returned to the original position. Over time, the stress at each time point is stored and stress softening of the material is able to be observed. The strain state in a uniaxial setting is governed by the deformation gradient under ideally incompressible conditions viz.,

$$\mathbf{F} = \begin{bmatrix} \lambda & 0 & 0 \\ 0 & \frac{1}{\sqrt{\lambda}} & 0 \\ 0 & 0 & \frac{1}{\sqrt{\lambda}} \end{bmatrix} . \tag{5.1}$$

For both the intermittent uniaxial and continuous relaxation numerical tests a displacement controlled loading condition is chosen for simplicity, see Figure 5.1a. The time period when moving between a stretch of $\lambda = 1$ and $\lambda = 1.5$ is chosen to be one hour. During this ramp time, some small amount of ageing occurs but this can be safely neglected.

The Cauchy stress response from the primary and secondary network is provided in Figure 5.1. The primary network is only permitted to decay over time and this can be clearly seen in Figure 5.1b. Another important property is the stress-free secondary network formation, which can be observed in Figure 5.1c. Here the formation of secondary networks during ageing does not contribute to the overall stress response until they are perturbed from their deformation state at creation. Separate analysis of the primary and secondary network is a useful, albeit fictitious, verification tool to ensure the model is performing as expected. The actual stress response is always the combination of the two networks. The complete response of the material is the superposition of the primary and secondary networks, see Figure 5.1d. Both the stress softening and permanent set effect can be seen in the combined response of the primary and secondary network.

The scission rate determines the amount of stress relaxation that occurs during ageing, with higher rates of scission leading to faster degradation of the primary network. It should be noted that the permanent

(a) Applied stretch loading

(b) Primary network response

(c) Secondary network response

(d) Combined network response
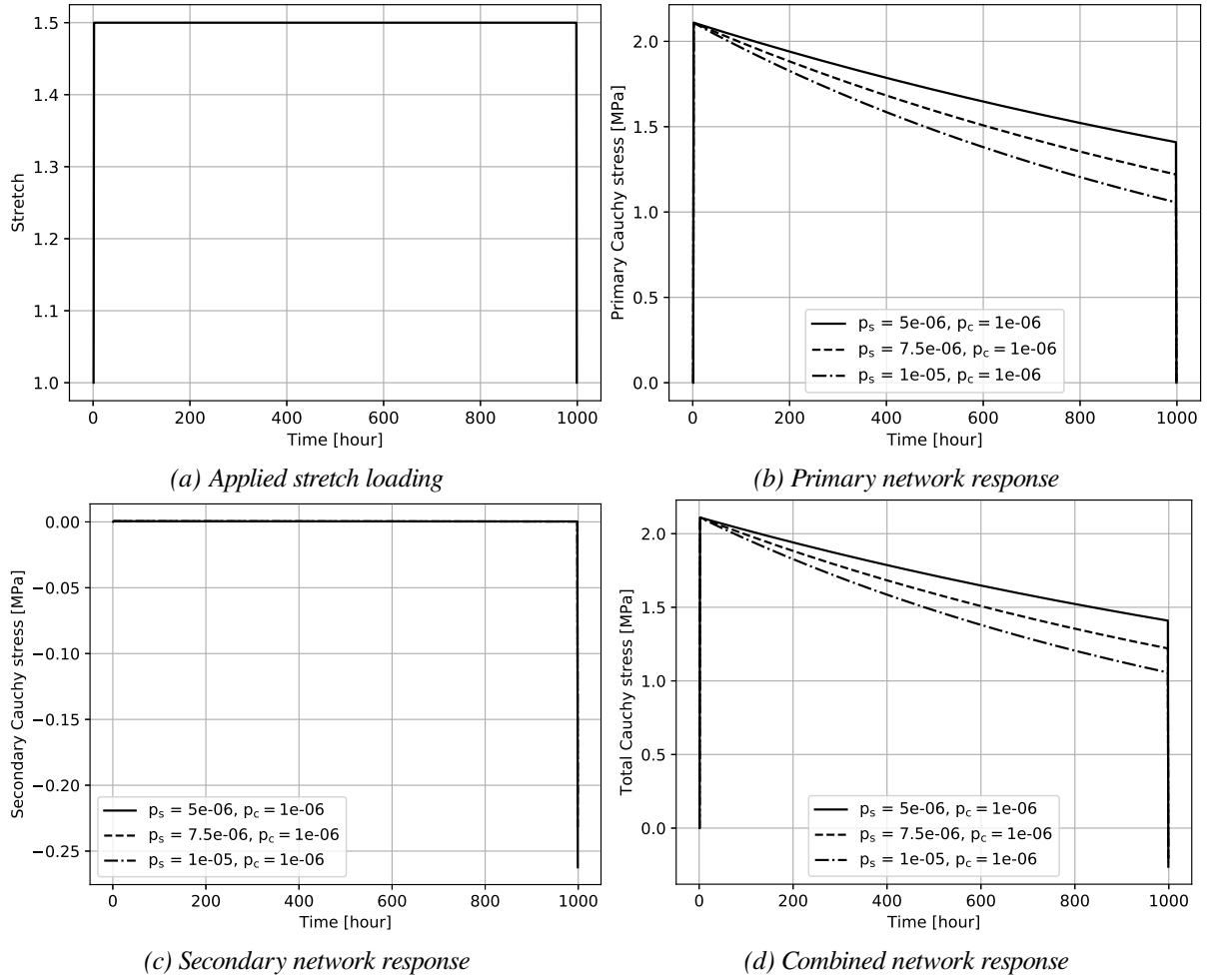
Figure 5.1: Continuous uniaxial test with initial conditions $\mu_a(0) = 1\,\text{MPa}$, $N_a(0) = 60$ and $N_{ia}(0) = 120$

set is observed through a negative stress when the specimen is returned to a stretch of one. The degree of permanent set is difficult to quantify from the continuous stress plots and is the topic of Section 5.1.1.

5.1.1 Permanent tension set

Resistance to permanent set is an important parameter to consider when selecting an elastomer for design. Therefore accurate prediction of permanent set is of interest to avoid a loss of component performance with potentially dire consequences. A permanent set experiment consists of ageing a specimen at a deformed state ($\lambda = 1.5$) for a period of time and then releasing the specimen and recording the final displacement. Permanent set is calculated as the percentage of the total deformation of the specimen according to

$$\text{Permanent set } (\%) = \frac{l_s - l_0}{l_f - l_0} \times 100\% \tag{5.2}$$

where l_s is the permanent deformed length of each specimen, l_0 is the initial length and l_f is the deformation that the specimen was set to.

Due to secondary network formation in a stress-free configuration, a new equilibrium position will be found in between the initial and stretched configurations. Performing the simulation and plotting the end

time and the permanent stretch remaining as a percentage of the total applied stretch was performed and presented in Figure 5.2.
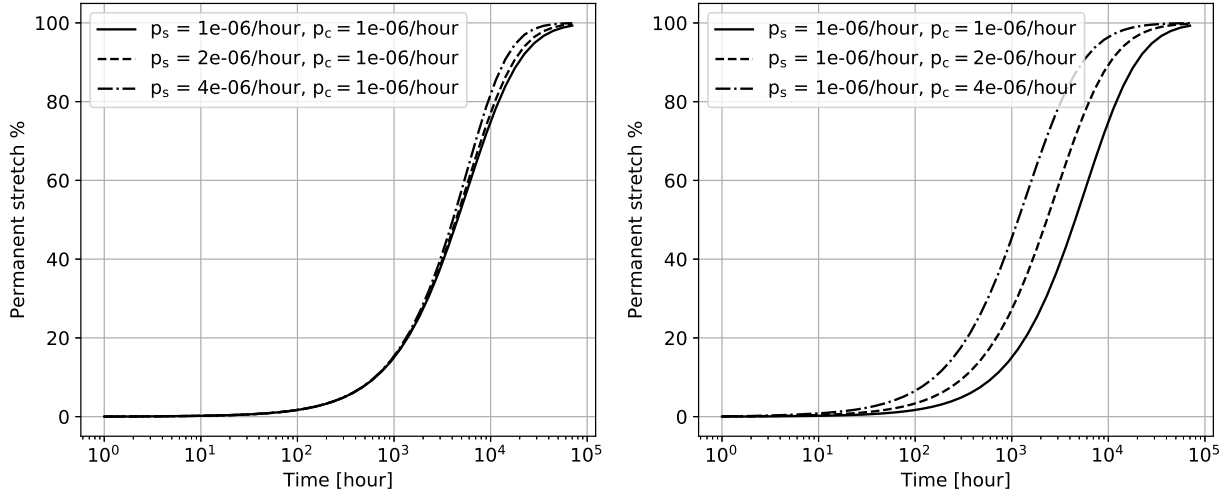
Figure 5.2: Permanent set for different rates of scission p_s and cross-linking p_c with $\mu_a(0) = 1\,\mathrm{MPa}$, $N_a(0) = 60$ and $N_{ia}(0) = 30$

It can be observed in Figure 5.2 that the permanent set is strongly dependent on the cross-linking rate. Changes in scission rate does not significantly effect the degree of permanent set as expected. Small differences in the permanent set as the scission rate increases are due to the additional chains in the inactive set, leading to accelerated cross-linking reactions due to the dependence in n_{ia}. This suggests that both a permanent set and a uniaxial stress test are required to determine p_s and p_c.

Permanent set appears to increase until it reaches a value of 100% after a significant period of time. The cross-linking probability effects the time required to reach a complete rearrangement of the polymer network such that the new deformation state is the new stress-free reference configuration. It is important to note that during ageing in a deformed state, the network is continuously undergoing rearrangement, with the gradual degradation of the initial network until no polymer chains exist with respect to $\lambda = 1$.

Since the permanent set is a central player in oxidative ageing, a comparison with the state of the art model developed by [Hossain et al., 2009a] will be conducted. Although this model was originally developed to model the curing of thermosets, several authors have applied this model to oxidative ageing. The Neo-Hooke version of the Hossain model is presented by [Dippel et al., 2014]. The Neo-Hooke version has been compared with the proposed model, see Figure 5.3. A multistep ramped stretch was chosen as the applied load in order to build secondary networks at multiple different deformation states, see Figure 5.3a. The primary and secondary network stresses are computed through the evaluation and push forward of (4.11) and (4.16) respectively. Inspection of Figure 5.3b reveals that both models predict a similar decay of the primary network.

Figure 5.3c demonstrates the key differences between the modelling approach for the secondary network response. Most importantly, both models demonstrate the stress-free curing property as observed for the first 10000 hours. The proposed model also demonstrates the degradation of the secondary network through scission, as indicated by the stress softening during periods of constant deformation. This results in an overall lower stress of the proposed model than the Dippel et.al model over extended ageing periods. The stress response upon returning to the original configuration differ significantly between the two models. To further understand these differences, a series of tests are performed, where the applied deformation has the same distribution of constant periods, but is scaled on the time axis, see Figure 5.4. A history of the permanent set

(a) Applied stretch loading

(b) Primary network response

(c) Secondary network response
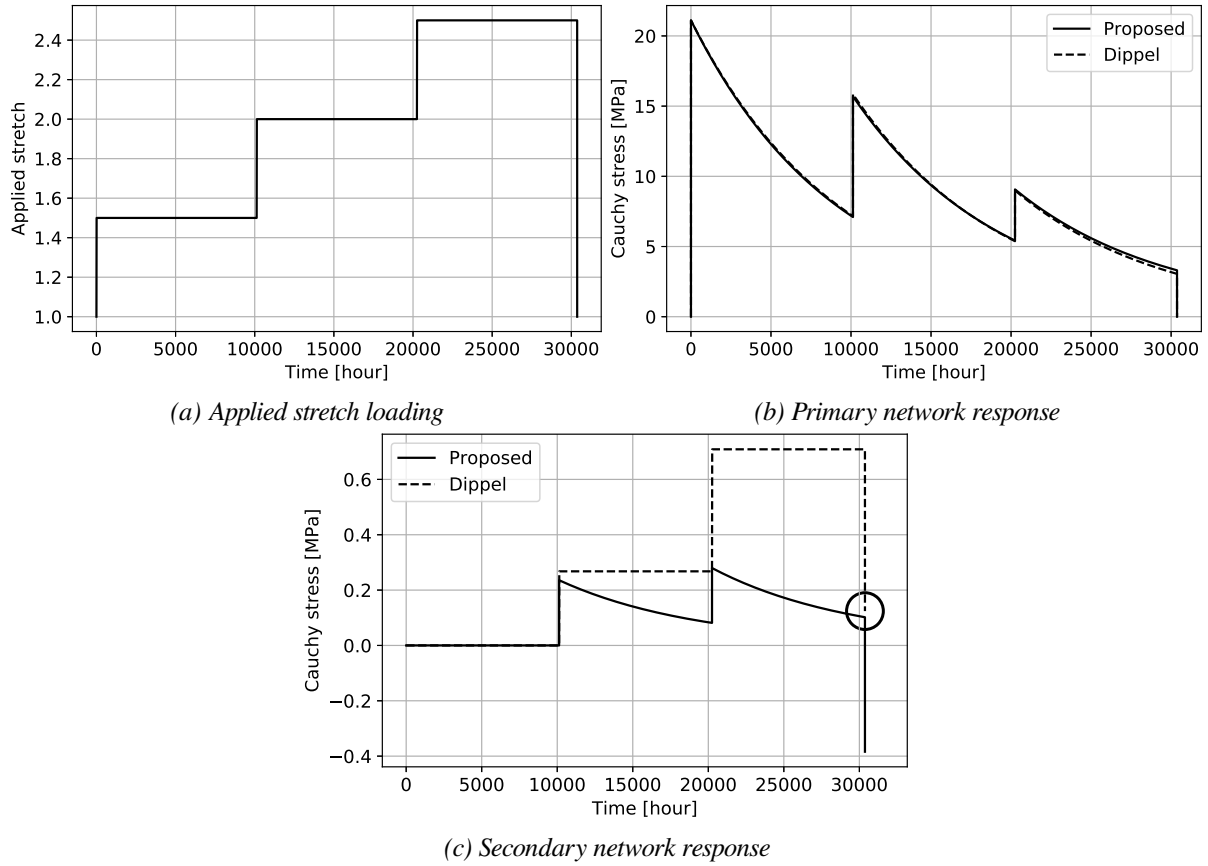
Figure 5.3: Comparison between primary and secondary network response for Hossain and the proposed model

as generated by only the secondary network is given in Figure 5.4. The actual permanent set of the specimen is the result of different states of ease in the primary and secondary network. However, for simplification, only the state of ease of the secondary networks are shown.

Major differences in the permanent set prediction of the secondary network between the two models is apparent from inspection of Figure 5.4. To further understand the response of the Dippel model it is important to note that the extension is performed at a slower rate than the compression, see Figure 5.3a. The differences in the strain rates have a deleterious effect when the loading changes direction. This is due to the sampling of the reduction factor q_r only when the strain rate is non-zero. This is clearly observable by inspection of (4.16). In contrast, the proposed model is continuously tracking the network dynamics and updating the material response throughout time.

The permanent set results from the Dippel model appear to be nonphysical. Despite the fact that the component remains above a stretch of 1.0, the model predicts a permanent set due to the secondary network of less than one, which corresponds to a compression. A reasonable estimation of the stretch should be between 1.5 and 2.5. In contrast, the proposed model shows a complex evolution of the permanent set but it shows that $\lambda \geq 1.5$. When the ageing time is sufficiently long, the networks created at earlier time points gradually undergo scission reactions and the memory of the earlier deformation is lost and the permanent stretch tends to the final constant stretch period. The analysis provided here is only performed on the fictitious secondary network, however the conclusions are unchanged when considering the combination of
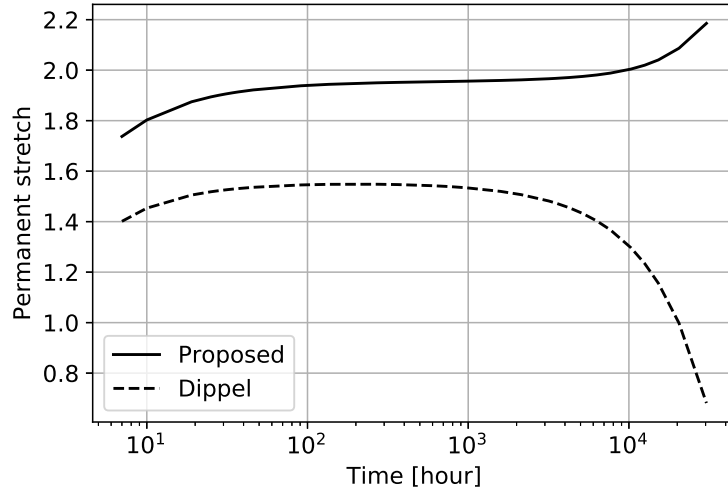
Figure 5.4: Permanent stretch at the new stress-free configuration after oxidative ageing

the networks as the primary network response is able to be matched for both models, see Figure 5.3b.

Experimental procedures do not typically consider ageing at multiple stages of deformation due to the additional experimental effect required. With an arbitrary deformation history, oxidative ageing models based on the Hossain model should be used with caution as the permanent set prediction can be, at best, under predicted and potentially nonphysical.

5.1.2 Intermittent tension test

The intermittent stress test illustrates the differences in stiffness of an elastomer over time and depend heavily on the chemical treatment and composition. An elastomer can increase or decrease in stiffness over time depending on which reactions are dominant at which point during the ageing. In this test, samples are left to age in their initial configuration until a specified time. The specimens are then elongated to a predetermined stretch and the stress is then recorded. For elastomers which become stiffer over time, the stress will increase. Conversely, the stress will decrease for elastomers which exhibit softening over time. The results for an intermittent uniaxial stress test are provided in Figure 5.5 for various values of p_s and p_c.

As observed in Figure 5.5a, the model is able to reproduce monotonic increases and decreases in stiffness over time. Note that the parameters p_s and p_c are not balanced in the sense that equal values will not result in a constant stiffness.

5.2 Finite element modelling

This section will detail the finite element implementation and provide performance indicators. Implementation into a non-linear finite element framework can be performed in an efficient manner. The material routine needs to include the stress update procedure according to Algorithm 2. Reuse of the material tangent operator function for the affine Gaussian or non-affine non-Gaussian models is possible for the primary network model, if the hybrid approach is taken. A time integration scheme for the network dynamics equation is required and can be performed by including the reduction equation in the linearisation provided in Appendix D. Note that an adhoc method of assuming $\dot{N}$ is zero and iterating until convergence of the rates appears to function, however no guarantees can be made about the stability or accuracy for arbitrary initial conditions or parameters.

| (a) Various p_s | (b) Various p_c |
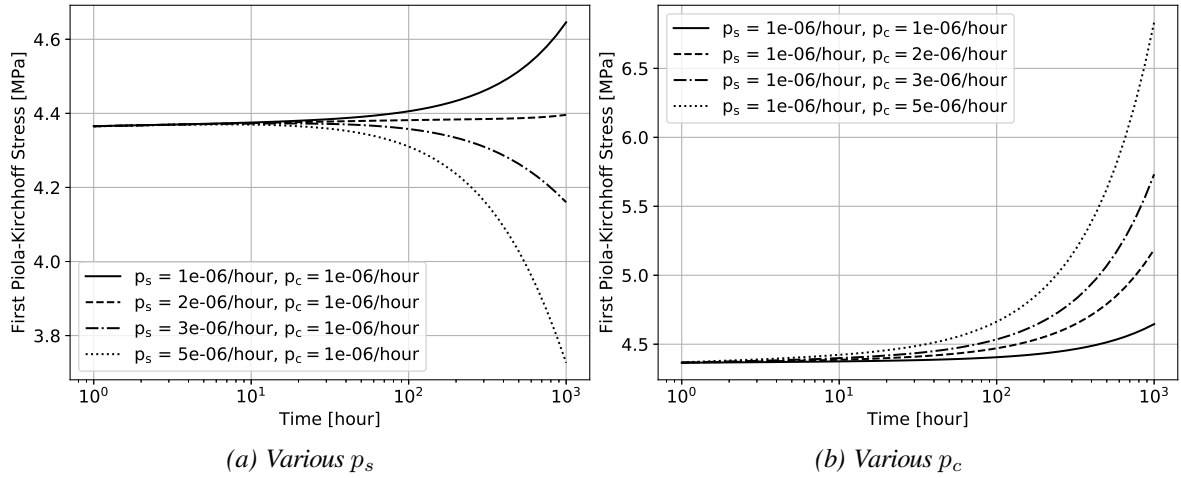
Figure 5.5: Intermittent stress values at 50% elongation

A hallmark of consistent linearisation is the convergence of the Newton-Raphson method. In the neighbourhood of the solution, the convergence should be quadratic. In the proposed model, changes in the stiffness caused by the network dynamics means that periods of fast dynamics will cause the solution to be sufficiently far away from the previous solution, resulting in poorer convergence behaviour. In Figure 5.6 a plot of the convergence properties after a few time steps of the model is presented for the incremental displacement and residual force norm. Note that rapid convergence can be observed within five iterations.
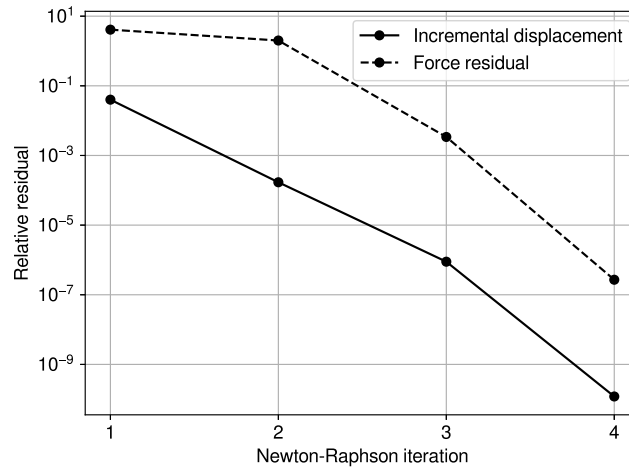
Figure 5.6: Newton-Raphson convergence properties of proposed model

From Figure 5.7 it can be observed that the internal variable update, including the computation of the material tangent operator and the stress update procedure, consumes a very small portion of the overall wall clock time in a single Newton-Raphson iteration. This benchmark was performed on an AMD Ryzen 2700 8C/16T machine with 16GB of RAM using an open source finite element solver written in modern C++ compiled with native optimisations enabled. Note that both the stiffness assembly and the internal variable update is multithreaded and the linear algebra library `Eigen` was used to obtain highly optimised linear algebra routines. As previously eluded to, the ageing model is very efficient and the time is dominated by

the linear solver, IO and sparse matrix assembly procedures.
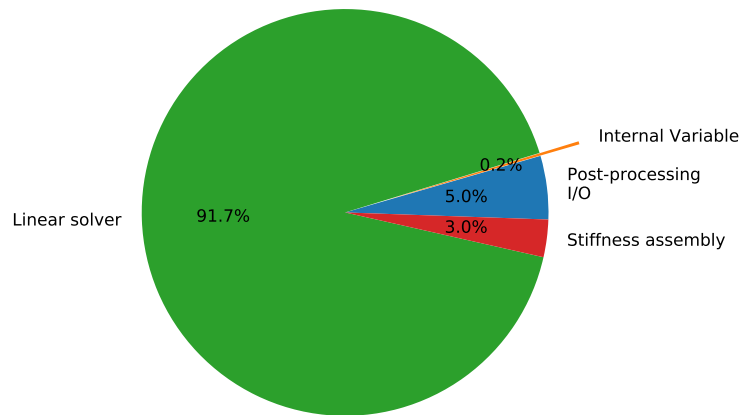
Figure 5.7: Performance properties of proposed model for one Newton-Raphson iteration for a 650k DoF model

Note that the domination of the linear solver is expected for such large problems due to the algorithmic complexity for the direct linear solver of $\mathcal{O}(N^3)$, where N is the size of the sparse matrix. Nevertheless, assembly and internal variable updates scale with the number of elements and quadrature points and is less of a concern than the linear solution stage, especially since multithreading scales reasonably well in comparison to the linear solver.

5.3 Automotive engine mount

Elastomers are commonly used as a mounting structure to isolate vibrations and provide a small degree of flexibility. Naturally, these properties degrade over time and the mount will need to be replaced before excessive vibrations cause damage to the plant or neighbouring structures. Consider the engine mounts in automobiles. Here, the mount is subjected to a constant load owing to the weight of the structure (ignoring operating transients and loads). When stress softening is combined with a constant load, the mounts sag over time and causes the motor to lower and potentially increases the stress on connected components. Quantification of this sag is of interest to the engineer for determining safe operating limits.

Consider the basic engine mount geometry with boundary conditions as shown in Figure 5.8. The outer ring is typically encased in either a plastic or steel housing and mounts to the chassis. For this example, the outer ring has an outer diameter of $80\,\mathrm{mm}$. The inner ring is attached to a steel sleeve and then bolted to the motor. The outer ring is rigidly fixed.

A total of 288456 quadratic tetrahedron elements were used, resulting in a total of 646584 unknowns. For the loading, a symmetric boundary condition was placed in the y direction. A uniform and constant traction load of $0.1\,\mathrm{MPa}$ was placed on the upper surface of the inner ring to approximate a bearing load. The simulation was run for a total of 2000 days with a maximum time step of 50 days. The material properties for the simulation are provided in Table 5.1.

Computing the inactive shear modulus (or the inactive cross-link density) is performed by experimentally determining the percentage cure as a function of the curing time. Let χ be the fraction of fully cured for the elastomer. The inactive cross-link density is not known and, by extension, the inactive shear modulus.
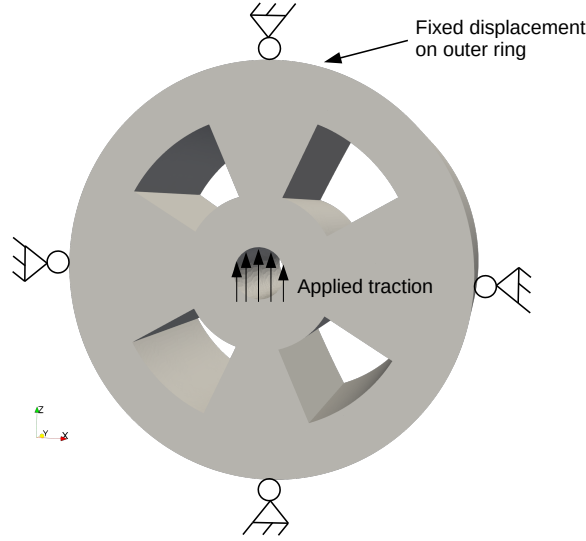
Figure 5.8: Engine mount with applied boundary conditions

Table 5.1: Material parameters for mount

Parameter	Symbol	Value	Unit
Shear modulus	$\mu_a(0)$	0.67	MPa
Bulk modulus	K	16.67	MPa
Inactive shear modulus	$\mu_{ia}(0)$	0.035 (T95)	MPa
Scission rate	p_s	$2.0 \cdot 10^{-5}$	s^{-1}
Cross-linking rate	p_c	$1.0 \cdot 10^{-5}$	s^{-1}
Segments per chain, active	$N_a(0)$	70	-
Segments per chain, inactive	$N_{ia}(0)$	0	-

Assume that the initial active shear modulus μ_a is known, then the inactive shear modulus is given by

$$\mu_{ia}(0) = \frac{1-\chi}{\chi}\mu_a(0) \ . \tag{5.3}$$

The displacement evolution over the ageing period is provided at several snapshots in Figure 5.9. Due to the stress softening, the displacement field evolves over time as the stiffness decreases for the parameters listed in Table 5.1. The displacement reached a peak of $4\,\text{mm}$ during the ageing period and upon release of the load, the permanent displacement is approximately $3\,\text{mm}$. A higher cross-linking rate could cause the component to become stiffer and resist sag with a likely increase in permanent compression set. The design engineer can use the results of this simulation to compute the sag over time due to ageing and analyse more complicated loading histories.

Figure 5.10 shows that the Cauchy stress does not evolve significantly due to scission over time, except when softening causes the load path to change inside the component. At the conclusion of the simulation, the component returns to a stress-free position at a different position, as indicated in Figure 5.9.

At this point, it is clear that this model is powerful predictive tool in the analysis of complex components that undergo significant stress softening. The component designer is able to predict if stress-softening will cause a previously low stress region to accept additional load and potentially cause previously unpredictable

(a) Day 1   *(b) Day 16*

(c) Day 228   *(d) Day 828*

(e) Day 1528   *(f) Permanent set after release at 2001 days*
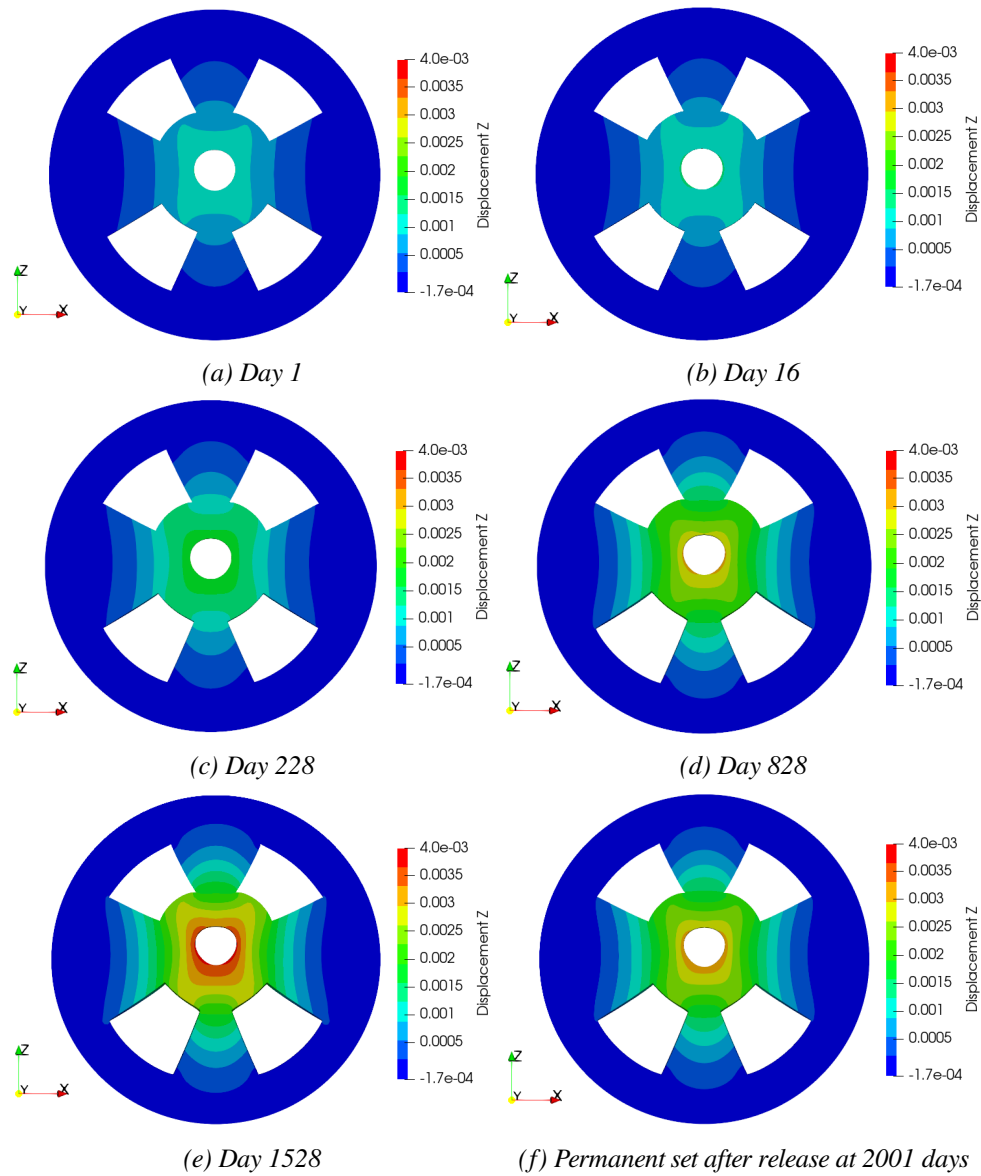
Figure 5.9: Displacement evolution of ageing elastomer mount under constant traction load

effects due to oxidative ageing. Geometry optimisation is often used to design such engine mounts and modelling capabilities can now incorporate long-term oxidative ageing effects. This opens the door for increasing component lifetime for sustainable product design through better durability and less raw materials.

This engine mount example is an excellent example of the need to introduce the DLO effect. Due to the large amount of internal material compared to surface material, the internal material will age at a significantly different rate. The resulting heterogeneous structure could significantly influence the degree of permanent set and stress-softening. A topic of future work is the coupling of oxygen reaction-diffusion into the network dynamics model.

(a) Day 1

(b) Day 828

(c) Day 2000

(d) Day 2001
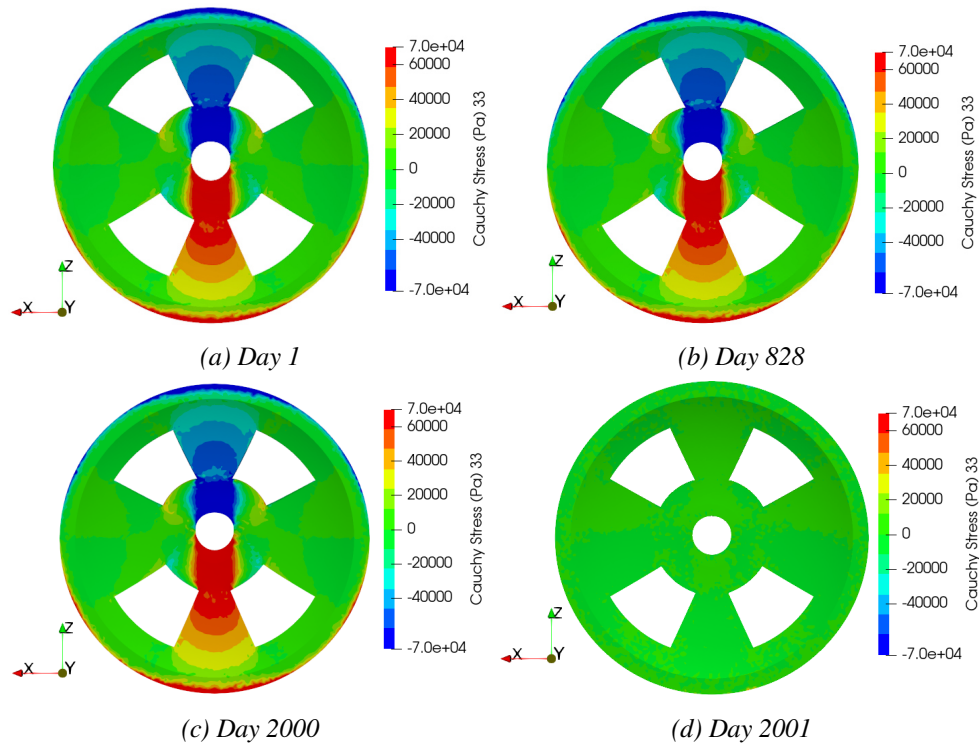
Figure 5.10: Cauchy stress evolution of ageing elastomer mount under constant traction load

5.4 Flexible boot

Another important application for elastomer components is the protection of mechanical joints from environmental conditions such as dust, water and light. When these boots age and become brittle, they often crack allowing contaminant ingress and rapid wear to take place. When this occurs, for example in a constant velocity (CV) joint of an automobile, the mechanical joint will wear rapidly and lead to expensive repairs.

In this example, a rubber boot is stretched in the y direction to a displacement of $10\,\mathrm{mm}$. Symmetric boundary conditions are applied on the quarter model and the bottom flange displacement are fixed to zero in all directions. Displacement boundary conditions model the use of this boot in a scenario where the boot is constantly held at a defined position, as is the case with CV joints on vehicles, see Figure 5.11. A total of 556054 quadratic tetrahedron elements were used, resulting in a total of 1387386 unknowns. The material properties are summarised in Table 5.2. Due to the relatively thin-walled structure, the DLO effect will play a lesser role than in the engine mount example.

The displacement field can be seen in Figure 5.12. After 1000 days of ageing, substantial permanent tension set has been developed and the stress is significantly reduced over the ageing time, see Figures 5.12 and 5.13 respectively. The maximum observed permanent tension set according to (5.2) is 93% at the load point to a final deformation of $9.3\,\mathrm{mm}$ from a fixed displacement of $10\,\mathrm{mm}$.

The stress developed during the loading tends to decay towards a stress-free state over time, indicating stress-free curing is occurring in the deformed configuration. Both regions of tension and compression are smoothed over several years with the choice of material parameters. In the manner as the engine mount, a virtual model can aid the designer in selection of a suitable elastomer type by providing a virtual method for predicting stiffness changes and permanent set under various loading conditions.

(a) Isometric view

(b) Applied displacement boundary conditions
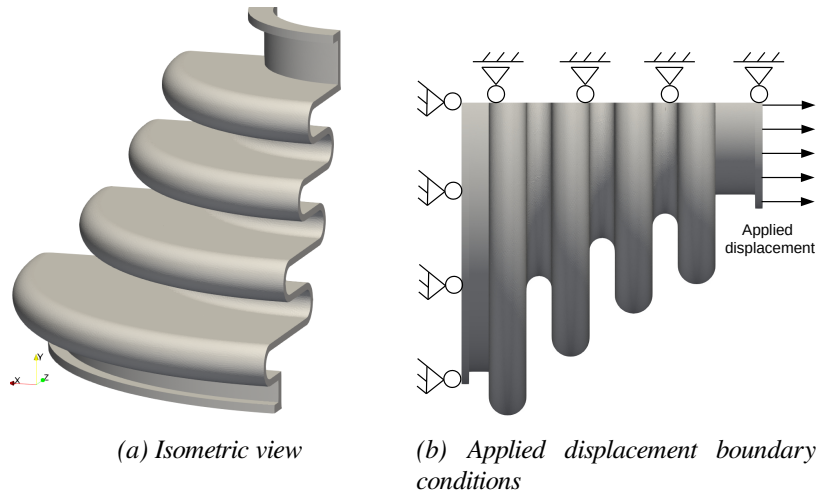
Figure 5.11: A quarter model of a rubber bellow-style boot with applied boundary conditions

Table 5.2: Material parameters for boot

Parameter	Symbol	Value	Unit
Shear modulus	$\mu_a(0)$	0.33	MPa
Bulk modulus	K	8.3	MPa
Inactive shear modulus	$\mu_{ia}(0)$	0.017 (T95)	MPa
Scission rate	p_s	$3.5 \cdot 10^{-5}$	d^{-1}
Cross-linking rate	p_c	$1.5 \cdot 10^{-5}$	d^{-1}
Segments per chain, active	$N_a(0)$	70	-
Segments per chain, inactive	$N_{ia}(0)$	0	-

(a) 1 day

(b) Permanent set after release at 1001 days
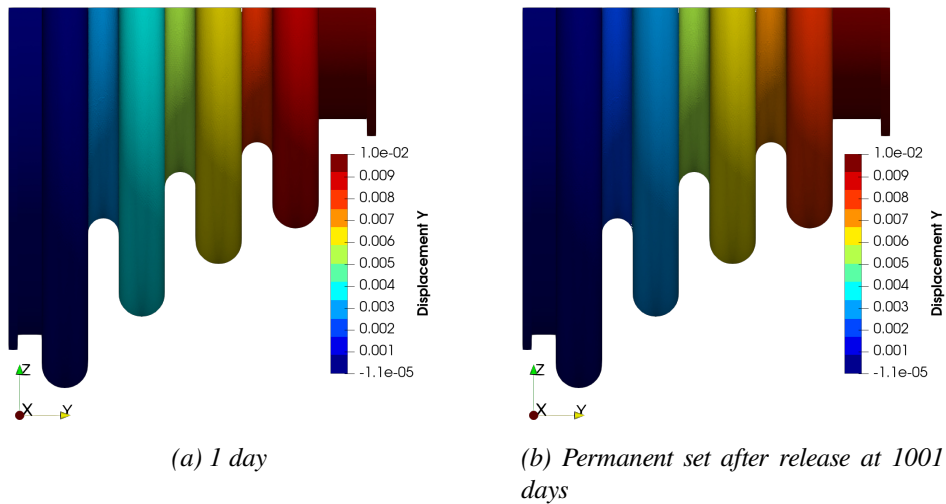
Figure 5.12: Displacement evolution of ageing elastomer boot. Note significant permanent set occurs after being held in stretched position for 1000 days

(a) Day 1

(b) Day 264

(c) Day 514

(d) Day 764
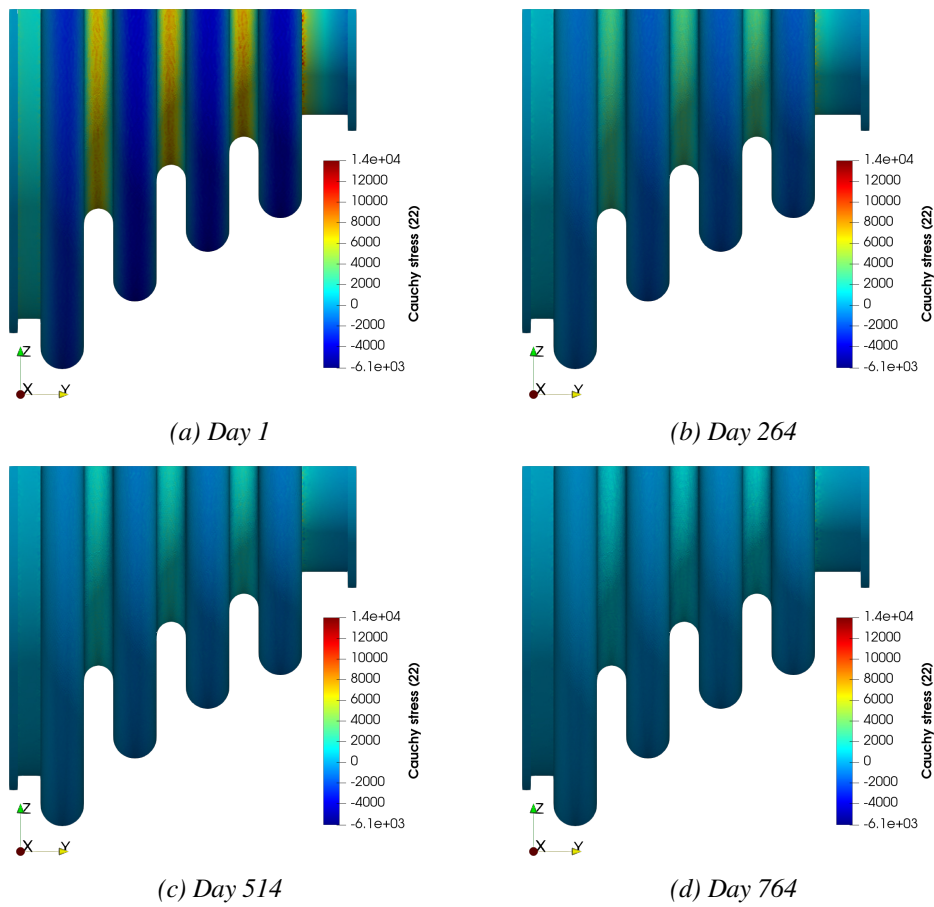
Figure 5.13: Cauchy stress (22) in Pa. Note stress softening effect in the constant loading condition

Chapter 6

Experimental results

In order to validate the proposed constitutive model, a series of permanent set and intermittent uniaxial tests were performed at the Deutsches Institut für Kautschuktechnologie (DIK) in Hanover, Germany. To match the model as closely as possible, the elastomer did not contain any additives such as filler and anti-ageing agents. Without these additives, this is considered academic exercise as the resulting elastomer would exhibit poor mechanical and ageing performance in comparison to technical elastomers. All experiments were performed for strains less than 200% in order to avoid deformation-dependent oxygen diffusion behaviour [Johlitz et al., 2014].

SBR was selected due to availability and the ability to undergo sufficient deformation after ageing. A total of six formulations, with peroxide and sulphur cross-linking systems, underwent trial ageing and the chosen recipe, based on sulphur cross-linking, is provided in Table 6.1.

Table 6.1: Unfilled SBR recipe

Constituent	Amount (phr)	Density (g/cm^3)
Buna SE 1500	100	0.94
Zinc Oxide	3	5.61
Stearic Acid	1	0.94
Rhenogran S-80	0.8	1.64
Rhenogran CBS-80	1.6	1.19
Total	106.4	-

After mixing, vulcanisation was performed in $1\,\mathrm{mm}$ sheets for $45\,\mathrm{min}$ at $170\,°\mathrm{C}$ to achieve T95, see Figure 6.1.

Thin vulcanised rubber sheets were chosen to reduce the diffusion limited oxidation (DLO) effect to ensure oxygen saturation. A total of two hundred S2 specimens were stamped and placed into the freezer at $-18\,°\mathrm{C}$ to inhibit further ageing.

6.1 Permanent set

Measuring the permanent set is a common procedure to assess the deformation dependent ageing performance of elastomers. The elastomer samples were fixed at 50% deformation and placed into an oven for a predetermined period of time, removed and then measured. However, this experiment does not uncover
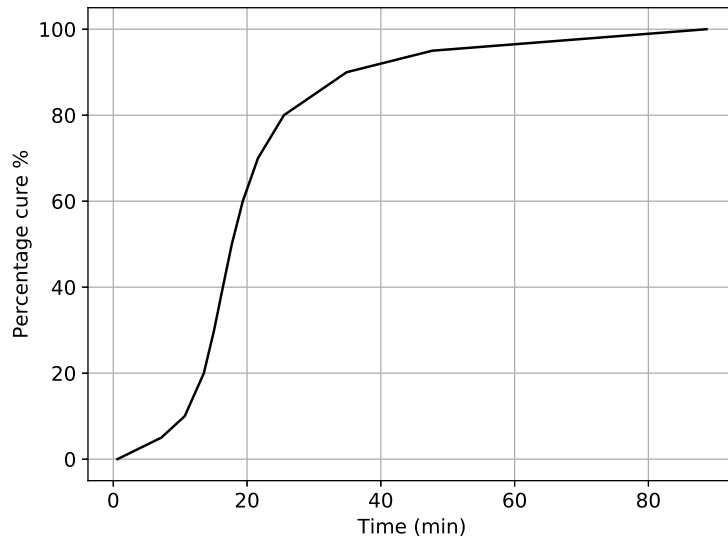
Figure 6.1: Cure percentage at 170 °C as time increases for the SBR recipe provided in Table 6.1

shortcomings in constitutive models for oxidative ageing, as seen in Section 5.1.1. While in the stretched configuration, the polymer network could build secondary networks in new stress-free states.

A total of five specimens across six time points were tested at three different temperatures, leading to a total of 90 specimens. These specimens were placed into the oven at intervals determined by a geometric sequence due to the rapidly accelerating ageing at shorter time intervals. The deformation was measured between the markers placed on the specimen before being placed into the oven. Each final deformation measurement was recorded in millimetres with Vernier calipers to four significant figures and given in Figure 6.2. The permanent set is computed according to (5.2).
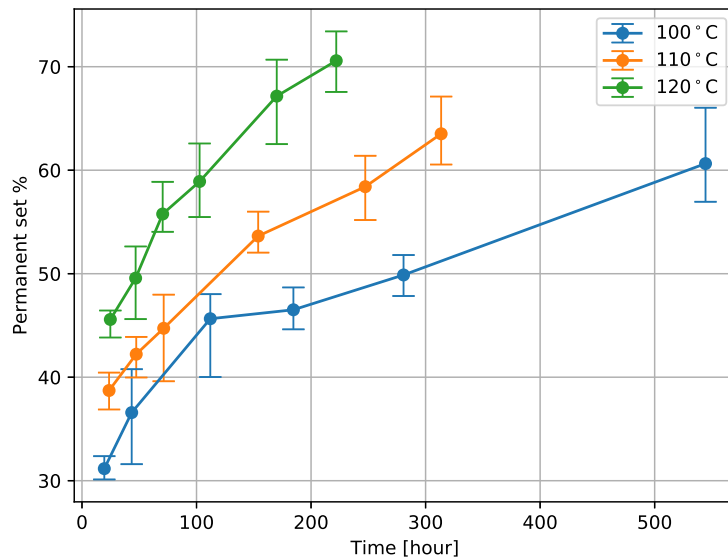
Figure 6.2: Averaged permanent set results for different temperatures with error bars indicating minimum and maximum recorded values

Inspection of Figure 6.2 indicates a clear dependence of the permanent set on both the temperature and

the ageing time as expected. Elevated temperatures can accelerate the permanent set by a factor of five and appears to have a non-linear dependence on the temperature, indicating a relationship with the well-known Arrhenius law. However, even at lower ageing times of approximately 20 hours the results indicate permanent set in the range of 30 to 45 percent. Fitting the numerical model to the experimental data results in Figure 6.3.
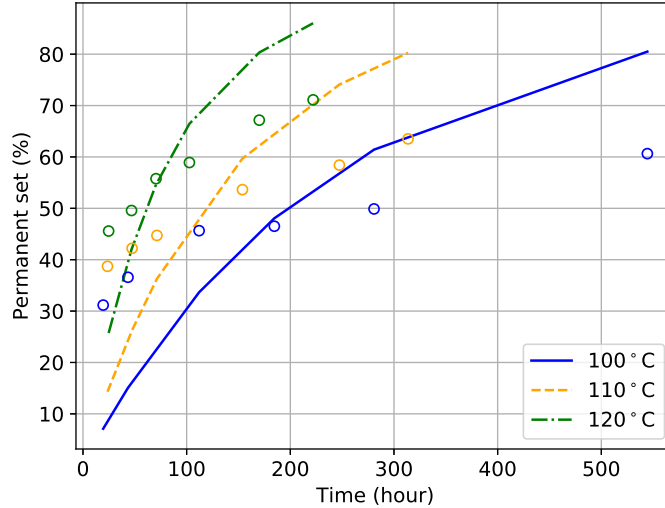
Figure 6.3: Numerical fit (line) to experimental measurements at different temperatures (circles)

The agreement between the numerical and experimental data in Figure 6.3 can be classified as poor. Qualitative inspection indicates that the experimentally determined permanent set is much higher than the numerically computed value at the beginning of the experiment. The model then over predicts the permanent set for longer time periods. A least squares fit attempts to match the high initial permanent set, but the network dynamics model is inadequate to capture such high initial permanent sets while not over-estimating the permanent set at longer time periods.

Additional sulphur cross-linking could attribute to the initially high permanent set. Sulphur cross-linking is known to quickly react and form new cross-links until the cross-linking bridges become shorter and reach an equilibrium. Oxidative ageing occurs simultaneously to create additional polymer cross-links, at a much slower rate. This effect will be seen in Section 6.2, which appears to support the sulphur bridge hypothesis.

A list of the resulting model parameters from the fit in Figure 6.3 are given in Table 6.2.

Table 6.2: Model fit parameters to permanent set data

Temperature °C	μ_a [MPa]	μ_a [MPa]	p_s [h^{-1}]	p_c [h^{-1}]
100	2.92	18.36	1.87e-06	7.18e-05
110	1.75	25.90	5.22e-06	8.97e-05
120	8.47	47.31	1.83e-06	9.35e-05

The least squares procedure did not produce the same cross-link density, however this discrepancy can be remedied by enforcing the same cross-link density. The resulting fit is still poor and will require a more advanced network dynamics model to capture the initially high rate with the slow taper off as oxidative ageing dominates. The correlations between the variables are given in Figure 6.4. High correlation is present between the cross-linking rate p_c and the active number of segments N_a. This is likely due to the

lack of intermittent test data to provide additional constraints during the parameter identification procedure. Use of the non-affine non-Gaussian model formulation (that includes the parameter $N_a(0)$) for the primary network would aid in determining $N_a(0)$. However, without good agreement between the current network dynamics model and the SBR experimental results, $N_a(0)$ is not able to be uniquely determined.
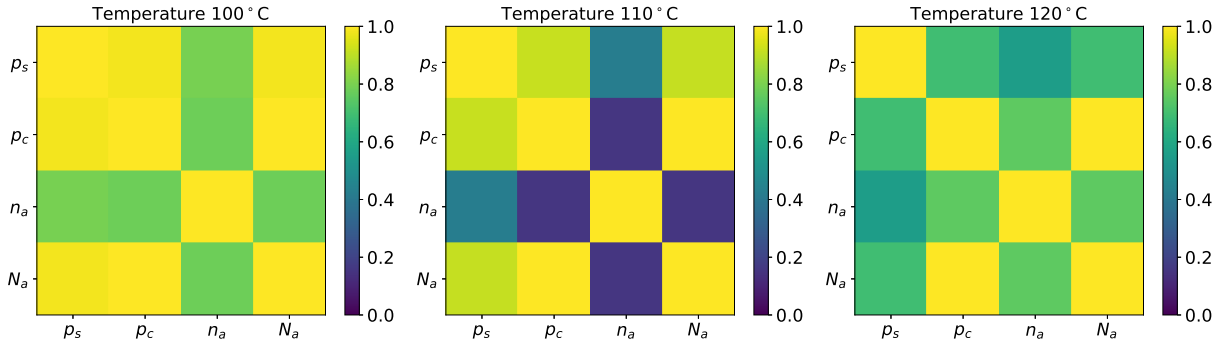
Figure 6.4: Correlation of model parameters from least-squares fitting procedure for permanent set

6.2 Intermittent uniaxial test

A common procedure to assess the softening or stiffening effect of elastomers is the intermittent uniaxial test. In this test, a series of samples are left to hang in an oven at an elevated temperature to undergo oxidative ageing. At specified time intervals, the samples are removed from the oven and are elongated to breaking strain in a uniaxial stress test. The stress at 50% elongation is recorded. In materials that exhibit stress-stiffening, the stress will increase over time. In contrast, stress-softening will result in a reduction in stress at 50% elongation. Whether an elastomer will exhibit softening or stiffening behaviour depends strongly on the dominant reaction kinetics at a given time [Tobolsky et al., 1944].
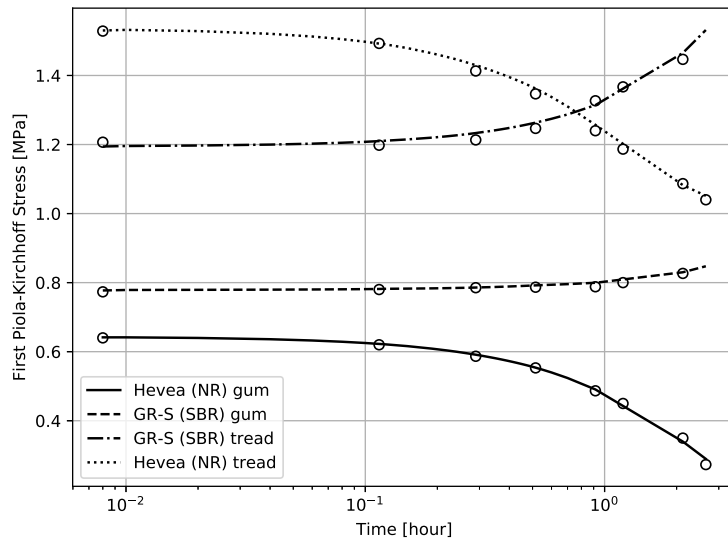
Figure 6.5: Intermittent stress comparison of experimental (points) and numerical results [Tobolsky et al., 1944]

Inspection of Figure 6.5 demonstrate excellent agreement between numerical and experimental results.

69

Note that Hevea is now commonly known as natural rubber and GR-S is now known as SBR and are simply historical artefacts [Augustyn et al., 2019]. A simple network dynamics model is able to capture the increases or decreases in stiffness over time, with the reflection of the material response in the rates of scission and cross-linking, see Table 6.3. This is a promising result for the effectiveness of the network dynamics model to describe micro-mechanical changes in polymer networks.

Model parameters were computed using the Python SciPy `optimize` package and the `least_squares` function with the default tolerances. The residual is computed as the difference between the experimental and numerical first Piola-Kirchhoff stresses. For the numerical model, the affine non-Gaussian model is used for the primary network and the affine Gaussian model is used for the secondary networks. Inclusion of the number of segments in the mechanical model assists in the fitting of the network dynamics initial value for N_a. The initial value of N_{ia} is taken as twice the initial value of N_a.

Table 6.3: Intermittent stress model parameters

Formulation	n_a	N_a	p_s	p_c
Hevea (NR) gum	0.58	26.61	0.013	0
GRS (SBR) gum	0.73	99.9	0.0024	0.0012
GRS (SBR) tread	1.11	67.8	0.00053	0.001
Hevea (NR) tread	0.8	3.43	0.084	0.031
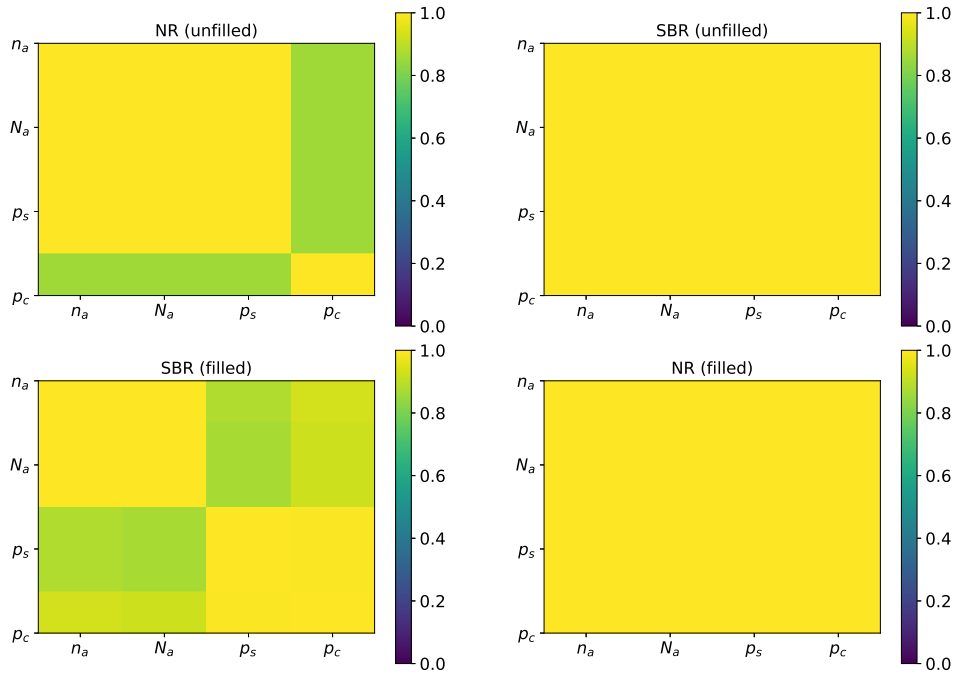
Figure 6.6: Correlation of model parameters from least-squares fitting procedure for Figure 6.5

To understand the influence that each parameter in Table 6.3 has on the overall solution, the correlation matrices for each elastomer type is given in Figure 6.6. Due to the non-linearities involved in the network dynamics the parameters are not necessarily unique. It is currently an open question as to whether a unique set of materials parameters is possible with the proposed model. The high correlation between p_s and p_c for the intermittent stress procedure suggest that these parameters can be combined into a single equivalent

parameter, as indicated by the similar decay pattern observed in Figure 4.11. The lack of uniqueness, indicated by the high correlation between parameters, can be attributed to the lack of fitting without permanent set data.

A series of intermittent uniaxial tests were performed at the DIK to investigate the ageing behaviour of unfilled elastomers with a sulphur cross-linking mechanism. The tests were carried out on a Zwick 1445 machine with a Zwick Roell Xforce HP loadcell with a sensitivity of $2\,\mathrm{mV\,V^{-1}}$. To limit viscoelastic effects, a strain rate of 60% per minute was used.

The stress results from the intermittent uniaxial tension test are provided in Figure 6.7. The mean of the data is plotted as the solid points and the error bars indicate the maximum and minimum values from an original sample set of five, with the minimum and maximum values removed. Several plots are provided with the stress at increasing levels of specimen elongation. Despite the significant variation in the data, clear trends are able to be recognised as temperature and ageing periods increase.

(a) First Piola-Kirchhoff stress at 50% strain

(b) First Piola-Kirchhoff stress at 100% strain

(c) First Piola-Kirchhoff stress at 150% strain

(d) First Piola-Kirchhoff stress at 200% strain
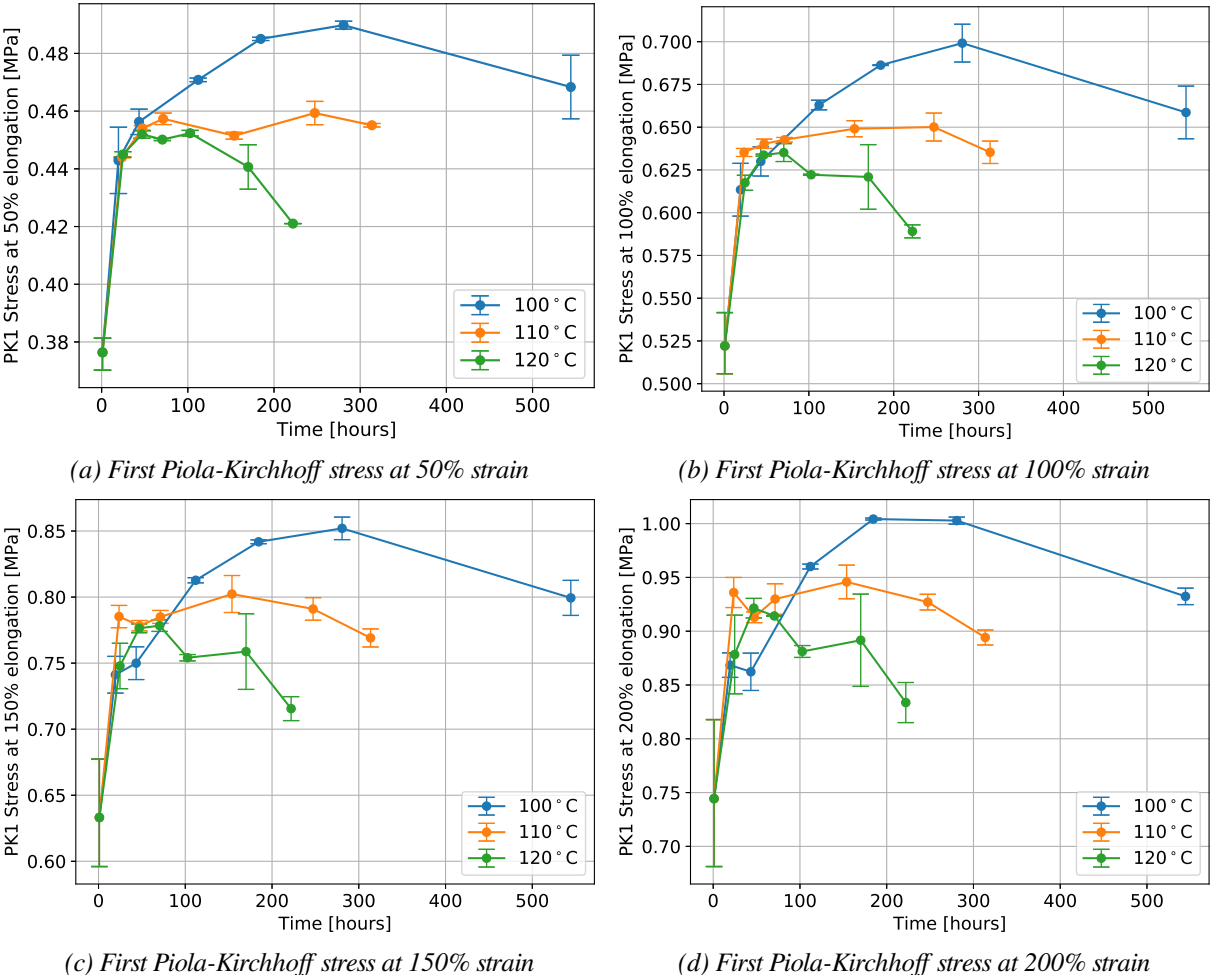
Figure 6.7: Intermittent stress test results for various strains and temperatures with removal of outliers. Error bars indicate maximum and minimum values over linear time scale.

The same data from Figure 6.7 is plotted with a logarithmic time axis in Figure 6.8. Inspection of earlier time periods appear to confirm the observations in Section 6.1, whereby the sulphur bridges are likely deconstructed and reconstructed to form a network with additional sulphur cross-links, thereby becoming

71

(a) First Piola-Kirchhoff stress at 50% strain

(b) First Piola-Kirchhoff stress at 100% strain

(c) First Piola-Kirchhoff stress at 150% strain

(d) First Piola-Kirchhoff stress at 200% strain
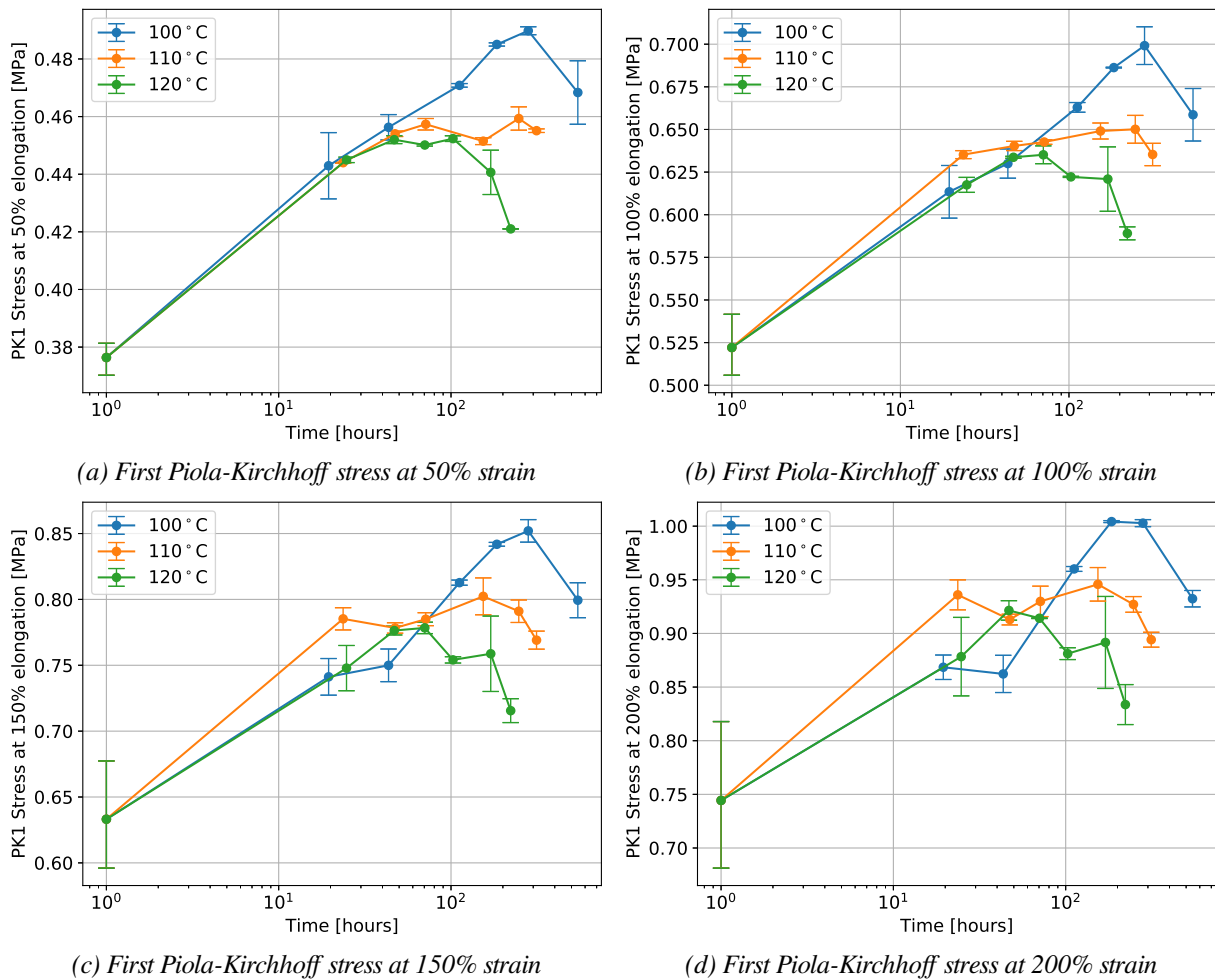
Figure 6.8: Intermittent stress test results for various strains and temperatures with removal of outliers. Error bars indicate maximum and minimum values over log time scale.

stiffer. Once the sulphur bridges reach a limiting value, the oxidative ageing effects then dominate, with a balance of polymer cross-linking and chain scission which eventually leads to softening of the polymer matrix. Attempting to apply the basic network dynamics model to this data results in a poor fit. The proposed network dynamics model can only capture monotonic increases or decreases in stiffness due to the basic kinetics. A proper fit requires an extension to include a dual-network approach for distinguishing between sulphur and oxidative ageing. A proposal for the extension of the network dynamics with these assumptions is covered in Section 6.3.

6.3 Extended network dynamics

The mechanisms responsible for the initial stiffness increase observed experimentally is likely due to the fast degradation of the sulphur cross-links. An extension to the network dynamics is proposed in this section in order to capture the differences in the chemical reactions of the basic network dynamics. The possible mechanisms for sulphur ageing are provided in Figure 6.9 with the mechanisms behind the numbers provided in [Nocil, 2010].
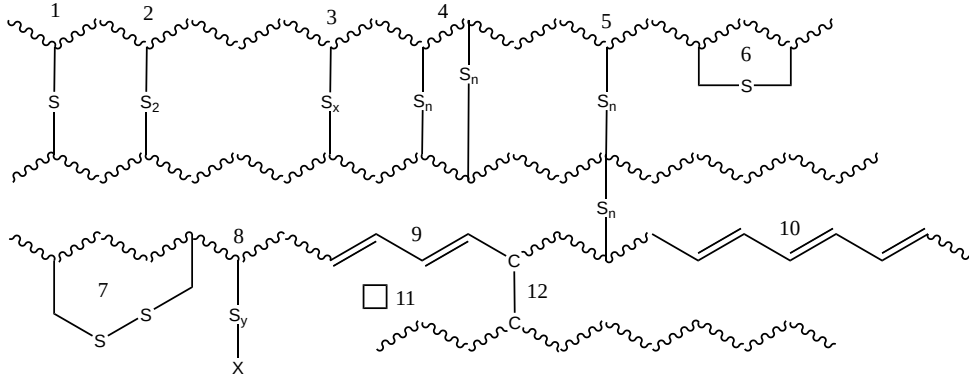
Figure 6.9: Possible configurations for sulphur cross-linking

Of particular relevance for the proposed modifications to the model are the following numbers from Figure 6.9:

1. Single sulphur cross-link

2. Double sulphur cross-link

3. Multiple sulphur cross-links

5. Sulphur cross-linking occurring to another cross-linked carbon

6. Sulphur loop spanning single carbon-carbon bond

7. Sulphur loop spanning multiple carbon-carbon bonds

Consider the initial state of the polymer after vulcanisation has taken place. The polymer is sparsely cross-linked with sulphur bridges that must be at least one unit in length. Let $N_{a,s} = \{x \in \mathbb{R} \mid x \geq 1\}$ be the average number of segments in the sulphur bridges. For simplicity only the sulphur cross-links are modelled, specifically items 1, 2 and 3. Following the previous derivation, we introduce the failure density function ζ as

$$\zeta = p_c \left(N_{a,s} + \dot{N}_{a,s} t \right) \exp \left(-p_c N_{a,s} t \right) . \tag{6.1}$$

Since $N_{a,s} << N_a$, the probability that an arbitrary sulphur cross-link undergoes a scission reaction is much higher than a single chain. Assuming that each scission leads to a cross-linking reaction, then the rate at which the sulphur network changes is

$$\frac{\mathrm{d}n_{a,s}}{\mathrm{d}t} = \zeta n_{a,s} . \tag{6.2}$$

Mass conversation dictates the evolution of the sulphur cross-linking segments to be

$$\frac{\mathrm{d}N_{a,s}}{\mathrm{d}t} = -\frac{N_{a,s}}{n_{a,s}} \frac{\mathrm{d}n_{a,s}}{\mathrm{d}t} \tag{6.3}$$

$$= -\zeta N_{a,s} . \tag{6.4}$$

73

Note that sulphur can form an inactive ring attached to the polymer, rather than contributing to further cross-linking, see item 6 and 7 in Figure 6.9. This effect is neglected in the outline of an extended model and would require an additional set to handle inactive sulphur bonds.

The total response of the elastomer is governed then by the sum of the sulphur cross-links and those built later by oxidative ageing as

$$n_a = n_{a,s} + n_{a,o} \, , \tag{6.5}$$

where $n_{a,o}$ is the cross-link density for the oxidative ageing process. These modifications require additional complexity to the network dynamics equation but will be required to capture the duality of the sulphur and oxidative secondary network behaviour. Due to the time constraints of this dissertation, this modification is relegated to future work but a trial model showed promise in the effectiveness of the constitutive model in modelling the peaking in the stiffness from Figure 6.7.

Chapter 7

Conclusion and outlook

7.1 Conclusion

In this dissertation, the oxidative ageing behaviour of elastomers has been introduced from a chemistry standpoint. A new constitutive model for the oxidative ageing model has been derived, implemented and verified in a finite element framework. Important physical aspects of oxidative ageing, such as permanent set, stress-free curing, stress softening and stiffening were included into the model. To complement the numerical aspect of modelling, experimental work has been performed to ascertain the current deficiencies in the model and provide hints for future model refinement.

The evolution of the cross-link density and the length of the polymer chains were derived based on a probabilistic approach for the chain scission and cross-linking reactions. A set of coupled, non-linear differential equations were then solved to determine the state of the polymer network. To capture the degradation, a novel mapping technique was introduced to store the degradation state of secondary networks that were created at previous time steps. This mapping technique allows the model to degrade the secondary networks created in previous time steps without explicitly storing the stress tensor at each time step. A micro-mechanically based constitutive model is then modified to include the continuous creation of secondary networks with respect to the deformation state they were created in. Exploiting properties of Gaussian models allowed this operation to be extremely computationally efficient and simulation of long ageing periods could be achieved.

A theoretical analysis was performed to ascertain the conditions under which thermodynamical consistency of the constitutive model is fulfilled. It was found that the network dynamics play a pivotal role, whereby the so-called dimensionless reduction factor rate must be zero or negative. A physical interpretation of the consistency is clear: the polymer must remain constant or be decaying over time. This simple condition allows rapid development of the network dynamics to include other effects without arduously confirming the thermodynamic consistency.

Numerical experiments of the proposed model showcased its ability in the modelling of polymers, reproducing both stress softening, stiffening and permanent set in uniaxial and general deformation states. The proposed model demonstrated clear advantages over the current state-of-the-art constitutive model for elastomer ageing, particularly in the ability to provide physically sound permanent set predictions and to include degradation of all networks, including secondary networks. Two finite element models of common engineering components demonstrated the ability of the model to produce stable solutions to medium scale problems, with large scale problems limited only by the available computation power.

Comparison of experimental results from the literature showed excellent agreement in predicting softening and stiffening. Consequently, a series of experiments were performed at the DIK (Deutsches Institut

für Kautschuktechnologie) to provide insight into ageing performance of current elastomers. Shortcomings in the assumptions of the idealised network dynamics were highlighted and attributed to the complex ageing behaviour, even when using a simple rubber formulation. Some potential ageing mechanisms were discussed and a concept for an extended network dynamics model was proposed.

7.2 Outlook

While the proposed model shows clear improvements over the current state-of-the-art constitutive model, selected extensions to the model will significantly advance the modelling capabilities. Comparisons with experimental data highlighted insufficiencies with a network dynamics model that can only reproduce exponential type increases or decreases in stiffness. The extension of the network dynamics model to include sulphur cross-linking could allow experimental validation with both the intermittent uniaxial stress and permanent set results. Additional ageing mechanisms could be enabled to gauge the effect on the mechanical behaviour, driving the development of a virtual material before beginning the synthesis of the desired polymer properties. The conditions of thermodynamic consistency derived in this dissertation are dependent on the simple inequalities related to the network dynamics thereby allowing extensions by chemists and physicists without requiring a re-derivation of the continuum mechanics model.

Further work to include the reaction-diffusion equation is of upmost importance to industrially relevant problems. The diffusion limited oxidation (DLO) effect is driven by the ability of oxygen to diffuse into an elastomer as it is required during the oxidative ageing process. Oxygen concentration directly effects the values of p_s and p_c, and a functional form dependent on the Arrhenius equation should be postulated. This dissertation is focused instead on the development of a constitutive model compatible with the inclusion of the DLO effect, but the scope was limited to understanding the network dynamics behaviour in situations where a saturation of oxygen exists. Several publications tackle the problem of coupling the diffusion-reaction equation to a constitutive model for oxidative ageing and is left as future work.

The limitations of Gaussian chain theory for the secondary network is perhaps the largest improvement to the mechanical model that can be made. Due to the linear nature of Gaussian theory, the secondary networks can be very efficiency compacted into a single accumulated stress and the novel mapping procedure can be used to elegantly compute the decay of previously created networks. Extending this framework to non-Gaussian theory presents significant challenges in computational efficiency. Several results that enabled simplifications in Gaussian theory are simply not present in non-Gaussian theory without resorting to an adhoc binning procedure of the secondary networks. Even if binning is chosen, it is not clear which strategy is optimal for selecting deformation states and destroys any possibility of using this idea in a general finite element framework. Promising new research suggests that it is possible to derive a probability density function specific to ageing and derive the constitutive model from first principles. Nevertheless, it was shown that the network dynamics are a major driver behind some complex time-dependent behaviour and quantification of these processes for mechanical model remains of critical importance.

Future work should also include viscoelasticity and contact problems to complete the multiphysical picture of engineering elastomers. For example, contact limits oxygen diffusion into the material and significant inhomogeneities in ageing occurs in apparently simple geometry, such as the engine mount. Coupling contact, reaction-diffusion and the mechanical model will be a significant undertaking but could produce a physically realistic stage in which to view oxidative ageing in elastomers.

Bibliography

[Andrews et al., 1946] Andrews, R. D., Tobolsky, A. V., and Hanson, E. E. (1946). The theory of permanent set at elevated temperatures in natural and synthetic rubber vulcanizates. *Journal of Applied Physics*, 17(5):352–361.

[Arruda and Boyce, 1993] Arruda, E. M. and Boyce, M. C. (1993). A three-dimensional constitutive model for the large stretch behavior of rubber elastic materials. *Journal of the Mechanics and Physics of Solids*, 41(2):389 – 412.

[Augustyn et al., 2019] Augustyn, A., Bauer, P., Duignan, B., Eldridge, A., Gregersen, E., McKenna, A., Petruzzello, M., Rafferty, J. P., Ray, M., Rogers, K., Tikkanen, A., Wallenfeldt, J., Zeidan, A., and Zelazko, A. (2019). "encyclopædia britannica".

[Bažant and Oh, 1986] Bažant, P. and Oh, B. H. (1986). Efficient numerical integration on the surface of a sphere. *ZAMM - Journal of Applied Mathematics and Mechanics / Zeitschrift für Angewandte Mathematik und Mechanik*, 66(1):37–49.

[Behnke and Kaliske, 2017] Behnke, R. and Kaliske, M. (2017). *The Extended Non-affine Tube Model for Crosslinked Polymer Networks: Physical Basics, Implementation, and Application to Thermomechanical Finite Element Analyses*, pages 1–70. Springer International Publishing, Cham.

[Belytschko et al., 2013] Belytschko, T., Liu, W., Moran, B., and Elkhodary, K. (2013). *Nonlinear Finite Elements for Continua and Structures*. No Longer used. Wiley.

[Bolland, 1949] Bolland, J. L. (1949). Kinetics of olefin oxidation. *Q. Rev. Chem. Soc.*, 3:1–21.

[Boyce and Arruda, 2000] Boyce, M. C. and Arruda, E. M. (2000). Constitutive models of rubber elasticity: A review. *Rubber Chemistry and Technology*, 73(3):504–523.

[Brown, 2007] Brown, T. (2007). *Chemistry: The Central Science : A Broad Perspective*. Pearson Education Australia.

[Budzien et al., 2008] Budzien, J., Rottach, D. R., Curro, J. G., Lo, C. S., and Thompson, A. P. (2008). A new constitutive model for the chemical aging of rubber networks in deformed states. *Macromolecules*, 41(24):9896–9903.

[Callister, 2007] Callister, W. (2007). *Materials Science And Engineering: An Introduction*. John Wiley & Sons.

[Chung, 2007] Chung, T. (2007). *General Continuum Mechanics*. General Continuum Mechanics. Cambridge University Press.

[de Souza Neto et al., 2011] de Souza Neto, E., Peric, D., and Owen, D. (2011). *Computational Methods for Plasticity: Theory and Applications*. Wiley.

[Dippel et al., 2014] Dippel, B., Johlitz, M., and Lion, A. (2014). Ageing of polymer bonds: a coupled chemomechanical modelling approach. *Continuum Mechanics and Thermodynamics*, 26(3):247–257.

[Doi and Edwards, 1988] Doi, M. and Edwards, S. (1988). *The Theory of Polymer Dynamics*. International series of monographs on physics. Clarendon Press.

[Doll and Schweizerhof, 1999] Doll, S. and Schweizerhof, K. (1999). On the development of volumetric strain energy functions. *Journal of Applied Mechanics*, 67(17).

[Doyle and Erickson, 1959] Doyle, T. and Erickson, J. (1959). *Nonlinear Elasticity, Advances in Applied Mechanics IV*, pages 53–115. New York: Academic Press.

[Edwards, 1965] Edwards, S. F. (1965). The statistical mechanics of polymers with excluded volume. *Proceedings of the Physical Society*, 85(4):613.

[Edwards, 1967a] Edwards, S. F. (1967a). The statistical mechanics of polymerized material. *Proceedings of the Physical Society*, 92(1):9.

[Edwards, 1967b] Edwards, S. F. (1967b). Statistical mechanics with topological constraints: I. *Proceedings of the Physical Society*, 91(3):513.

[Ehret et al., 2010] Ehret, A. E., Itskov, M., and Schmid, H. (2010). Numerical integration on the sphere and its effect on the material symmetry of constitutive equations—a comparative study. *International Journal for Numerical Methods in Engineering*, 81(2):189–206.

[Flory and Jr., 1943] Flory, P. J. and Jr., J. R. (1943). Statistical mechanics of cross-linked polymer networks I. rubberlike elasticity. *The Journal of Chemical Physics*, 11(11):512–520.

[Göktepe, 2007] Göktepe, S. (2007). *Micro-macro approaches to rubbery and glassy polymers : predictive micromechanically-based models and simulations*. PhD thesis, Institut für Mechanik (Bauwesen).

[Göktepe and Miehe, 2004] Göktepe, S. and Miehe, C. (2004). The micro-sphere model for rubber viscoelasticity: A micromechanically based network model for polymers. *PAMM*, 4(1):191–192.

[Govindjee and Simo, 1992a] Govindjee, S. and Simo, J. (1992a). Transition from micro-mechanics to computationally efficient phenomenology: Carbon black filled rubbers incorporating mullins' effect. *Journal of the Mechanics and Physics of Solids*, 40(1):213 – 233.

[Govindjee and Simo, 1992b] Govindjee, S. and Simo, J. C. (1992b). Mullins' effect and the strain amplitude dependence of the storage modulus. *International Journal of Solids and Structures*, 29(14):1737 – 1751.

[Gryn'ova et al., 2011] Gryn'ova, G., Hodgson, J. L., and Coote, M. L. (2011). Revising the mechanism of polymer autooxidation. *Org. Biomol. Chem.*, 9:480–490.

[Göktepe and Miehe, 2005] Göktepe, S. and Miehe, C. (2005). A micro–macro approach to rubber-like materials. Part III: The micro-sphere model of anisotropic mullins-type damage. *Journal of the Mechanics and Physics of Solids*, 53(10):2259 – 2283.

78

[Heinrich and Kaliske, 1997] Heinrich, G. and Kaliske, M. (1997). Theoretical and numerical formulation of a molecular based constitutive tube-model of rubber elasticity. *Computational and Theoretical Polymer Science*, 7(3):227 – 241.

[Herzig et al., 2015] Herzig, A., Johlitz, M., and Lion, A. (2015). An experimental set-up to analyse the oxygen consumption of elastomers during ageing by using a differential oxygen analyser. *Continuum Mechanics and Thermodynamics*, 27(6):1009–1017.

[Herzig et al., 2017] Herzig, A., Sekerakova, L., Johlitz, M., and Lion, A. (2017). A modelling approach for the heterogeneous oxidation of elastomers. *Continuum Mechanics and Thermodynamics*, 29(5):1149–1161.

[Hesse et al., 2015] Hesse, K., Sloan, I. H., and Womersley, R. S. (2015). *Numerical Integration on the Sphere*, pages 2671–2710. Springer Berlin Heidelberg, Berlin, Heidelberg.

[Holzapfel, 2002] Holzapfel, G. A. (2002). Nonlinear solid mechanics: A continuum approach for engineering science. *Meccanica*, 37(4):489–490.

[Horgan and Murphy, 2009] Horgan, C. O. and Murphy, J. G. (2009). On the volumetric part of strain-energy functions used in the constitutive modeling of slightly compressible solid rubbers. *International Journal of Solids and Structures*, 46(16):3078 – 3085.

[Hossain, 2010] Hossain, M. (2010). *Modelling and Computation of Polymer Curing*. PhD thesis, Der Technischen Fakultät der Universität Erlangen Nürnberg.

[Hossain et al., 2009a] Hossain, M., Possart, G., and Steinmann, P. (2009a). A finite strain framework for the simulation of polymer curing. Part I: elasticity. *Computational Mechanics*, 44(5):621–630.

[Hossain et al., 2009b] Hossain, M., Possart, G., and Steinmann, P. (2009b). A small-strain model to simulate the curing of thermosets. *Computational Mechanics*, 43(6):769–779.

[Hughes, 2012] Hughes, T. (2012). *The Finite Element Method: Linear Static and Dynamic Finite Element Analysis*. Dover Civil and Mechanical Engineering. Dover Publications.

[Itskov, 2016] Itskov, M. (2016). On the accuracy of numerical integration over the unit sphere applied to full network models. *Computational Mechanics*, 57(5):859–865.

[James and Guth, 1943] James, H. M. and Guth, E. (1943). Theory of the elastic properties of rubber. *The Journal of Chemical Physics*, 11(10):455–481.

[Jedynak, 2015] Jedynak, R. (2015). Approximation of the inverse Langevin function revisited. *Rheologica Acta*, 54(1):29–39.

[Ji et al., 2013] Ji, W., Waas, A. M., and Bazant, Z. P. (2013). On the Importance of Work-Conjugacy and Objective Stress Rates in Finite Deformation Incremental Finite Element Analysis. *Journal of Applied Mechanics*, 80(4). 041024.

[Johlitz et al., 2014] Johlitz, M., Diercks, N., and Lion, A. (2014). Thermo-oxidative ageing of elastomers: A modelling approach based on a finite strain theory. *International Journal of Plasticity*, 63:138 – 151. Deformation Tensors in Material Modeling in Honor of Prof. Otto T. Bruhns.

[Johlitz and Lion, 2013] Johlitz, M. and Lion, A. (2013). Chemo-thermomechanical ageing of elastomers based on multiphase continuum mechanics. *Continuum Mechanics and Thermodynamics*, 25(5):605–624.

[Kreiselmaier et al., 2014] Kreiselmaier, R., Beck, K., Paimann, P., Priess, C., Traber, B., and Stein, G. (2014). Model for the oxidative ageing process of elastomers. *International Polymer Science and Technology*, 41(9):1–4.

[Kuhn, 1952] Kuhn, W. (1952). Beziehung zwischen Molekülgrösse, statistischer Molekülgestalt und elastischen Eigenschaften hochpolymerer Stoffe. *Kolloid-Zeitschrift*, 76:258–271.

[Kuhn and Grün, 1942] Kuhn, W. and Grün, F. (1942). Beziehungen zwischen elastischen Konstanten und Dehnungsdoppelbrechung hochelastischer Stoffe. *Kolloid-Zeitschrift*, 101(3):248–271.

[Lebedev, 1976] Lebedev, V. (1976). Quadratures on a sphere. *USSR Computational Mathematics and Mathematical Physics*, 16(2):10 – 24.

[Lee, 1969] Lee, E. H. (1969). Elastic-plastic deformation at finite strains. *ASME*, 36(1):1–6.

[Lion and Johlitz, 2012] Lion, A. and Johlitz, M. (2012). On the representation of chemical ageing of rubber in continuum mechanics. *International Journal of Solids and Structures*, 49(10):1227 – 1240.

[Lion et al., 2011] Lion, A., Peters, J., and Kolmeder, S. (2011). Simulation of temperature history-dependent phenomena of glass-forming materials based on thermodynamics with internal state variables. *Thermochimica Acta*, 522(1):182 – 193. Special Issue: Interplay between Nucleation, Crystallization, and the Glass Transition.

[Maiti et al., 2014] Maiti, A., Small, W., Gee, R. H., Weisgraber, T. H., Chinn, S. C., Wilson, T. S., and Maxwell, R. S. (2014). Mullins effect in a filled elastomer under uniaxial tension. *Phys. Rev. E*, 89:012602.

[Marckmann and Verron, 2006] Marckmann, G. and Verron, E. (2006). Comparison of hyperelastic models for rubber-like materials. *Rubber Chemistry and Technology*, 79(5):835–858.

[Marsden and Hughes, 1994] Marsden, J. E. and Hughes, T. J. R. (1994). *Mathematical foundations of elasticity*. Dover Civil and Mechanical Engineering. Dover, Mineola, NY.

[Miehe, 1994] Miehe, C. (1994). Aspects of the formulation and finite element implementation of large strain isotropic elasticity. *International Journal for Numerical Methods in Engineering*, 37(12):1981–2004.

[Miehe et al., 2004] Miehe, C., Göktepe, S., and Lulei, F. (2004). A micro-macro approach to rubber-like materials. Part I: the non-affine micro-sphere model of rubber elasticity. *Journal of the Mechanics and Physics of Solids*, 52(11):2617–2660.

[Miehe and Göktepe, 2005] Miehe, C. and Göktepe, S. (2005). A micro–macro approach to rubber-like materials. Part II: The micro-sphere model of finite rubber viscoelasticity. *Journal of the Mechanics and Physics of Solids*, 53(10):2231 – 2258.

[Mistry and Govindjee, 2014] Mistry, S. J. and Govindjee, S. (2014). A micro-mechanically based continuum model for strain-induced crystallization in natural rubber. *International Journal of Solids and Structures*, 51(2):530 – 539.

[Mooney, 1940] Mooney, M. (1940). A theory of large elastic deformation. *Journal of Applied Physics*, 11(9):582–592.

[Nasdala et al., 2005] Nasdala, L., Kaliske, M., and Rothert, H. (2005). Entwicklung von Materialmodellen zur Alterung von Elastomerwerkstoffen unter besonderer Beruecksichtigung des Sauerstoffeinflusses.

[Naumann, 2017] Naumann, C. (2017). *Chemisch-mechanisch gekoppelte Modellierung und Simulation oxidativer Alterungsvorgänge in Gummibauteilen*. PhD thesis.

[Nocil, 2010] Nocil (2010). Vulcanization and accelerators.

[Penrose, 1969] Penrose, O. (1969). *Foundations of statistical mechanics: a deductive treatment*. International series of monographs in natural philosophy. Pergamon Press.

[Pyckhout-Hintzen et al., 2013] Pyckhout-Hintzen, W., Westermann, S., Wischnewski, A., Monkenbusch, M., Richter, D., Straube, E., Farago, B., and Lindner, P. (2013). Direct observation of nonaffine tube deformation in strained polymer networks. *Phys. Rev. Lett.*, 110:196002.

[Rajagopal and Wineman, 1992] Rajagopal, K. and Wineman, A. (1992). A constitutive equation for nonlinear solids which undergo deformation induced microstructural changes. *International Journal of Plasticity*, 8(4):385 – 395.

[Rivlin, 1948] Rivlin, R. S. (1948). Large elastic deformations of isotropic materials IV. further developments of the general theory. *Philosophical Transactions of the Royal Society of London A: Mathematical, Physical and Engineering Sciences*, 241(835):379–397.

[Rubinstein and Panyukov, 2002] Rubinstein, M. and Panyukov, S. (2002). Elasticity of polymer networks. *Macromolecules*, 35(17):6670–6686.

[Schlömer, 2018] Schlömer, N. (2018). nschloe/quadpy v0.11.3. `https://doi.org/10.5281/zenodo.1173133`.

[Staggs, 2002] Staggs, J. (2002). Modelling random scission of linear polymers. *Polymer Degradation and Stability*, 76(1):37 – 44.

[Staggs, 2004] Staggs, J. (2004). Modelling end-chain scission and recombination of linear polymers. *Polymer Degradation and Stability*, 85(2):759 – 767.

[Stegen, 2014] Stegen, O. (2014). *A fully micromechanically motivated material law for filled elastomers*. PhD thesis, Institute for Mechanics and Numerical Mechanics, Gottfried Leibniz Universität Hannover, Germany.

[Steinke et al., 2011] Steinke, L., Weltin, U., and Flamm, M. (2011). *Numerical analysis of the heterogeneous ageing of rubber products*, pages 155–160. CRC Press.

[Strang and Fix, 2008] Strang, G. and Fix, G. (2008). *An Analysis of the Finite Element Method*. Wellesley-Cambridge Press.

[Tobolsky et al., 1961] Tobolsky, A. V., Carlson, D. W., and Indictor, N. (1961). Rubber elasticity and chain configuration. *Journal of Polymer Science*, 54(159):175–192.

[Tobolsky et al., 1944] Tobolsky, A. V., Prettyman, I. B., and Dillon, J. H. (1944). Stress relaxation of natural and synthetic rubber stocks. *Journal of Applied Physics*, 15(4):380–395.

[Treloar, 1975] Treloar, L. (1975). *The Physics of Rubber Elasticity*. Monographs on the physics and chemistry of materials. Oxford University Press, USA.

[Treloar, 1944] Treloar, L. R. G. (1944). Stress-strain data for vulcanised rubber under various types of deformation. *Trans. Faraday Soc.*, 40:59–70.

[Vernerey, 2018] Vernerey, F. J. (2018). Transient response of nonlinear polymer networks: A kinetic theory. *Journal of the Mechanics and Physics of Solids*, 115:230 – 247.

[Verron, 2015] Verron, E. (2015). Questioning numerical integration methods for microsphere (and microplane) constitutive equations. *Mechanics of Materials*, 89:216 – 228.

[Wang and Guth, 1952] Wang, M. C. and Guth, E. (1952). Statistical Theory of Networks of Non-Gaussian Flexible Chains. *The Journal of Chemical Physics*, 20(7):1144–1157.

[Williams, 1926] Williams, I. (1926). Oxidation of rubber exposed to light. *Industrial & Engineering Chemistry*, 18(4):367–369.

[Wriggers, 2008] Wriggers, P. (2008). *Nonlinear Finite Element Methods*. Springer Berlin Heidelberg.

Appendix A

Tensor algebra

Tensors experience heavy usage in non-linear continuum mechanics to describe relationships between kinetic and kinematic tensor-valued variables. While specialised computing languages can evaluate these expressions (see AceGen), general purpose programming languages do not readily provide tooling to assist in tensor operation evaluation. However, using particular transforms, it is possible to express operations involving fourth-order tensors using well defined matrix-vector and matrix-matrix operations. This has the advantage of leveraging a highly optimised routines that are already developed.

In operations involving fourth-order tensors, there are two commonly used transformations; Voigt and Mandel transformations. A Voigt transformation allows a matrix-vector multiplication to correspond to a contraction (double dot product) on a fourth and second order tensor, viz.,

$$C_{ijkl}\varepsilon_{kl} = \boldsymbol{C} : \boldsymbol{\varepsilon} = \boldsymbol{C}\boldsymbol{\varepsilon} \ . \tag{A.1}$$

A.1 O-dot notation

In the development of the non-affine microsphere model, the *o-dot* operator is defined as

$$\text{sym}(\boldsymbol{M} \odot \boldsymbol{N}) = \frac{1}{2}\left(M_{ik}N_{jl} + M_{jk}N_{il}\right) \tag{A.2}$$

With the knowledge that $\boldsymbol{M}$ is the metric tensor $\boldsymbol{g}$, we can instead write this as

$$\text{sym}(\boldsymbol{g}^{-1} \odot \boldsymbol{N}) = \frac{1}{2}(\delta^{ik}N_{jl} + \delta^{jk}N_{il}) \tag{A.3}$$

The full expression required for evaluation is

$$\text{sym}(\boldsymbol{g}^{-1} \odot \boldsymbol{N} + \boldsymbol{N} \odot \boldsymbol{g}^{-1}) = \frac{1}{2}(\delta^{ik}N_{jl} + \delta^{jk}N_{il} + N_{ik}\delta^{jl} + N_{jk}\delta^{il}) \tag{A.4}$$

Using $\boldsymbol{g} = \delta$, we can express this in Voigt notation as

$$\text{sym}(\boldsymbol{g}^{-1} \odot \boldsymbol{N} + \boldsymbol{N} \odot \boldsymbol{g}^{-1}) = \begin{bmatrix} 2N_{11} & 0 & 0 & 0 & N_{13} & N_{12} \\ & 2N_{22} & 0 & N_{23} & 0 & N_{12} \\ & & 2N_{33} & N_{23} & N_{13} & 0 \\ & & & (N_{22}+N_{33})/2 & N_{12}/2 & N_{13}/2 \\ & \text{sym} & & & (N_{11}+N_{33})/2 & N_{32}/2 \\ & & & & & (N_{11}+N_{22})/2 \end{bmatrix}$$

$$\tag{A.5}$$

A.2 Second order tensor properties

Some useful identities for tensor algebra from [de Souza Neto et al., 2011] are presented here without proof.

$$\mathbf{1} : \boldsymbol{T} = \text{tr}\,(\boldsymbol{T}) \tag{A.6}$$

$$\boldsymbol{R} : \boldsymbol{S} \cdot \boldsymbol{T} = \boldsymbol{S}^{\text{T}} \cdot \boldsymbol{R} : \boldsymbol{T} = (\boldsymbol{R} \cdot \boldsymbol{T}^{\text{T}}) : \boldsymbol{S} \tag{A.7}$$

$$\boldsymbol{u} \cdot \boldsymbol{S}\boldsymbol{v} = \boldsymbol{S} : (\boldsymbol{u} \otimes \boldsymbol{v}) \tag{A.8}$$

$$(\boldsymbol{s} \otimes \boldsymbol{t}) : (\boldsymbol{u} \otimes \boldsymbol{v}) = (\boldsymbol{s} \cdot \boldsymbol{u})(\boldsymbol{t} \cdot \boldsymbol{v}) \tag{A.9}$$

A subset of available tensor function derivatives are presented from [Holzapfel, 2002], including the important identity for the derivative

$$\frac{\partial \det \boldsymbol{A}}{\partial \boldsymbol{A}} = \det \boldsymbol{A} \boldsymbol{A}^{-T} \tag{A.10}$$

When using a generalised coordinate system, the trace of a second order tensor is given by

$$\text{tr}\,(\boldsymbol{A}) = g^{ij} A_{ij} = g_{ij} A^{ij} \tag{A.11}$$

or in matrix notation

$$\text{tr}\,(\boldsymbol{A}) = \boldsymbol{g}^{-1} \boldsymbol{A} = \boldsymbol{g} \boldsymbol{A} \tag{A.12}$$

$$\boldsymbol{S} \cdot (\boldsymbol{u} \otimes \boldsymbol{v}) = \boldsymbol{S} \cdot \boldsymbol{u} \otimes \boldsymbol{v} \tag{A.13}$$

$$(\boldsymbol{u} \otimes \boldsymbol{v}) \cdot \boldsymbol{S} = \boldsymbol{u} \otimes \boldsymbol{S}^{\text{T}} \cdot \boldsymbol{v} \tag{A.14}$$

A.3 Fourth order tensor properties

Given a fourth order tensor $\mathbb{T}$ and two second order tensors $\boldsymbol{S}$ and $\boldsymbol{U}$, $\mathbb{T}$ is said to be symmetric if

$$\boldsymbol{S} : \mathbb{T} : \boldsymbol{U} = (\mathbb{T} : \boldsymbol{S}) : \boldsymbol{U} \tag{A.15}$$

is satisfied. Some additional identities from [Holzapfel, 2002], where $\boldsymbol{A}$, $\boldsymbol{B}$ and $\boldsymbol{C}$ are second order tensors

$$(\boldsymbol{A} \otimes \boldsymbol{B}) : \boldsymbol{C} = \boldsymbol{A} \cdot (\boldsymbol{B} : \boldsymbol{C}) = (\boldsymbol{B} : \boldsymbol{C}) \cdot \boldsymbol{A} \tag{A.16}$$

$$\boldsymbol{A} : (\boldsymbol{B} \otimes \boldsymbol{C}) = (\boldsymbol{A} : \boldsymbol{B}) \cdot \boldsymbol{C} = \boldsymbol{C} \cdot (\boldsymbol{A} : \boldsymbol{B}) \tag{A.17}$$

$$(\boldsymbol{A} \otimes \boldsymbol{B}) : (\boldsymbol{C} \otimes \boldsymbol{D}) = (\boldsymbol{B} : \boldsymbol{C})(\boldsymbol{A} \otimes \boldsymbol{D}) = (\boldsymbol{A} \otimes \boldsymbol{D})(\boldsymbol{B} : \boldsymbol{C}) \tag{A.18}$$

and some identities for contraction of fourth order tensors

$$\boldsymbol{B} : \mathbb{A}^{\text{T}} : \boldsymbol{C} = \boldsymbol{C} : \mathbb{A} : \boldsymbol{B} = (\mathbb{A} : \boldsymbol{B}) : \boldsymbol{C} \,. \tag{A.19}$$

Appendix B

Statistical mechanics of cross-linking

A statistical mechanical approach for polymer ageing can be explored by a modification of the probability distribution functions when the chain is subject to a cross-linking reaction. Consider Figure B.1 where the cross-link occurs between segment n and m on the chain. The chain has a reduced number of possible conformations available due to the additional cross-linking constraint. We will apply Gaussian chain theory in order to derive a free energy function for the cross-linked chain. The background for the theory presented in this appendix can be found in [Doi and Edwards, 1988].
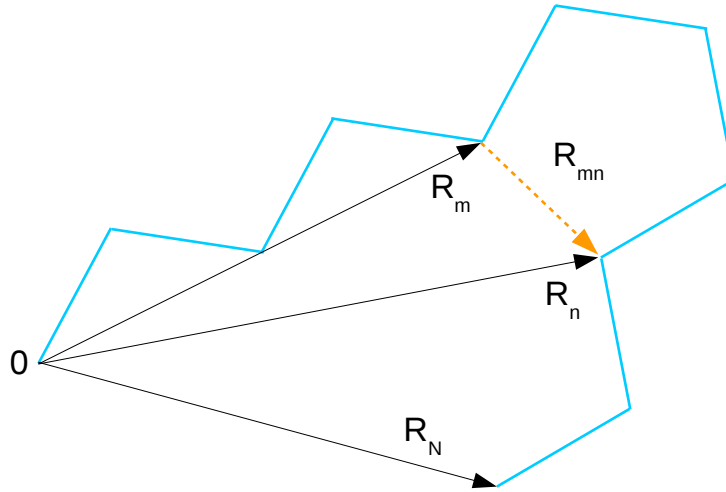
Figure B.1: A polymer chain with N segments. An internal cross-link is shown at segment m and n.

We begin by defining some known quantities. Consider Figure B.1, where the end-to-end vector is given by $\boldsymbol{R}_N$. Assuming that each segment has a Gaussian distribution for the conformation and that each bond is restricted to rotate with a fixed angle θ from the previous segment, the conformation distribution for a single segment is given by

$$\Omega_f(\boldsymbol{r}) = \left(\frac{3}{2\pi b^2}\right)^{\frac{3}{2}} \exp\left(-\frac{3\boldsymbol{r}^2}{2b^2}\right) \ , \tag{B.1}$$

where b is the segment length and $\boldsymbol{r}$ is the segment vector such that $||\boldsymbol{r}||_2 = b$. Since each segment is independent, the total conformation distribution of the chain is expressed as the product of the individual

segment distributions of (B.1), viz.,

$$\Omega(\{\boldsymbol{r}_n\}) = \prod_{n=1}^{N} \Omega_f(\boldsymbol{r}_n) \tag{B.2}$$

$$= \prod_{n=1}^{N} \left(\frac{3}{2\pi b^2}\right)^{\frac{3}{2}} \exp\left(-\frac{3\boldsymbol{r}_n^2}{2b^2}\right) . \tag{B.3}$$

Using the properties of the exponential functions, (B.3) can be simplified to

$$\Omega(\{\boldsymbol{r}_n\}) = \left(\frac{3}{2\pi b^2}\right)^{\frac{3N}{2}} \exp\left(-\frac{3}{2b^2}\sum_{n=1}^{N} \boldsymbol{r}_n^2\right) \tag{B.4}$$

$$= \left(\frac{3}{2\pi b^2}\right)^{\frac{3N}{2}} \exp\left(-\frac{3}{2b^2}\sum_{n=1}^{N}(\boldsymbol{R}_n - \boldsymbol{R}_{n-1})^2\right) . \tag{B.5}$$

According to [Doi and Edwards, 1988], the conformation distribution function can also be written as in terms of a harmonic potential

$$U_0(\{\boldsymbol{R}_n\}) = \frac{3}{2b^2}k_B T \sum_{n=1}^{N}(\boldsymbol{R}_n - \boldsymbol{R}_{n-1})^2 . \tag{B.6}$$

The probability distribution function of the end-to-end vector $\boldsymbol{R}$ of a chain with N segments can be evaluated from the integral

$$\Omega(\boldsymbol{R}, N) = \int d\boldsymbol{r}_1 \int d\boldsymbol{r}_2 \ldots \int d\boldsymbol{r}_n \delta\left(\boldsymbol{R} - \sum_{n=1}^{N} \boldsymbol{r}_n\right) \Omega(\{\boldsymbol{r}_n\}) . \tag{B.7}$$

With the aid of the Dirac distribution Fourier transform, (B.7) can be simplified to

$$\Omega(\boldsymbol{R}, N) = \frac{1}{(2\pi)^3} \int d\boldsymbol{k} \exp(i\boldsymbol{k}\cdot\boldsymbol{R}) \int d\boldsymbol{r}_1 \ldots \int d\boldsymbol{r}_N \prod_{n=1}^{N} \exp\left(-i\boldsymbol{k}\cdot\boldsymbol{r}_n\right) \Omega_f(\boldsymbol{r}_n) \tag{B.8}$$

$$= \frac{1}{(2\pi)^3} \int d\boldsymbol{k} \exp(i\boldsymbol{k}\cdot\boldsymbol{R}) \int d\boldsymbol{r} [\exp\left(-i\boldsymbol{k}\cdot\boldsymbol{r}\right)\Omega_f(\boldsymbol{r})]^N . \tag{B.9}$$

Consider the transformation of (B.9) into spherical coordinates

$$\int d\boldsymbol{r} \exp(-i\boldsymbol{k}\cdot\boldsymbol{r})\Omega_f(\boldsymbol{r}) = \frac{1}{4\pi b^2} \int_0^\infty dr r^2 \int_0^{2\pi} d\Omega_f \int_0^\pi d\theta \sin\theta \exp(-ikr\cos\theta)\delta(r - b) \tag{B.10}$$

$$= \frac{\sin(kb)}{kb} \tag{B.11}$$

which leads to

$$\Omega(\boldsymbol{R}, N) = \frac{1}{(2\pi)^3} \int d\boldsymbol{k} \exp(i\boldsymbol{k}\cdot\boldsymbol{R}) \left(\frac{\sin kb}{kb}\right)^N . \tag{B.12}$$

If the term kb is small, then $(\sin(kb)/kb)^N$ can be approximated as

$$\left(\frac{\sin kb}{kb} \right)^N \approx \left(1 - \frac{k^2 b^2}{6} \right)^N \approx \exp\left(-\frac{N k^2 b^2}{6} \right) . \tag{B.13}$$

This leads to the integral

$$\Omega(\boldsymbol{R}, N) = \frac{1}{(2\pi)^3} \int \mathrm{d}\boldsymbol{k} \exp(i\boldsymbol{k} \cdot \boldsymbol{R}) \exp\left(-\frac{N k^2 b^2}{6} \right) . \tag{B.14}$$

Performing the integration using identities for the Gaussian integral, it is possible to obtain

$$\Omega(\boldsymbol{R}, N) = \frac{1}{(2\pi)^3} \prod_{\alpha=x,y,z} \left[\int_{-\infty}^{\infty} dk_\alpha \exp(i k_\alpha R_\alpha - N k_\alpha^2 b^2/6) \right] \tag{B.15}$$

$$= \frac{1}{(2\pi)^3} \prod_{\alpha=x,y,z} \left(\frac{6\pi}{Nb^2} \right)^{1/2} \exp\left(-\frac{3}{2Nb^2} R_\alpha^2 \right) \tag{B.16}$$

$$= \left(\frac{3}{2\pi Nb^2} \right)^{3/2} \exp\left(-\frac{3\boldsymbol{R}^2}{2Nb^2} \right) . \tag{B.17}$$

With (B.17) in hand, it is a small leap to obtain the free energy function through the Boltzmann equation

$$\psi_f(\boldsymbol{R}) = -k_B T \ln \Omega(\boldsymbol{R}, N) , \tag{B.18}$$

from which the chain force can be computed. However this does not include considerations of cross-linking. For this we invoke an interesting property of the Gaussian statistics, namely that a sub-chain between segments n and m is also Gaussian distributed

$$\Omega(\boldsymbol{R}_n - \boldsymbol{R}_m, q - p) = \left(\frac{3}{2\pi b^2 |q - p|} \right)^{\frac{3}{2}} \exp\left(-\frac{3}{2} \frac{(\boldsymbol{R}_n - \boldsymbol{R}_m)^2}{|q - p| b^2} \right) . \tag{B.19}$$

Recall the chain in Figure B.1, from (B.19) this implies that the system could be described by three Gaussian chains if the cross-link constraint is ignored. The only remaining task to complete is the constraint on the available conformations that the cross-link enforces. Returning to (B.2), the total conformation is the multiplication of the individual segments.

The available conformations for the chain section between p and q is reduced. The remaining chain from 0 to p and q to N is also affected. Naturally, a reduction in the number of conformations is expected and the distribution needs to be adjusted accordingly.

If it is recognised that the cross-link has a distribution of the end-to-end vector given simply by a Gaussian distribution of the polymer chain between cross-link sites then (B.19) can be applied. The available conformations after cross-linking is then described by

$$\Omega(\boldsymbol{R}, N) = \prod_{n=0}^{N-(q-p)} \Omega_f(\boldsymbol{r}_i) \tag{B.20}$$

where the $q - p$ is the section of chain removed by the internal cross-link. To include the effect of cross-link formation in the zero-stress configuration, we require some additional developments to enforce this

condition. Since $N - (q - p)$ is simply a reduction in the number of segments, we can write this as $\bar{N} = N - (q - p)$, simplifying (B.20) with the modified $\bar{N}$ provides

$$\Omega(\boldsymbol{R}, \bar{N}) = \prod_{n=0}^{\bar{N}} \Omega_f(\boldsymbol{r}_i) . \tag{B.21}$$

The derivation that follows (B.21) is identical except the for the inclusion of $\bar{N}$,

$$\Omega(\boldsymbol{R}, \bar{N}) = \left(\frac{3}{2\pi \bar{N} b^2} \right)^{3/2} \exp \left(-\frac{3\boldsymbol{R}^2}{2\bar{N} b^2} \right) . \tag{B.22}$$

Consider the following: a chain in the virgin state undergoes an internal cross-link reaction that leads to a modified free energy function from (B.22). Following the derivation of the Neo-Hooke model [Treloar, 1975], the entropy between the states is related by $s = k \ln \Omega(\boldsymbol{R}, N)$ can be written as

$$s_0 = k\frac{3}{2} \ln \left(\frac{3}{2\pi N b^2} \right) - k\frac{3r_0^2}{2N b^2} \tag{B.23}$$

for the initial state and for the cross-linked state without applied deformation

$$s_\chi = k\frac{3}{2} \ln \left(\frac{3}{2\pi \bar{N} b^2} \right) - k\frac{3r_0^2}{2\bar{N} b^2} . \tag{B.24}$$

Applying a deformation to the χ state leads to

$$s_{\chi,1} = k\frac{3}{2} \ln \left(\frac{3}{2\pi \bar{N} b^2} \right) - k\frac{3r^2}{2\bar{N} b^2} \tag{B.25}$$

The difference in entropy between the states is given by

$$\Delta s = s_{\chi,1} - s_0 \tag{B.26}$$

$$= -k\frac{3}{2\bar{N} b^2} r^2 + k\frac{3}{2N b^2} r_0^2 + \frac{3k}{2} \left[\ln \left(\frac{3}{2\pi \bar{N} b^2} \right) - \ln \left(\frac{3}{2\pi N b^2} \right) \right] \tag{B.27}$$

$$= -k\frac{3}{2b^2} \left(\frac{1}{\bar{N}} r^2 - \frac{1}{N} r_0^2 \right) + \frac{3k}{2} \left[\ln \left(\frac{N}{\bar{N}} \right) \right] . \tag{B.28}$$

Reintroducing the definition of $\bar{N} = N - (q - p)$ and letting $\Delta N = q - p$, some rearrangement yields

$$\Delta s = -k\frac{3}{2b^2} \left(\frac{1}{N - \Delta N} \frac{N}{N} r^2 - \frac{1}{N} r_0^2 \right) + \frac{3k}{2} \ln(\widetilde{N}) \tag{B.29}$$

$$= -k\frac{3}{2N b^2} \left(\frac{N}{N - \Delta N} r^2 - r_0^2 \right) + \frac{3k}{2} \ln(\widetilde{N}) \tag{B.30}$$

$$= -k\frac{3}{2N b^2} \left(\widetilde{N} r^2 - r_0^2 \right) + \frac{3k}{2} \ln(\widetilde{N}) , \tag{B.31}$$

where $\widetilde{N} = N/(N - \Delta N)$. Since $\Delta N \le N$ and ignoring the singularly if a cross-link occurs between the chain ends, $\widetilde{N} \ge 1$. Using the following definitions for r

$$r_0^2 = x_0^2 + y_0^2 + z_0^2 \tag{B.32}$$
$$r^2 = x^2 + y^2 + z^2 \tag{B.33}$$

the change in entropy is then represented by

$$\Delta s = -k\frac{3}{2Nb^2}\left(\widetilde{N}(x^2+y^2+z^2)-(x_0^2+y_0^2+z_0^2)\right)+\frac{3k}{2}\ln(\widetilde{N})\,, \tag{B.34}$$

and invoking the affine assumption for the chains (i.e., the chains are aligned in the direction of deformation),

$$x = \lambda_1 x_0 \tag{B.35}$$
$$y = \lambda_2 y_0 \tag{B.36}$$
$$z = \lambda_3 z_0 \,, \tag{B.37}$$

gives the change in entropy of

$$\Delta s = -k\frac{3}{2Nb^2}\left(\widetilde{N}((\lambda_1 x_0)^2+(\lambda_2 y_0)^2+(\lambda_3 z_0)^2)-(x_0^2+y_0^2+z_0^2)\right)+\frac{3k}{2}\ln(\widetilde{N}) \tag{B.38}$$

$$= -k\frac{3}{2Nb^2}\left(x_0^2(\widetilde{N}\lambda_1^2-1)+y_0^2(\widetilde{N}\lambda_2^2-1)+z_0^2(\widetilde{N}\lambda_3^2-1)\right)+\frac{3k}{2}\ln(\widetilde{N})\,. \tag{B.39}$$

The total change in entropy of the chain system can be computed by summing over the individual entropies

$$\Delta S = \sum \Delta s = -\frac{3k}{2Nb^2}\left(\sum x_0^2(\widetilde{N}\lambda_1^2-1)+\sum y_0^2(\widetilde{N}\lambda_2^2-1)+\sum z_0^2(\widetilde{N}\lambda_3^2-1)\right)$$
$$+\frac{3k}{2}\ln(\widetilde{N})\,. \tag{B.40}$$

Note that due to the independence of the chain segments, the sum of the directions for each axis can be written as

$$\sum x_0^2 = \sum y_0^2 = \sum z_0^2 = \frac{1}{3}\sum r_0^2 \tag{B.41}$$

and

$$\sum r_0^2 = n\bar{r}_0^2\,. \tag{B.42}$$

The total change in entropy is then

$$\Delta S = -\frac{3k}{3\times 2Nb^2}n\bar{r}_0^2\left(\widetilde{N}\lambda_1^2-1+\widetilde{N}\lambda_2^2-1+\widetilde{N}\lambda_3^2-1\right)+\frac{3nk}{2}\ln(\widetilde{N}) \tag{B.43}$$

$$= -\frac{k}{2Nb^2}\bar{r}_0^2\left(\widetilde{N}(\lambda_1^2+\lambda_2^2+\lambda_3^2)-3\right)+\frac{3nk}{2}\ln(\widetilde{N})\,, \tag{B.44}$$

with the average chain end-to-end distance given by $\bar{r}_0^2 = Nb^2$,

$$\Delta S = -\frac{1}{2}nk\left(\widetilde{N}(\lambda_1^2+\lambda_2^2+\lambda_3^2)-3\right)+\frac{3nk}{2}\ln(\widetilde{N})\,. \tag{B.45}$$

Using the identity $\bar{\Psi} = -T\Delta S$ for the total free energy,

$$\bar{\Psi} = \frac{1}{2}nkT\left(\widetilde{N}(\lambda_1^2+\lambda_2^2+\lambda_3^2)-3\right)-\frac{3nkT}{2}\ln(\widetilde{N}) \tag{B.46}$$

$$= \frac{1}{2}nkT\left(\widetilde{N}I_{\bar{\mathbf{C}}}-3\right)-\frac{3nkT}{2}\ln(\widetilde{N})\,, \tag{B.47}$$

where I_C is the first invariant of the right Cauchy-Green deformation tensor. With the free energy function in hand, the second Piola-Kirchhoff stress can be computed through

$$\bar{\mathbf{S}} = 2\frac{\partial \bar{\Psi}}{\partial \bar{\mathbf{C}}} : \frac{\partial \bar{\mathbf{C}}}{\partial \mathbf{C}} \ . \tag{B.48}$$

For the deviatoric part of $\mathbf{S}$, we obtain

$$\bar{\mathbf{S}} = \mu \widetilde{N} \mathbf{1} : \frac{\partial \bar{\mathbf{C}}}{\partial \mathbf{C}} \ , \tag{B.49}$$

which is independent of the deformation. This result indicates that changes to the length of the polymer change due to cross-linking can be modelled through an introduction of an effective cross-link density

$$\mu_{\mathrm{eff}} = \mu \widetilde{N} \ . \tag{B.50}$$

Appendix C

Microsphere model

In the microsphere model, the central notion is to decompose the free energy of the network into two parts; the unencumbered (free) chain and the constrained contribution due to the tube model. The macroscopic free energy can then be written as

$$\bar{\Psi} = \bar{\Psi}_f + \bar{\Psi}_c \,. \tag{C.1}$$

The unit sphere Kirchhoff stress and the tangent operator can be additively decomposed

$$\bar{\boldsymbol{\tau}} = \bar{\boldsymbol{\tau}}_f + \bar{\boldsymbol{\tau}}_c \,, \tag{C.2}$$

$$\bar{\mathbb{C}} = \bar{\mathbb{C}}_f + \bar{\mathbb{C}}_c \,, \tag{C.3}$$

where f denotes the free chain and c represents the constrained chain states. The stress and tangent matrix can be derived from the potential using

$$\boldsymbol{\tau} = 2\frac{\partial \Psi(\boldsymbol{g}, \mathbf{F})}{\partial \boldsymbol{g}} \,, \tag{C.4}$$

$$\mathbb{C} = 4\frac{\partial^2 \Psi(\boldsymbol{g}, \mathbf{F})}{\partial \boldsymbol{g}^2} \,. \tag{C.5}$$

Following the thesis from [Göktepe, 2007], the derivation of the Kirchhoff stress and the material tangent will be provided in the subsequent sections for completeness and provide insights required for adapting the microsphere model for modelling secondary network formation.

C.1   Kirchhoff stress derivation

Consider the stress power additively decomposed into volumetric and deviatoric components

$$\mathcal{P} = \mathcal{P}_{vol} + \mathcal{P}_{dev} \tag{C.6}$$

where the stress power for the volumetric free energy

$$\mathcal{P}_{vol} = \dot{U}(J) = 2\frac{\partial U(J)}{\partial \mathbf{C}} : \frac{1}{2}\dot{\mathbf{C}} \tag{C.7}$$

noting that the time derivative of $\mathbf{C}$ is related to the Lie derivative we can write

$$\mathcal{P}_{vol} = 2\frac{\partial U(J)}{\partial \mathbf{C}} : \mathbf{F}^{\mathrm{T}} \cdot \frac{1}{2}\pounds_{\boldsymbol{v}}\left(\boldsymbol{g}\right) \cdot \mathbf{F} \tag{C.8}$$

and exploiting two successive applications of (A.8) yields

$$\mathcal{P}_{vol} = \mathbf{F} \cdot 2\frac{\partial U(J)}{\partial \mathbf{C}} \cdot \mathbf{F}^{\mathrm{T}} : \frac{1}{2}\pounds_{\boldsymbol{v}}(\boldsymbol{g}) \tag{C.9}$$

Recall that the volumetric part of the second Piola-Kirchhoff is defined as

$$\boldsymbol{S}_{vol} = 2\frac{\partial U(J)}{\partial \mathbf{C}} \tag{C.10}$$

such that the push forward operation on the left hand side of the expression (C.9) results in the volumetric Kirchhoff stress, which is defined as the derivative of the volumetric free energy function with respect to the metric

$$\mathcal{P}_{vol} = 2\frac{\partial U(J)}{\partial \boldsymbol{g}} : \frac{1}{2}\pounds_{\boldsymbol{v}}(\boldsymbol{g}) \tag{C.11}$$

and writing in terms of the chain rule

$$\mathcal{P}_{vol} = 2\frac{\partial U(J)}{\partial \boldsymbol{g}} = 2\frac{\partial U(J)}{\partial J}\frac{\partial J}{\partial \boldsymbol{g}} : \frac{1}{2}\pounds_{\boldsymbol{v}}(\boldsymbol{g}) \ . \tag{C.12}$$

With the Jacobian definition given by [Marsden and Hughes, 1994] as

$$J = \det F_A^a \ \sqrt{\frac{\det g_{ab}}{\det G_{AB}}} \tag{C.13}$$

then we can write the derivative with respect to $\boldsymbol{g}$ as

$$\frac{\partial J}{\partial \boldsymbol{g}} = \det F_A^a \frac{1}{\sqrt{\det G_{AB}}}\frac{\partial\sqrt{\det \boldsymbol{g}}}{\partial \det \boldsymbol{g}}\frac{\partial \det \boldsymbol{g}}{\partial \boldsymbol{g}} \tag{C.14}$$

$$= \frac{1}{2}\det F_A^a \frac{1}{\sqrt{\det G_{AB}}}\frac{\det \boldsymbol{g}}{\sqrt{\det \boldsymbol{g}}} \ \boldsymbol{g}^{-\mathrm{T}} \tag{C.15}$$

$$= \frac{1}{2}\det F_A^a \frac{\sqrt{\det g_{ab}}}{\sqrt{\det G_{AB}}} \ \boldsymbol{g}^{-\mathrm{T}} \tag{C.16}$$

$$= \frac{1}{2}J \ \boldsymbol{g}^{-1} \ . \tag{C.17}$$

With all the required derivatives in hand, the volumetric Kirchhoff stress can be written as

$$\boldsymbol{\tau}_{vol} = 2\frac{\partial U}{\partial J}\frac{\partial J}{\partial \boldsymbol{g}} = p \ \boldsymbol{g}^{-1} \tag{C.18}$$

where we use the definition of pressure $p = U^{'}(J)J$.

With the volumetric strain energy in hand, we turn our attention to the deviatoric contribution to the Kirchhoff stress. Performing a similar analysis for the deviatoric part of the free energy function

$$\bar{\mathcal{P}} = 2\frac{\partial\bar{\psi}}{\partial\bar{\mathbf{C}}} : \frac{1}{2}\dot{\bar{C}} \tag{C.19}$$

$$\bar{\mathcal{P}} = 2\frac{\partial\bar{\psi}}{\partial\bar{\mathbf{C}}} : \frac{1}{2}\bar{\mathbf{F}}^{\mathrm{T}} \cdot \pounds_{\boldsymbol{v}}(\boldsymbol{g}) \cdot \bar{\mathbf{F}} \tag{C.20}$$

and employing the same tricks as for the volumetric part yields

$$\mathcal{P}_{dev} = 2\,\bar{\mathbf{F}} \cdot \frac{\partial \bar{\psi}}{\partial \bar{\mathbf{C}}} \cdot \bar{\mathbf{F}}^{\mathrm{T}} : \frac{1}{2}\bar{\mathcal{L}}_{\boldsymbol{v}}\left(\boldsymbol{g}\right) \tag{C.21}$$

$$= 2\,\frac{\partial \bar{\psi}}{\partial \boldsymbol{g}} : \frac{1}{2}\bar{\mathcal{L}}_{\boldsymbol{v}}\left(\boldsymbol{g}\right) \tag{C.22}$$

$$= \bar{\boldsymbol{\tau}} : \frac{1}{2}\bar{\mathcal{L}}_{\boldsymbol{v}}\left(\boldsymbol{g}\right)\ , \tag{C.23}$$

where the deviatoric Lie derivative $\bar{\mathcal{L}}_{\boldsymbol{v}}\left(\cdot\right)$ is defined as

$$\bar{\mathcal{L}}_{\boldsymbol{v}}\left(\boldsymbol{g}\right) = \mathbf{F}^{-\mathrm{T}} \cdot \frac{\mathrm{D}}{\mathrm{D}t}\left(\bar{\mathbf{F}}^{\mathrm{T}} \cdot \boldsymbol{g} \cdot \bar{\mathbf{F}}\right) \cdot \mathbf{F}^{-1} = \boldsymbol{g} \cdot \bar{\boldsymbol{l}} + \bar{\boldsymbol{l}}^{\mathrm{T}} \cdot \boldsymbol{g} = 2\bar{\mathbf{d}}\ . \tag{C.24}$$

At this point we should also introduce the deviatoric spatial velocity gradient defined as

$$\bar{\boldsymbol{l}} = \dot{\bar{\mathbf{F}}} \cdot \bar{\mathbf{F}}^{-1}\ . \tag{C.25}$$

Now we seek a relationship between the deviatoric spatial velocity gradient and the Lie derivative. We begin with the expression for the deviatoric spatial velocity gradient

$$\boldsymbol{g} \cdot \bar{\boldsymbol{l}} = \boldsymbol{g} \cdot \boldsymbol{l} - \frac{1}{3}\mathrm{tr}\left(\boldsymbol{l}\right)\boldsymbol{g} \tag{C.26}$$

and recall that the spatial velocity gradient is a contravariant second order tensor leading to the formal expression for the trace as

$$\mathrm{tr}\left(\boldsymbol{l}\right) = \boldsymbol{l} : \boldsymbol{g}^{-1}\ . \tag{C.27}$$

Now we can exploit the relationship between the Lie derivative and the rate of deformation in (C.24) coupled with the identity $\mathrm{tr}\left(\mathbf{d}\right) = \mathrm{tr}\left(\boldsymbol{l}\right)$ to obtain

$$\mathrm{tr}\left(\bar{\boldsymbol{l}}\right) = \mathrm{tr}\left(\bar{\mathbf{d}}\right) = \bar{\mathbf{d}} : \boldsymbol{g}^{-1} = \frac{1}{2}\bar{\mathcal{L}}_{\boldsymbol{v}}\left(\boldsymbol{g}\right) : \boldsymbol{g}^{-1}\ . \tag{C.28}$$

Inserting (C.28) into (C.26) returns

$$\boldsymbol{g} \cdot \bar{\boldsymbol{l}} = \boldsymbol{g} \cdot \boldsymbol{l} - \frac{1}{3}\left(\frac{1}{2}\bar{\mathcal{L}}_{\boldsymbol{v}}\left(\boldsymbol{g}\right) : \boldsymbol{g}^{-1}\right)\boldsymbol{g}\ . \tag{C.29}$$

Taking the transpose of (C.29) provides

$$\bar{\boldsymbol{l}}^{\mathrm{T}} \cdot \boldsymbol{g} = \boldsymbol{l}^{\mathrm{T}} \cdot \boldsymbol{g} - \frac{1}{3}\left[\left(\frac{1}{2}\bar{\mathcal{L}}_{\boldsymbol{v}}\left(\boldsymbol{g}\right) : \boldsymbol{g}^{-1}\right) \cdot \boldsymbol{g}\right]^{\mathrm{T}} \tag{C.30}$$

$$= \boldsymbol{l}^{\mathrm{T}} \cdot \boldsymbol{g} - \frac{1}{3}\left(\frac{1}{2}\bar{\mathcal{L}}_{\boldsymbol{v}}\left(\boldsymbol{g}\right) : \boldsymbol{g}^{-1}\right) \cdot \boldsymbol{g}^{\mathrm{T}} \tag{C.31}$$

$$\tag{C.32}$$

and noting that $\boldsymbol{g}^{\mathrm{T}} = \boldsymbol{g}$ by virtue of the definition $g_{ij} = \boldsymbol{g}_i \cdot \boldsymbol{g}_j$. Inserting these intermediate results into (C.24) leads to

$$\bar{\mathcal{L}}_{\boldsymbol{v}}\left(\boldsymbol{g}\right) = \boldsymbol{g}\boldsymbol{l} - \frac{1}{3}\left(\frac{1}{2}\bar{\mathcal{L}}_{\boldsymbol{v}}\left(\boldsymbol{g}\right) : \boldsymbol{g}^{-1}\right)\boldsymbol{g} + \boldsymbol{l}^{\mathrm{T}}\boldsymbol{g} - \frac{1}{3}\left(\frac{1}{2}\bar{\mathcal{L}}_{\boldsymbol{v}}\left(\boldsymbol{g}\right) : \boldsymbol{g}^{-1}\right)\boldsymbol{g} \tag{C.33}$$

$$= \boldsymbol{g}\boldsymbol{l} + \boldsymbol{l}^{\mathrm{T}}\boldsymbol{g} - \frac{1}{3}\left(\bar{\mathcal{L}}_{\boldsymbol{v}}\left(\boldsymbol{g}\right) : \boldsymbol{g}^{-1}\right)\boldsymbol{g} \tag{C.34}$$

$$= \mathcal{L}_{\boldsymbol{v}}\left(\boldsymbol{g}\right) - \frac{1}{3}\left(\bar{\mathcal{L}}_{\boldsymbol{v}}\left(\boldsymbol{g}\right) : \boldsymbol{g}^{-1}\right)\boldsymbol{g} \tag{C.35}$$

With the aid of (A.17) we can write

$$\bar{\mathcal{L}}_v\left(\boldsymbol{g}\right) = \mathcal{L}_v\left(\boldsymbol{g}\right) - \frac{1}{3}\bar{\mathcal{L}}_v\left(\boldsymbol{g}\right) : \boldsymbol{g}^{-1} \otimes \boldsymbol{g} \tag{C.36}$$

and extracting the transpose of the fourth order deviatoric projection tensor gives

$$\bar{\mathcal{L}}_v\left(\boldsymbol{g}\right) = \mathcal{L}_v\left(\boldsymbol{g}\right) : \left(\mathbb{I} - \frac{1}{3}\boldsymbol{g}^{-1} \otimes \boldsymbol{g}\right) \tag{C.37}$$

$$= \mathcal{L}_v\left(\boldsymbol{g}\right) : \mathbb{P}^{\mathrm{T}} \tag{C.38}$$

where $\mathbb{P} = \mathbb{I} - \frac{1}{3}\boldsymbol{g} \otimes \boldsymbol{g}^{-1}$. Now we can obtain an expression for the Kirchhoff stress through (C.23)

$$\mathcal{P}_{dev} = \bar{\boldsymbol{\tau}} : \frac{1}{2}\bar{\mathcal{L}}_v\left(\boldsymbol{g}\right) \tag{C.39}$$

$$= \bar{\boldsymbol{\tau}} : \frac{1}{2}\mathcal{L}_v\left(\boldsymbol{g}\right) : \mathbb{P}^{\mathrm{T}} \tag{C.40}$$

$$= \bar{\boldsymbol{\tau}} : \mathbb{P} : \frac{1}{2}\mathcal{L}_v\left(\boldsymbol{g}\right) \ . \tag{C.41}$$

With the advent of both the volumetric and deviatoric stress powers, we are able to write the Kirchhoff stress as

$$\boldsymbol{\tau} = \tau : \boldsymbol{g}^{-1} + \bar{\boldsymbol{\tau}} : \mathbb{P} = \tau : \boldsymbol{g}^{-1} + \mathbb{P} : \bar{\boldsymbol{\tau}} \tag{C.42}$$

where we exploited the symmetric property of the deviatoric projection tensor.

C.2   Material tangent derivation

Similarly to the Kirchhoff stress derivation, we seek a form

$$\mathcal{L}_v\left(\boldsymbol{\tau}\right) = \mathbb{C} : \frac{1}{2}\mathcal{L}_v\left(\boldsymbol{g}\right) \tag{C.43}$$

and the deviatoric part as related to the Lie derivative

$$\bar{\mathcal{L}}_v\left(\bar{\boldsymbol{\tau}}\right) = \bar{\mathbb{C}} : \frac{1}{2}\bar{\mathcal{L}}_v\left(\boldsymbol{g}\right) \ . \tag{C.44}$$

These definitions will allow us to form an expression based on the Doyle-Erickson formula for the elastic spatial modulus

$$\mathbb{C} = 4\frac{\partial^2 \psi(\boldsymbol{g}, \mathbf{F})}{\partial \boldsymbol{g}\partial \boldsymbol{g}} \tag{C.45}$$

and its deviatoric counterpart

$$\bar{\mathbb{C}} = 4\frac{\partial^2 \bar{\psi}(\boldsymbol{g}, \bar{\mathbf{F}})}{\partial \boldsymbol{g}\partial \boldsymbol{g}} \ . \tag{C.46}$$

Before focusing on the volumetric contribution, we note the following results. The Lie derivative of the Kirchhoff stress is given by

$$\mathcal{L}_v\left(\boldsymbol{\tau}\right) = \dot{\boldsymbol{\tau}} - \boldsymbol{l} \cdot \boldsymbol{\tau} - \boldsymbol{\tau} \cdot \boldsymbol{l}^{\mathrm{T}} \tag{C.47}$$

and analogously the deviatoric part is defined as

$$\bar{\mathcal{L}}_v\left(\bar{\boldsymbol{\tau}}\right) = \dot{\bar{\boldsymbol{\tau}}} - \bar{\boldsymbol{l}} \cdot \bar{\boldsymbol{\tau}} - \bar{\boldsymbol{\tau}} \cdot \bar{\boldsymbol{l}}^{\mathrm{T}} \ . \tag{C.48}$$

C.2.1 Volumetric material tangent

Recalling the expression for $\bar{\tau}$ and taking the Lie derivative (exploiting the proofs below) yields

$$\pounds_{\boldsymbol{v}}\left(p\boldsymbol{g}^{-1}\right) = \dot{p}\boldsymbol{g}^{-1} - p(\boldsymbol{l}\cdot\boldsymbol{g}^{-1} + \boldsymbol{g}^{-1}\cdot\boldsymbol{l}^{\mathrm{T}}) \tag{C.49}$$

$$= (p+\kappa)\boldsymbol{g}^{-1}\otimes\boldsymbol{g}^{-1} : \frac{1}{2}\pounds_{\boldsymbol{v}}\left(\boldsymbol{g}\right) - p\boldsymbol{g}^{-1}\cdot[\pounds_{\boldsymbol{v}}\left(\boldsymbol{g}\right)]\cdot\boldsymbol{g}^{-1} \tag{C.50}$$

$$= \left((p+\kappa)\boldsymbol{g}^{-1}\otimes\boldsymbol{g}^{-1}\right) : \frac{1}{2}\pounds_{\boldsymbol{v}}\left(\boldsymbol{g}\right) - 2p\mathbb{I}_{\boldsymbol{g}^{-1}} : \frac{1}{2}\pounds_{\boldsymbol{v}}\left(\boldsymbol{g}\right) \tag{C.51}$$

$$= \left((p+\kappa)\boldsymbol{g}^{-1}\otimes\boldsymbol{g}^{-1} - 2p\mathbb{I}_{\boldsymbol{g}^{-1}}\right) : \frac{1}{2}\pounds_{\boldsymbol{v}}\left(\boldsymbol{g}\right) \ , \tag{C.52}$$

where $\mathbb{I}_{\boldsymbol{g}^{-1}}$ satisfies

$$p\boldsymbol{g}^{-1}\pounds_{\boldsymbol{v}}\left(\boldsymbol{g}\right)\boldsymbol{g}^{-1} = 2p\mathbb{I}_{\boldsymbol{g}^{-1}} : \frac{1}{2}\pounds_{\boldsymbol{v}}\left(\boldsymbol{g}\right) \ . \tag{C.53}$$

For completeness some key derivatives are derived below.

Proof. Differentiate $\dot{J}$ with respect to the metric.
Consider the time derivative of the Jacobian

$$\dot{J} = \frac{\partial J}{\partial t} = \frac{\partial J}{\partial \boldsymbol{g}} : \frac{\partial \boldsymbol{g}}{\partial t} \ . \tag{C.54}$$

Recall the previous result

$$\frac{\partial J}{\partial \boldsymbol{g}} = \frac{1}{2}J\boldsymbol{g}^{-1} \tag{C.55}$$

and substitution of this expression, coupled with the Lie derivative of the metric tensor yields

$$\frac{\partial J}{\partial t} = J\boldsymbol{g}^{-1} : \frac{1}{2}\pounds_{\boldsymbol{v}}\left(\boldsymbol{g}\right) \ . \tag{C.56}$$

$\square$

Proof. Differentiation of $\dot{p}\boldsymbol{g}^{-1}$ as a function of time.

Consider the time derivative of the pressure $p = JU'$ through the chain rule

$$\dot{p}\boldsymbol{g}^{-1} = \dot{J}U' + JU''\dot{J} . \tag{C.57}$$

Exploiting the previous results leads to

$$\dot{p}\boldsymbol{g}^{-1} = JU'\boldsymbol{g}^{-1} \otimes \boldsymbol{g}^{-1} : \frac{1}{2}\pounds_v(\boldsymbol{g}) + JU''J\boldsymbol{g}^{-1} \otimes \boldsymbol{g}^{-1} : \frac{1}{2}\pounds_v(\boldsymbol{g}) \tag{C.58}$$

$$= (p + \kappa)\boldsymbol{g}^{-1} \otimes \boldsymbol{g}^{-1} : \frac{1}{2}\pounds_v(\boldsymbol{g}) \tag{C.59}$$

with the definitions as before

$$p = JU' \tag{C.60}$$

$$\kappa = J^2 U'' \tag{C.61}$$

$\square$

C.2.2 Deviatoric material tangent

With the expression for the volumetric material tangent complete, we turn our attention to the deviatoric material tangent. We start with the term

$$\pounds_v(\bar{\boldsymbol{\tau}} : \mathbb{P}) = \pounds_v(\bar{\boldsymbol{\tau}}) : \mathbb{P} + \bar{\boldsymbol{\tau}} : \pounds_v(\mathbb{P}) , \tag{C.62}$$

and the definition for the Lie derivative of the deviatoric Kirchhoff stress

$$\pounds_v(\bar{\boldsymbol{\tau}}) = \dot{\bar{\boldsymbol{\tau}}} - \boldsymbol{l} \cdot \bar{\boldsymbol{\tau}} - \bar{\boldsymbol{\tau}} \cdot \boldsymbol{l}^{\mathrm{T}} . \tag{C.63}$$

Rearranging and inserting (C.48) into $\dot{\bar{\boldsymbol{\tau}}}$ from (C.63) gives

$$\pounds_v(\bar{\boldsymbol{\tau}}) = [\bar{\pounds}_v(\bar{\boldsymbol{\tau}}) + \bar{\boldsymbol{l}} \cdot \bar{\boldsymbol{\tau}} + \bar{\boldsymbol{\tau}} \cdot \bar{\boldsymbol{l}}^{\mathrm{T}}] - \boldsymbol{l} \cdot \bar{\boldsymbol{\tau}} - \bar{\boldsymbol{\tau}} \cdot \boldsymbol{l}^{\mathrm{T}} \tag{C.64}$$

$$= \bar{\pounds}_v(\bar{\boldsymbol{\tau}}) + (\bar{\boldsymbol{l}} - \boldsymbol{l}) \cdot \bar{\boldsymbol{\tau}} + \bar{\boldsymbol{\tau}} \cdot (\bar{\boldsymbol{l}}^{\mathrm{T}} - \boldsymbol{l}^{\mathrm{T}}) . \tag{C.65}$$

Now we require an expression for $\bar{\boldsymbol{l}} - \boldsymbol{l}$, which we can glean from the definition of the deviatoric velocity gradient (C.26)

$$\bar{\boldsymbol{l}} - \boldsymbol{l} = \boldsymbol{g}^{-1} \cdot \boldsymbol{g} \cdot \boldsymbol{l} - \frac{1}{3}\mathrm{tr}(\boldsymbol{l})\boldsymbol{g}^{-1} \cdot \boldsymbol{g} - \boldsymbol{l} \tag{C.66}$$

$$= -\frac{1}{3}\mathrm{tr}(\boldsymbol{l})\mathbf{1} \tag{C.67}$$

$$= -\frac{1}{3}\left[\frac{1}{2}\pounds_v(\boldsymbol{g}) : \boldsymbol{g}^{-1}\right]\mathbf{1} \tag{C.68}$$

and a straightforward transpose operation returns

$$\bar{\boldsymbol{l}}^{\mathrm{T}} - \boldsymbol{l}^{\mathrm{T}} = -\frac{1}{3}\left[\frac{1}{2}\pounds_v(\boldsymbol{g}) : \boldsymbol{g}^{-1}\right]\mathbf{1} . \tag{C.69}$$

Inserting expressions (C.68) and (C.69) into (C.65) provides

$$\pounds_v\left(\bar{\boldsymbol{\tau}}\right) = \bar{\pounds}_v\left(\bar{\boldsymbol{\tau}}\right) - \left(\frac{1}{3}\left[\frac{1}{2}\pounds_v\left(\boldsymbol{g}\right):\boldsymbol{g}^{-1}\right]\right)\bar{\boldsymbol{\tau}} - \bar{\boldsymbol{\tau}}\left(\frac{1}{3}\left[\frac{1}{2}\pounds_v\left(\boldsymbol{g}\right):\boldsymbol{g}^{-1}\right]\right) . \tag{C.70}$$

Using (A.17) where $\boldsymbol{A} = 1/2\pounds_v\left(\boldsymbol{g}\right)$, $\boldsymbol{B} = \boldsymbol{g}^{-1}$ and $\boldsymbol{C} = \bar{\boldsymbol{\tau}}$, allows the Lie derivative of the metric to be written on the right hand side

$$\pounds_v\left(\bar{\boldsymbol{\tau}}\right) = \bar{\pounds}_v\left(\bar{\boldsymbol{\tau}}\right) - \frac{2}{3}\left(\frac{1}{2}\pounds_v\left(\boldsymbol{g}\right):\boldsymbol{g}^{-1}\right)\bar{\boldsymbol{\tau}} \tag{C.71}$$

$$= \bar{\pounds}_v\left(\bar{\boldsymbol{\tau}}\right) - \frac{2}{3}\left[\frac{1}{2}\pounds_v\left(\boldsymbol{g}\right):\left(\boldsymbol{g}^{-1}\otimes\bar{\boldsymbol{\tau}}\right)\right] \tag{C.72}$$

$$= \bar{\pounds}_v\left(\bar{\boldsymbol{\tau}}\right) - \frac{2}{3}(\boldsymbol{g}^{-1}\otimes\bar{\boldsymbol{\tau}}):\frac{1}{2}\pounds_v\left(\boldsymbol{g}\right) \tag{C.73}$$

$$= \bar{\pounds}_v\left(\bar{\boldsymbol{\tau}}\right) - \frac{2}{3}\left(\bar{\boldsymbol{\tau}}\otimes\boldsymbol{g}^{-1}\right):\frac{1}{2}\pounds_v\left(\boldsymbol{g}\right) \tag{C.74}$$

and exploiting (C.38) and (C.44) provides

$$\pounds_v\left(\bar{\boldsymbol{\tau}}\right) = \bar{\mathbb{C}}:\frac{1}{2}\bar{\pounds}_v\left(\boldsymbol{g}\right) - \frac{2}{3}\left(\bar{\boldsymbol{\tau}}\otimes\boldsymbol{g}^{-1}\right):\frac{1}{2}\pounds_v\left(\boldsymbol{g}\right) \tag{C.75}$$

$$= \left(\bar{\mathbb{C}}:\mathbb{P} - \frac{2}{3}\left(\bar{\boldsymbol{\tau}}\otimes\boldsymbol{g}^{-1}\right)\right):\frac{1}{2}\pounds_v\left(\boldsymbol{g}\right) , \tag{C.76}$$

where we used (C.38) and the transpose identity to obtain the Lie derivative on the right hand side. We can now complete the expression in (C.62) to obtain

$$\pounds_v\left(\bar{\boldsymbol{\tau}}\right):\mathbb{P} = \left(\bar{\mathbb{C}}:\mathbb{P} - \frac{2}{3}\left(\bar{\boldsymbol{\tau}}\otimes\boldsymbol{g}^{-1}\right)\right):\frac{1}{2}\pounds_v\left(\boldsymbol{g}\right):\mathbb{P} \tag{C.77}$$

$$= \mathbb{P}^{\mathrm{T}}:\left(\bar{\mathbb{C}}:\mathbb{P} - \frac{2}{3}\left(\bar{\boldsymbol{\tau}}\otimes\boldsymbol{g}^{-1}\right)\right):\frac{1}{2}\pounds_v\left(\boldsymbol{g}\right) \tag{C.78}$$

$$= \left(\mathbb{P}^{\mathrm{T}}:\bar{\mathbb{C}}:\mathbb{P} - \frac{2}{3}\left(\mathbb{P}^{\mathrm{T}}:\bar{\boldsymbol{\tau}}\otimes\boldsymbol{g}^{-1}\right)\right):\frac{1}{2}\pounds_v\left(\boldsymbol{g}\right) . \tag{C.79}$$

With the following result in hand, we require the second expression in (C.62) to complete the isochoric view of the constitutive model

$$\pounds_v\left(\mathbb{P}\right) = -\frac{1}{3}\left[\pounds_v\left(\boldsymbol{g}\right)\otimes\boldsymbol{g}^{-1} + \boldsymbol{g}\otimes\pounds_v\left(\boldsymbol{g}^{-1}\right)\right] , \tag{C.80}$$

where the result required to simplify (C.80) is given by (C.82).

Proof. Show that $\mathcal{L}_v\left(g^{-1}\right) = -g^{-1} \cdot \mathcal{L}_v\left(g\right) \cdot g^{-1}$

Consider the Lie derivative of the covariant metric

$$\mathcal{L}_v\left(g\right) = \mathbf{F}^{-\mathrm{T}} \cdot \frac{\mathrm{d}}{\mathrm{d}t}(\mathbf{F}^{\mathrm{T}} \cdot g \cdot \mathbf{F}) \cdot \mathbf{F}^{-1} \tag{C.81}$$

and the Lie derivative of the contravariant metric

$$\mathcal{L}_v\left(g^{-1}\right) = \mathbf{F} \cdot \frac{\mathrm{d}}{\mathrm{d}t} \cdot (\mathbf{F}^{-1} \cdot g \cdot \mathbf{F}^{-\mathrm{T}}) \cdot \mathbf{F}^{\mathrm{T}} \ . \tag{C.82}$$

Recalling the identity for the deformation gradient

$$\frac{\mathrm{d}(\mathbf{F} \cdot \mathbf{F}^{-1})}{\mathrm{d}t} = 0 \tag{C.83}$$

leads to an alternative expression involving the velocity gradient $l = \dot{\mathbf{F}} \cdot \mathbf{F}^{-1}$

$$\dot{\mathbf{F}}^{-1} = -\mathbf{F}^{-1} \cdot \dot{\mathbf{F}} \cdot \mathbf{F}^{-1} = -\mathbf{F}^{-1} \cdot l \tag{C.84}$$

Expanding the expressions for the Lie derivatives result in several terms. It is a straightforward exercise in matrix algebra to rearrange terms in (C.82) using (C.84) to obtain

$$\mathcal{L}_v\left(g\right) = -g \cdot \mathcal{L}_v\left(g^{-1}\right) \cdot g \ . \tag{C.85}$$

$\square$

After simplifying we obtain

$$\mathcal{L}_v\left(\mathbb{P}\right) = -\frac{1}{3}\left[\mathcal{L}_v\left(g\right) \otimes g^{-1} - g \otimes g^{-1}(\mathcal{L}_v\left(g\right))g^{-1}\right] \tag{C.86}$$

which through (C.53) yields

$$\mathcal{L}_v\left(\mathbb{P}\right) = -\frac{1}{3}\left[\mathcal{L}_v\left(g\right) \otimes g^{-1} - g \otimes g^{-1}(\mathcal{L}_v\left(g\right))g^{-1}\right] \tag{C.87}$$

$$\bar{\tau} : \mathcal{L}_v\left(\mathbb{P}\right) = -\frac{1}{3}\left[\bar{\tau} : \mathcal{L}_v\left(g\right) \otimes g^{-1} - \bar{\tau} : g \otimes g^{-1}(\mathcal{L}_v\left(g\right))g^{-1}\right] \ . \tag{C.88}$$

Successive applications of (A.16) and (A.17) to the first term and one application of (A.17) to the second term furnishes

$$\tau : \mathcal{L}_v\left(\mathbb{P}\right) = -\frac{1}{3}\left[\bar{\tau} : \mathcal{L}_v\left(g\right) \otimes g^{-1} - \bar{\tau} : g \otimes (\mathbb{I}_{g^{-1}} : \mathcal{L}_v\left(g\right))\right] \tag{C.89}$$

$$= -\frac{1}{3}\left[g^{-1} \otimes \bar{\tau} : \mathcal{L}_v\left(g\right) - (\bar{\tau} : g)\mathbb{I}_{g^{-1}} : \mathcal{L}_v\left(g\right)\right] \tag{C.90}$$

$$= -\frac{2}{3}\left[g^{-1} \otimes \bar{\tau} - (\bar{\tau} : g)\mathbb{I}_{g^{-1}}\right] : \frac{1}{2}\mathcal{L}_v\left(g\right) \ . \tag{C.91}$$

At this stage, it is important to note that introducing the fourth order projection tensor would be advantageous for merging these results with the volumetric contribution and the first term in the deviatoric contribution of the material tangent. To this end, it is useful to recall the definition of the projection tensor

$$\mathbb{P} = \mathbb{I} - \frac{1}{3}g \otimes g^{-1} \ . \tag{C.92}$$

Simple rearrangement of (C.91) yields

$$\boldsymbol{\tau} : \mathcal{L}_{\boldsymbol{v}}\left(\mathbb{P}\right) = -\frac{2}{3}\left[\boldsymbol{g}^{-1} \otimes \bar{\boldsymbol{\tau}} : \mathbb{P} + \frac{1}{3}(\boldsymbol{g}^{-1} \otimes \bar{\boldsymbol{\tau}}) : (\boldsymbol{g} \otimes \boldsymbol{g}^{-1}) - (\bar{\boldsymbol{\tau}} : \boldsymbol{g})\mathbb{I}_{\boldsymbol{g}^{-1}}\right] : \frac{1}{2}\mathcal{L}_{\boldsymbol{v}}\left(\boldsymbol{g}\right) . \qquad \text{(C.93)}$$

Applying (A.18) on (C.93) with $A = \boldsymbol{g}^{-1}$, $B = \bar{\boldsymbol{\tau}}$, $C = \boldsymbol{g}$ and $D = \boldsymbol{g}^{-1}$ and collecting terms provides

$$\boldsymbol{\tau} : \mathcal{L}_{\boldsymbol{v}}\left(\mathbb{P}\right) = -\frac{2}{3}\left[\boldsymbol{g}^{-1} \otimes \bar{\boldsymbol{\tau}} : \mathbb{P} + \frac{1}{3}(\bar{\boldsymbol{\tau}} : \boldsymbol{g})(\boldsymbol{g}^{-1} \otimes \boldsymbol{g}^{-1}) - (\bar{\boldsymbol{\tau}} : \boldsymbol{g})\mathbb{I}_{\boldsymbol{g}^{-1}}\right] : \frac{1}{2}\mathcal{L}_{\boldsymbol{v}}\left(\boldsymbol{g}\right) \qquad \text{(C.94)}$$

$$= -\frac{2}{3}\left[\boldsymbol{g}^{-1} \otimes \bar{\boldsymbol{\tau}} : \mathbb{P} - (\bar{\boldsymbol{\tau}} : \boldsymbol{g})\left(\mathbb{I}_{\boldsymbol{g}^{-1}} - \frac{1}{3}\boldsymbol{g}^{-1} \otimes \boldsymbol{g}^{-1}\right)\right] : \frac{1}{2}\mathcal{L}_{\boldsymbol{v}}\left(\boldsymbol{g}\right) . \qquad \text{(C.95)}$$

Defining $\mathbb{P}_{\boldsymbol{g}^{-1}} = \mathbb{I}_{\boldsymbol{g}^{-1}} - \frac{1}{3}\boldsymbol{g}^{-1} \otimes \boldsymbol{g}^{-1}$ allows simplification of (C.95) leading to

$$\boldsymbol{\tau} : \mathcal{L}_{\boldsymbol{v}}\left(\mathbb{P}\right) = -\frac{2}{3}\left[\boldsymbol{g}^{-1} \otimes \bar{\boldsymbol{\tau}} : \mathbb{P} - (\bar{\boldsymbol{\tau}} : \boldsymbol{g})\mathbb{P}_{\boldsymbol{g}^{-1}}\right] : \frac{1}{2}\mathcal{L}_{\boldsymbol{v}}\left(\boldsymbol{g}\right) . \qquad \text{(C.96)}$$

Finally we can substitute (C.96) into (C.79) to obtain the deviatoric part of the material tangent

$$\mathcal{L}_{\boldsymbol{v}}\left(\bar{\boldsymbol{\tau}} : \mathbb{P}\right) = \left[\mathbb{P}^{\mathrm{T}} : \left(\bar{\mathbb{C}} + \frac{2}{3}(\bar{\boldsymbol{\tau}} : \boldsymbol{g})\mathbb{I}_{\boldsymbol{g}^{-1}}\right) : \mathbb{P} - \frac{2}{3}(\mathbb{P}^{\mathrm{T}} : \bar{\boldsymbol{\tau}} \otimes \boldsymbol{g}^{-1} + \boldsymbol{g}^{-1} \otimes \bar{\boldsymbol{\tau}} : \mathbb{P})\right] : \frac{1}{2}\mathcal{L}_{\boldsymbol{v}}\left(\boldsymbol{g}\right) \qquad \text{(C.97)}$$

and combining the deviatoric part with the volumetric part yields

$$\mathbb{C} = (p + \kappa)\boldsymbol{g}^{-1} \otimes \boldsymbol{g}^{-1} - 2p\mathbb{I}_{\boldsymbol{g}^{-1}} + \left[\mathbb{P}^{\mathrm{T}} : \left(\bar{\mathbb{C}} + \frac{2}{3}(\bar{\boldsymbol{\tau}} : \boldsymbol{g})\mathbb{I}_{\boldsymbol{g}^{-1}}\right) : \mathbb{P} - \frac{2}{3}(\mathbb{P}^{\mathrm{T}} : \bar{\boldsymbol{\tau}} \otimes \boldsymbol{g}^{-1} + \boldsymbol{g}^{-1} \otimes \bar{\boldsymbol{\tau}} : \mathbb{P})\right] .$$
$$\text{(C.98)}$$

C.3   Analysis of unit sphere numerical integration

Considerable debate and scepticism surrounds the use of numerical integration over unit spheres in elastomer models despite the fact that the microsphere model has shown its ability to be a versatile tool for constitutive modelling of elastomers [Ehret et al., 2010]. In order to further understand the role of numerical integration on the accuracy and the induced anisotropy of the homogenisation, a series of numerical experiments will be performed. Since the integration method is characterised by the degree of the operand, both Gaussian and non-Gaussian affine microsphere models will be examined under basic deformation modes. These three deformation modes will be tested; uniaxial, equibiaxial and shear, characterised by the stretch λ, resulting in the following deformation gradients

$$\mathbf{F}_{\text{uniaxial}} = \begin{bmatrix} \lambda & 0 & 0 \\ 0 & 1/\sqrt{\lambda} & 0 \\ 0 & 0 & 1/\sqrt{\lambda} \end{bmatrix} , \qquad \text{(C.99)}$$

$$\mathbf{F}_{\text{equibiaxial}} = \begin{bmatrix} \lambda & 0 & 0 \\ 0 & \lambda & 0 \\ 0 & 0 & 1/\lambda^2 \end{bmatrix} \qquad \text{(C.100)}$$

and

$$\mathbf{F}_{\text{shear}} = \begin{bmatrix} 1 & 0 & \lambda \\ 0 & 1 & 0 \\ 0 & 0 & 1 \end{bmatrix} , \qquad \text{(C.101)}$$
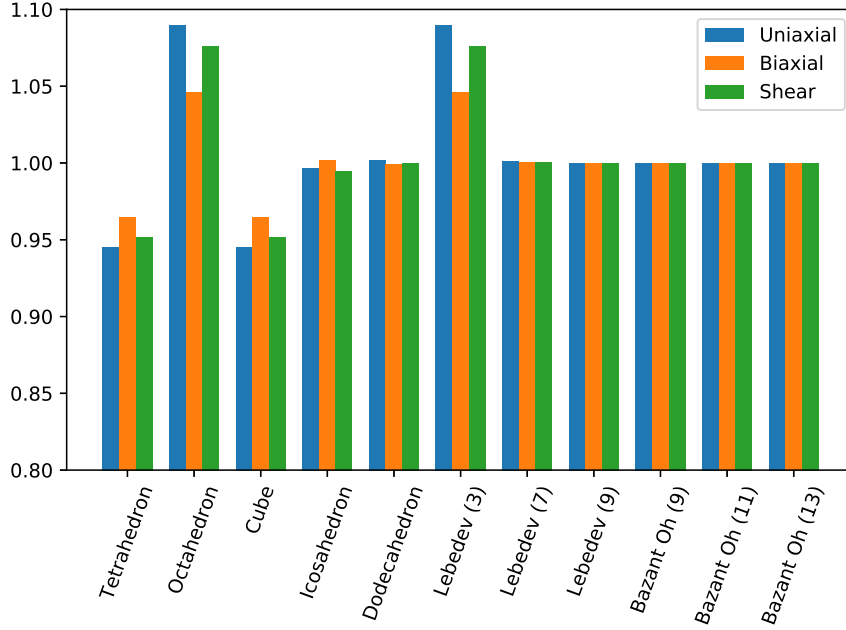
Figure C.1: Integration error normalised to the thirteenth order Bažant and Oh integration scheme

respectively. The deviatoric Kirchhoff stress of the affine Gaussian and non-Gaussian microsphere stress are given by

$$\bar{\boldsymbol{\tau}} = 3\mu \langle \boldsymbol{t} \otimes \boldsymbol{t} \rangle \tag{C.102}$$

and

$$\bar{\boldsymbol{\tau}} = \mu \left\langle \frac{3N - \lambda^2}{N - \lambda^2} \boldsymbol{t} \otimes \boldsymbol{t} \right\rangle , \tag{C.103}$$

respectively, where the deformed tangent is represented by $\boldsymbol{t} = \mathbf{F} \cdot \boldsymbol{r}$ and $\boldsymbol{r}$ is the integration direction to the surface of the unit sphere. The non-Gaussian model is introduced to provide a source of complexity in the integration. The von Mises stress is computed for a rotated coordinate system and the error with the original configuration is visualised to highlight the degree of anisotropy induced by the integration scheme. Numerical integration error was seen to increase for larger stretches, therefore the nominal stretch was taken as $\lambda = 5$.

Typically a 21 point[1] symmetric quadrature scheme is used for the evaluation of the stress and material tangent operator, for example [Bažant and Oh, 1986]. A comparison of several quadrature schemes available in the open source Python package `Quadpy` was performed [Schlömer, 2018]. These included lower order schemes suitable for the efficient computation of stress and material tangent operators, including platonic, Lebedev and Bažant and Oh schemes, see [Hesse et al., 2015, Lebedev, 1976, Bažant and Oh, 1986]. For evaluating the relative error between schemes, the von Mises stress is computed and normalised against the thirteenth order Bažant and Oh scheme, see Figure C.1.

Inspection of Figure C.1 demonstrates the inadequacy of platonic type integration schemes compared to Lebedev and Bažant and Oh schemes. Minor differences occur in the loading conditions for lower order

---

[1]The selection of this integration scheme is the source of the erroneous and misleading moniker *21 chain model* for the microsphere model, see for example [Hossain, 2010]. It is emphasised that the quadrature scheme has nothing to do with number of chains in the unit sphere. It is merely a tool to numerically evaluate a continuous integral.

schemes but the accuracy remains sufficient. Performing analysis of higher order schemes reveals differences in the sixth decimal place occur, which could be significant depending on the tolerances used in the Newton-Raphson procedure. Further analysis is required to understand if these differences are simply numerical round off error or if additional accuracy is indeed required.

For the special case where affine Gaussian chain theory is used, the dependence on the sphere integration scheme is removed and the resulting choice of integration scheme is not important, see Figure C.2, where floating point error is the cause of any anisotropy or inaccuracy across several integration schemes and no relationship between the error and the stretch or deformation mode is observed.

The accuracy of the schemes is not the only consideration in the selection of a suitable integration scheme. Pollution of the solution through induced anisotropy is also a concern. To understand the influence of the quadrature scheme on this property, Figures C.4, C.6 and C.8 show the induced anisotropy of the platonic schemes and Figures C.5, C.7 and C.9 show the induced anisotropy for the Lebedev and Bažant and Oh schemes for the uniaxial, biaxial and shear loading respectively. These figures were produced by rotating the integration points and computing the percentage error between the rotated von Mises stress and the unrotated von Mises stress.

Isotropy is destroyed when using the platonic schemes and low order Lebedev schemes and it is therefore recommended to avoid these schemes. Lebedev schemes of reasonable accuracy introduce a level of anisotropy in the order of 0.008% for equibiaxial loading, with the least anisotropy induced by the thirteenth order Bažant and Oh scheme. Similar results are observed in the uniaxial case. However, under shear loading the higher order schemes may influence the result more than the lower order schemes. This is counter-intuitive and indicates that some level problem specific testing is required. Note that for higher order schemes the error introduced relative to the unrotated sphere is less than 1% and is negligible compared to uncertainties in material properties.

(a) Tetrahedron scheme

(b) Octahedron scheme

(c) Cube scheme

(d) Icosahedron scheme

(e) Dodecahedron scheme
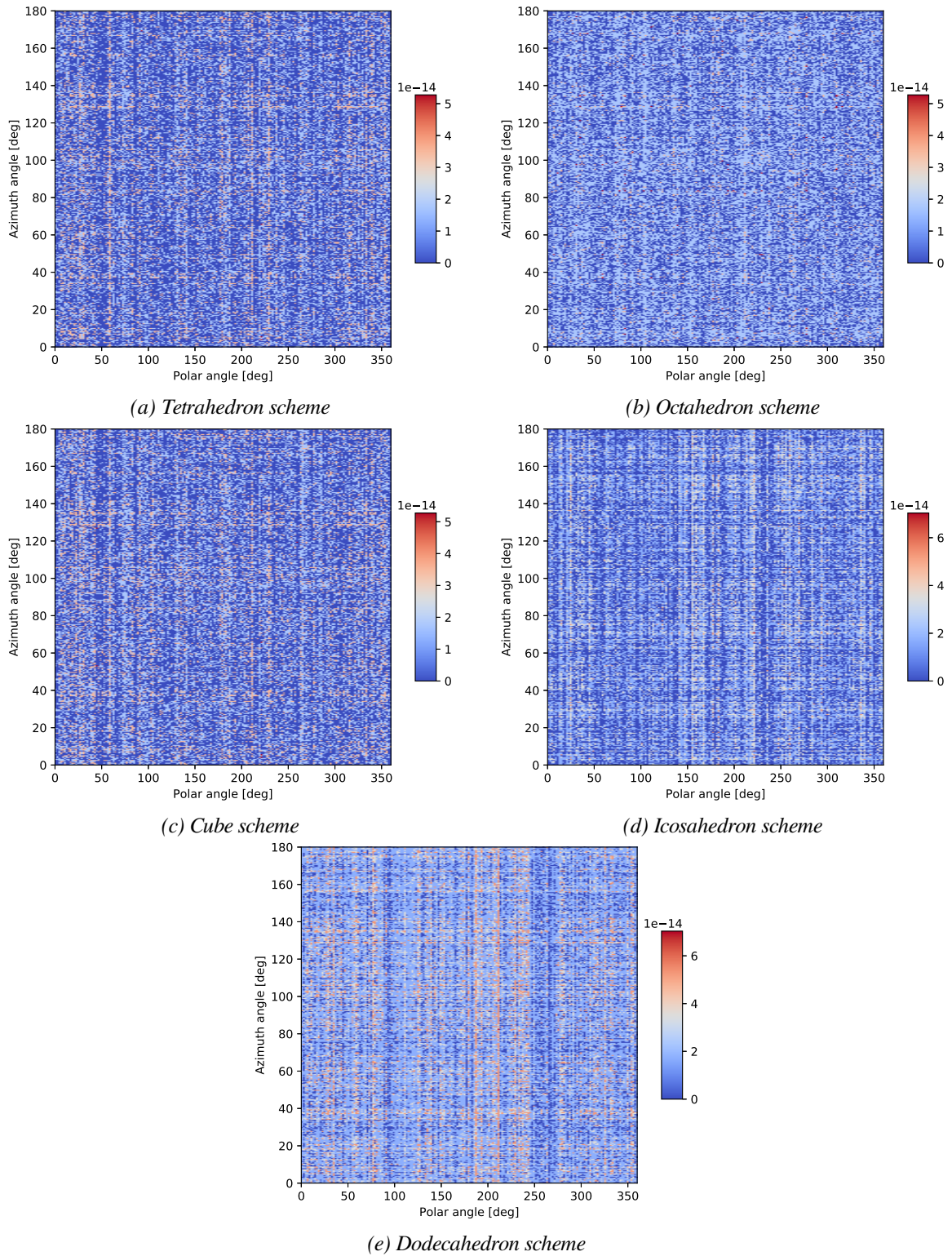
Figure C.2: Percentage error of the platonic integration schemes with respect to the reference solution under rotational transformations and biaxial loading ($\lambda = 5$) for affine Gaussian model

(a) Lebedev 3rd order

(b) Lebedev 7th order

(c) Lebedev 9th order

(d) Bažant and Oh 9th order

(e) Bažant and Oh 11th order

(f) Bažant and Oh 13th order
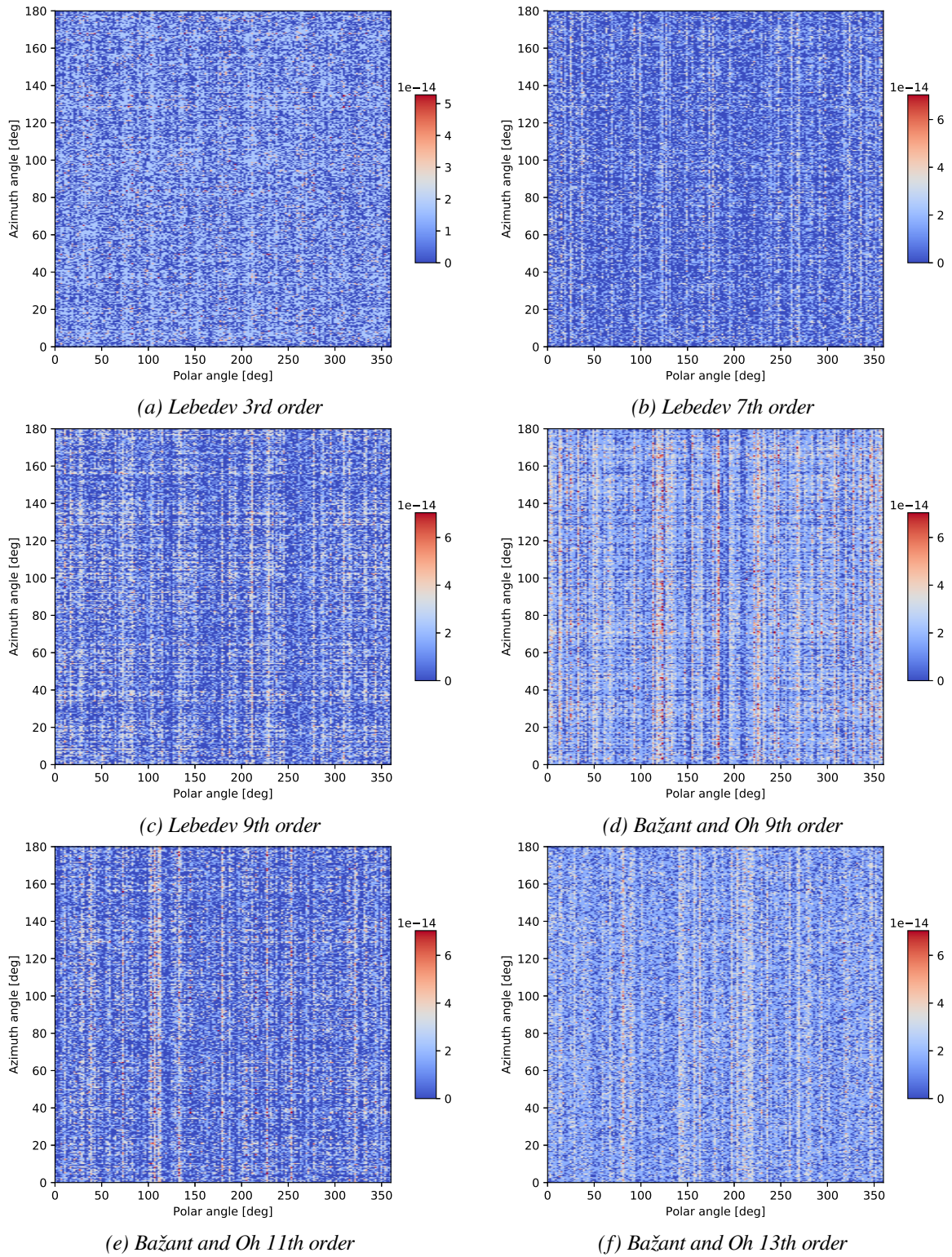
Figure C.3: Percentage error of integration schemes with respect to the reference solution under rotational transformations and biaxial loading ($\lambda = 5$) for affine Gaussian model

(a) Tetrahedron scheme

(b) Octahedron scheme

(c) Cube scheme

(d) Icosahedron scheme

(e) Dodecahedron scheme
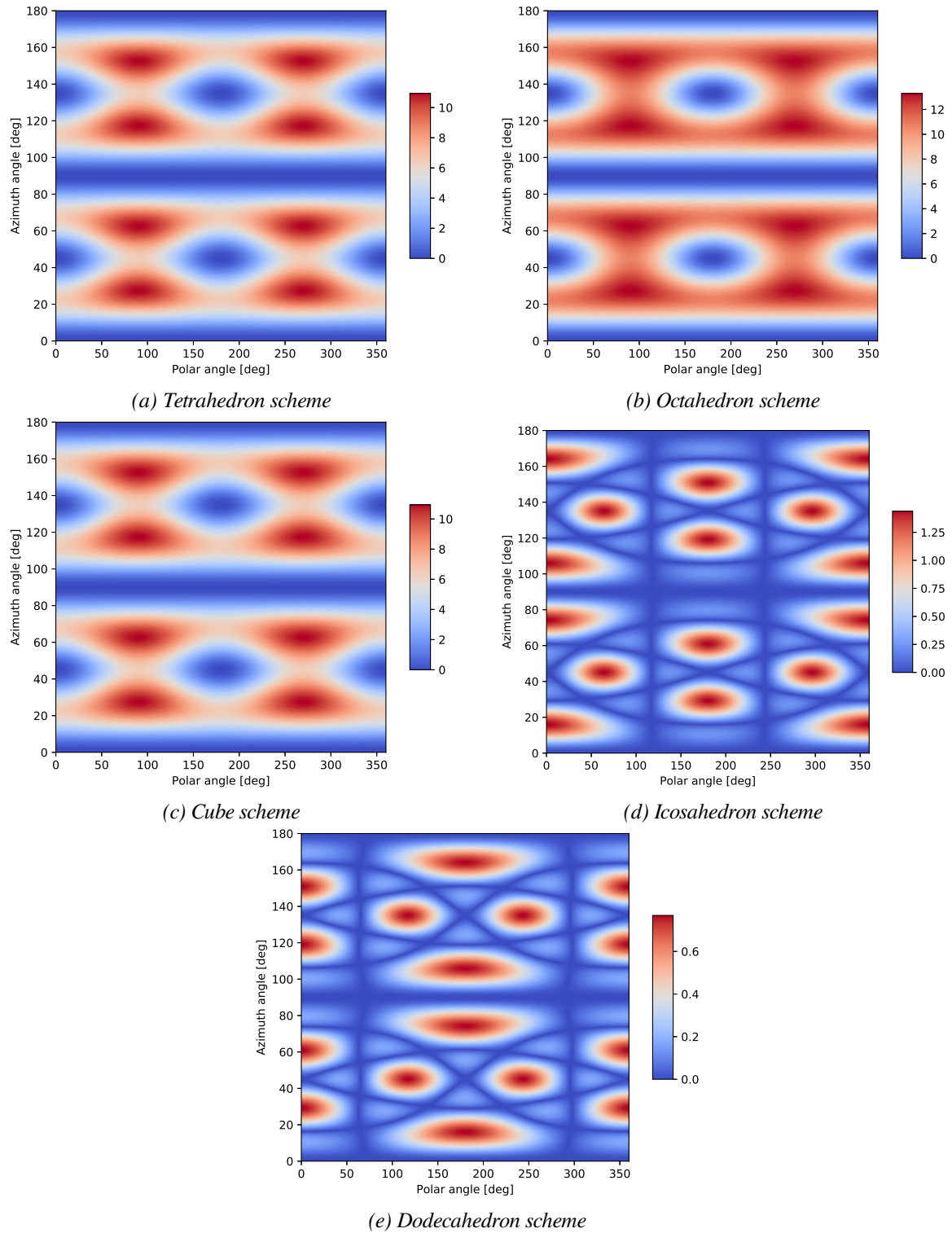
Figure C.4: Percentage error of the platonic integration schemes with respect to the reference solution under rotational transformations and uniaxial loading ($\lambda = 5$) for affine non-Gaussian model

(a) Lebedev 3rd order

(b) Lebedev 7th order

(c) Lebedev 9th order

(d) Bažant and Oh 9th order

(e) Bažant and Oh 11th order

(f) Bažant and Oh 13th order
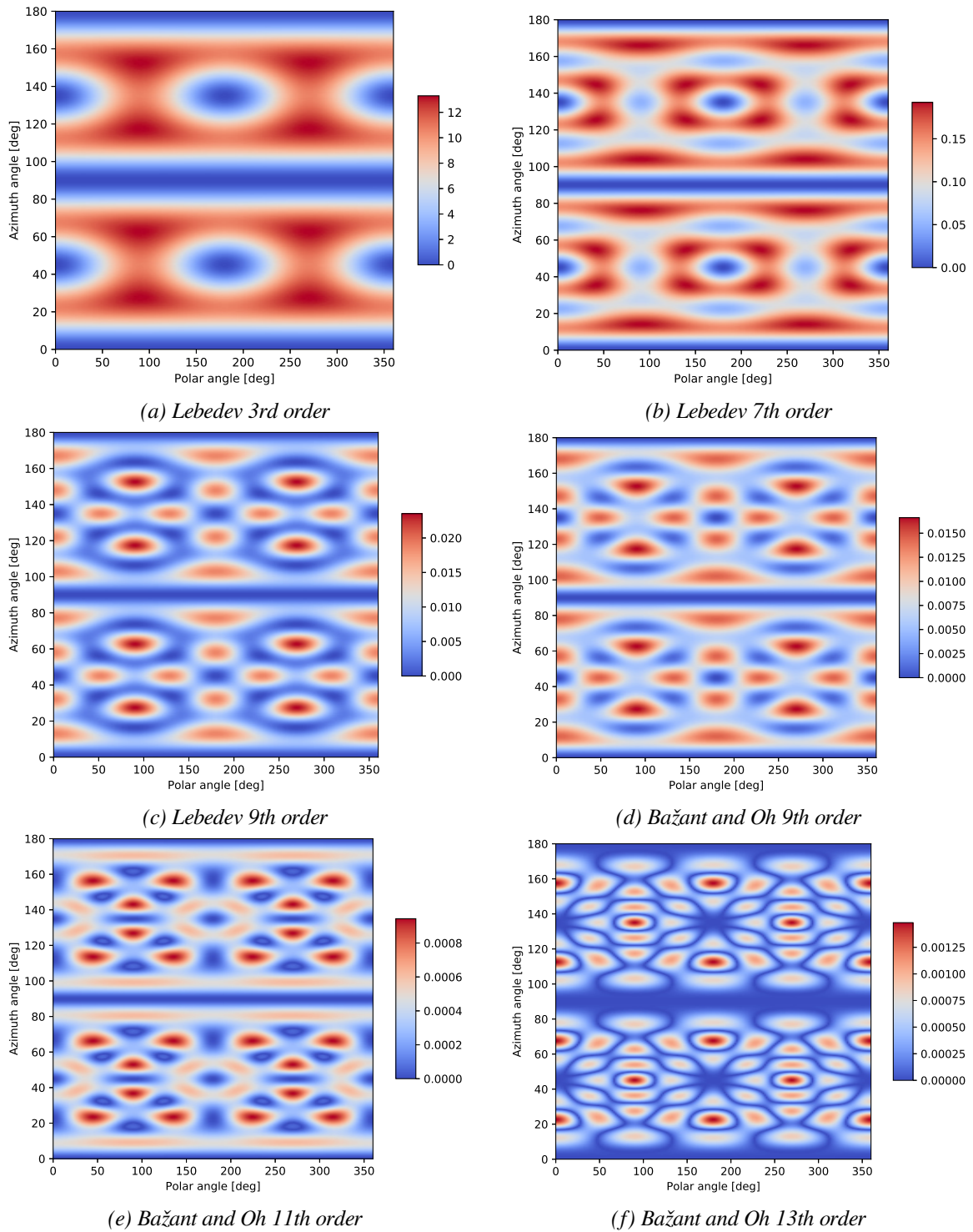
Figure C.5: Percentage error of integration schemes with respect to the reference solution under rotational transformations and uniaxial loading to $\lambda = 5$

(a) Tetrahedron scheme

(b) Octahedron scheme

(c) Cube scheme

(d) Icosahedron scheme

(e) Dodecahedron scheme
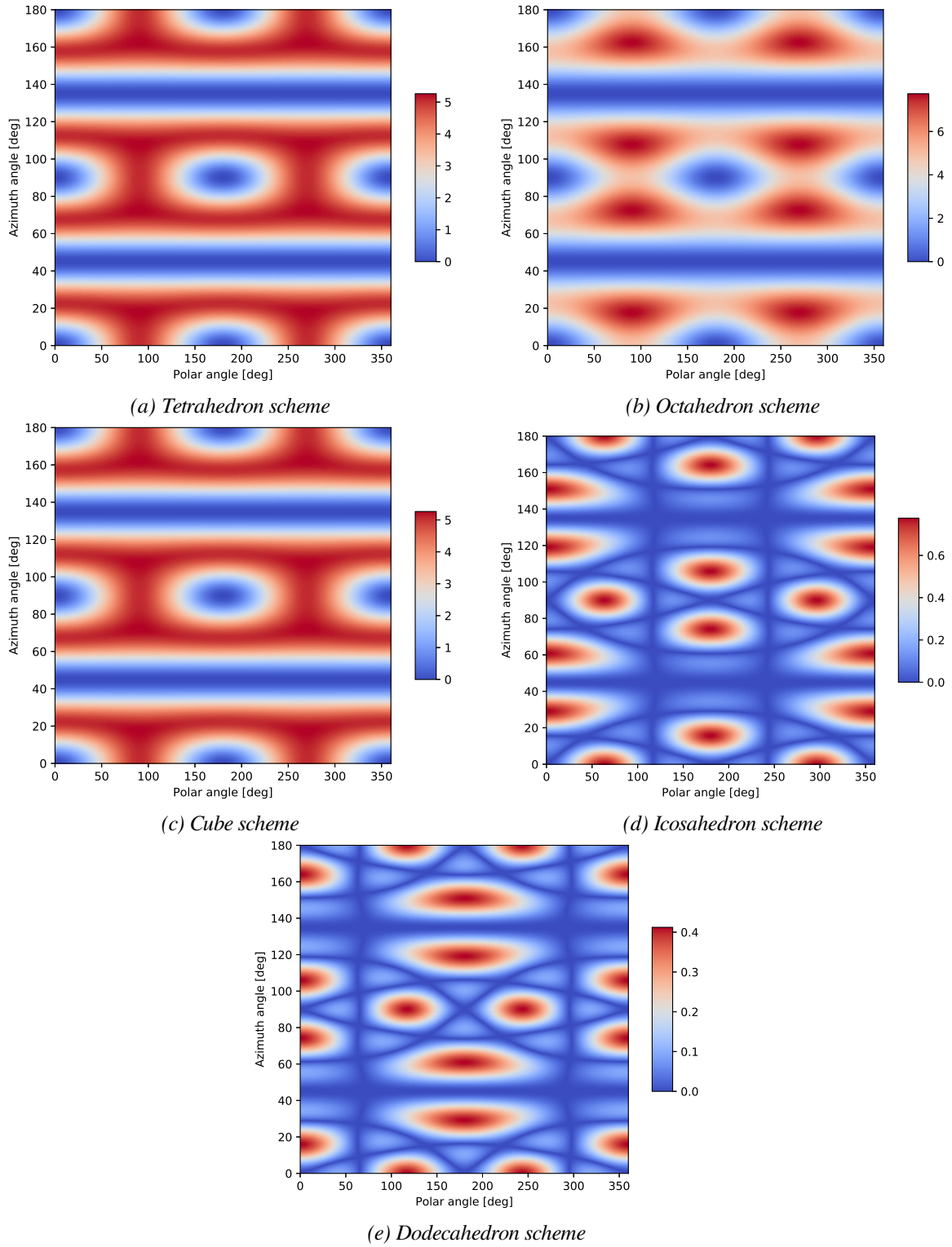
Figure C.6: Percentage error of the platonic integration schemes with respect to the reference solution under rotational transformations and equibiaxial loading to $\lambda = 5$

(a) Lebedev 3rd order

(b) Lebedev 7th order

(c) Lebedev 9th order

(d) Bažant and Oh 9th order

(e) Bažant and Oh 11th order

(f) Bažant and Oh 13th order
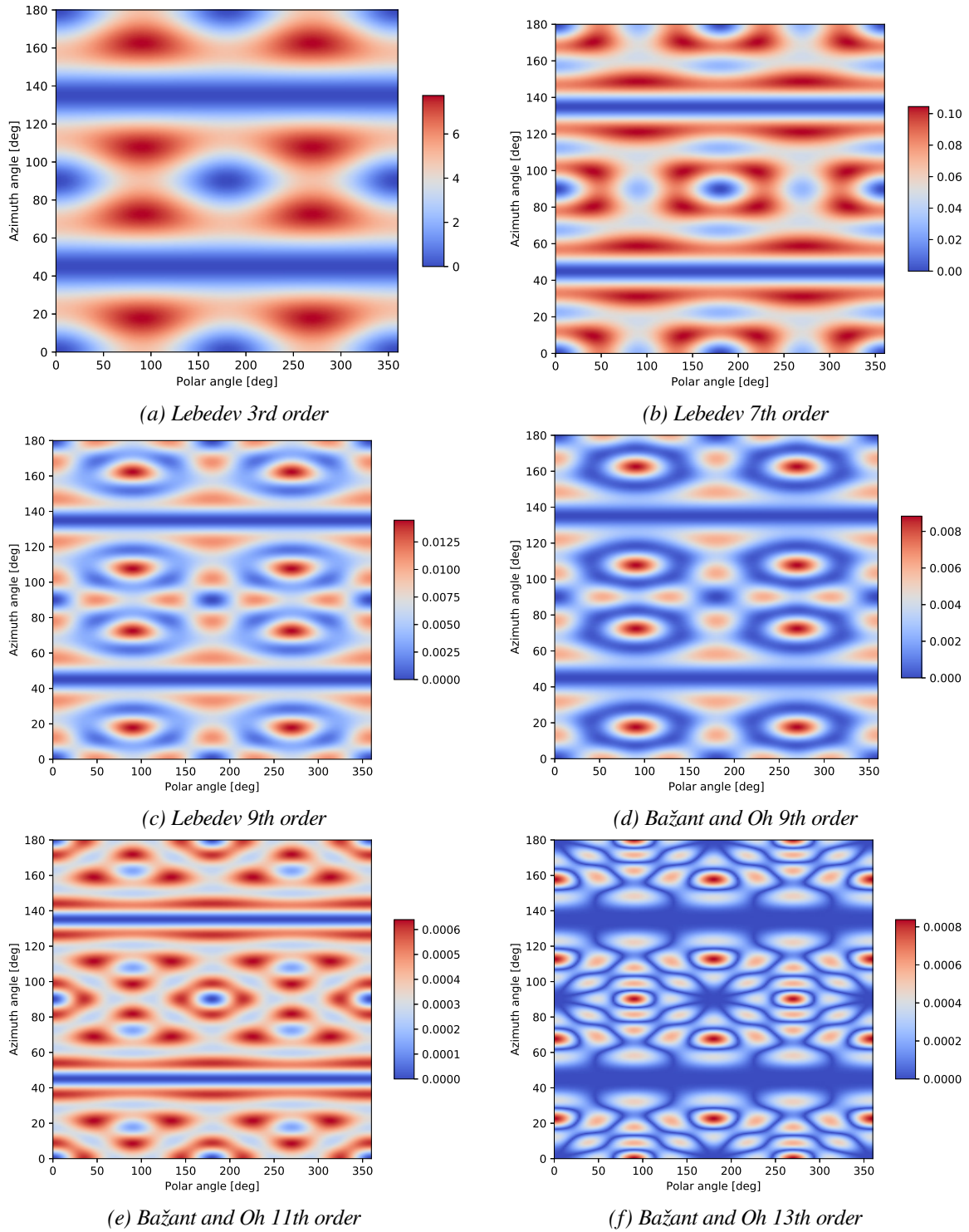
Figure C.7: Percentage error of integration schemes with respect to the reference solution under rotational transformations and equibiaxial loading to $\lambda = 5$

(a) Tetrahedron scheme

(b) Octahedron scheme

(c) Cube scheme

(d) Icosahedron scheme

(e) Dodecahedron scheme
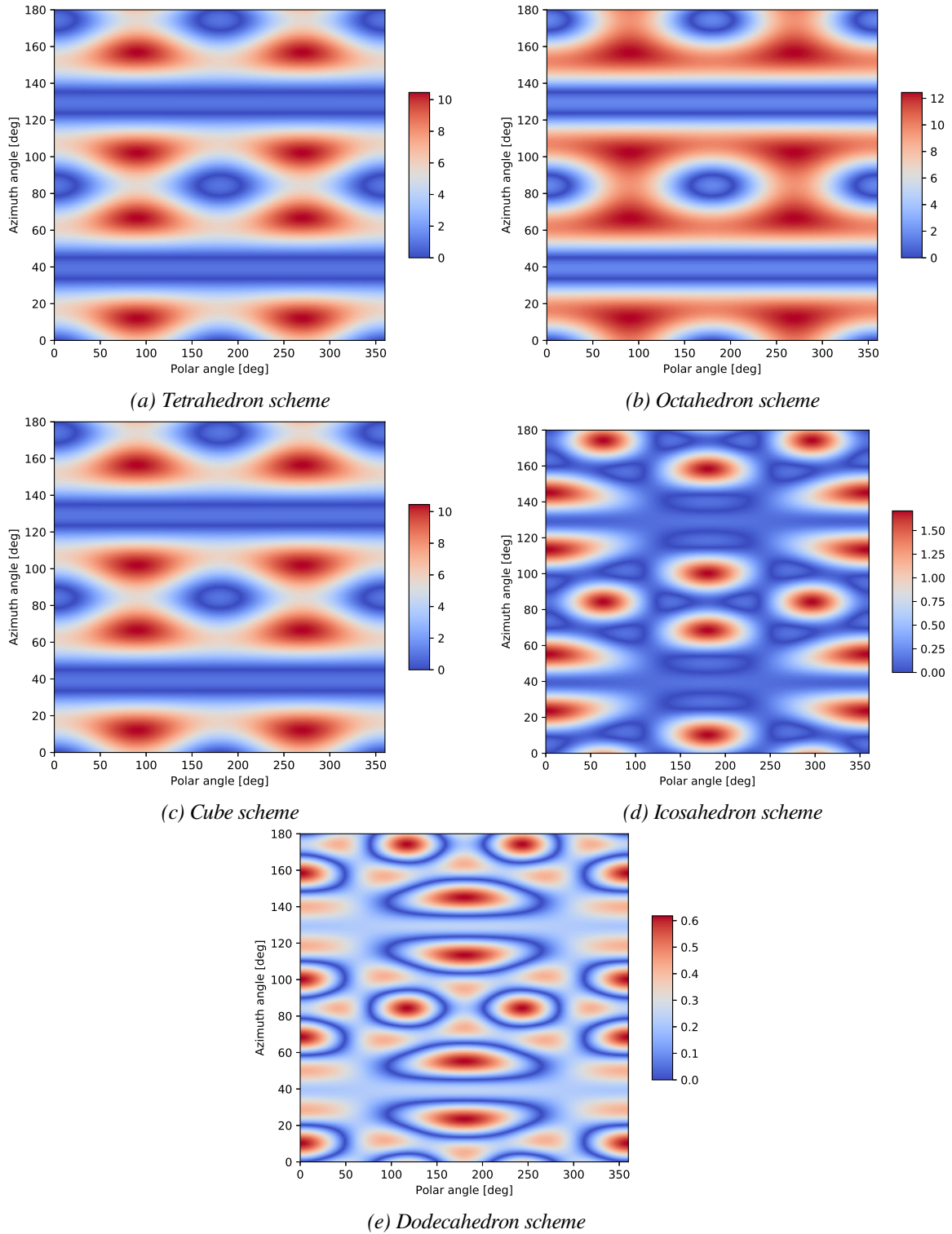
Figure C.8: Percentage error of the platonic integration schemes with respect to the reference solution under rotational transformations and shear loading to $\lambda = 5$
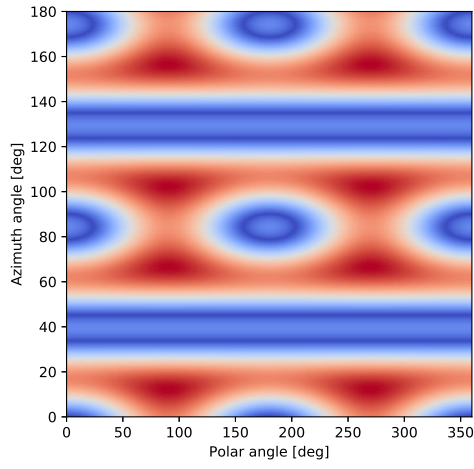
(a) Lebedev 3rd order
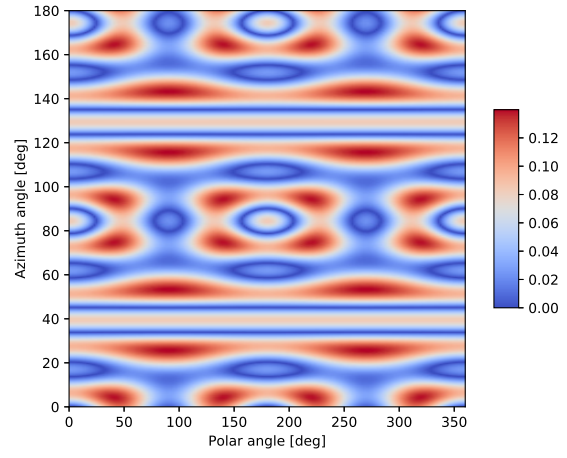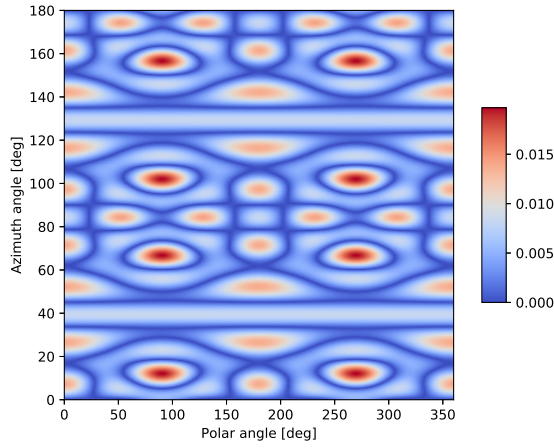
(b) Lebedev 7th order

(c) Lebedev 9th order
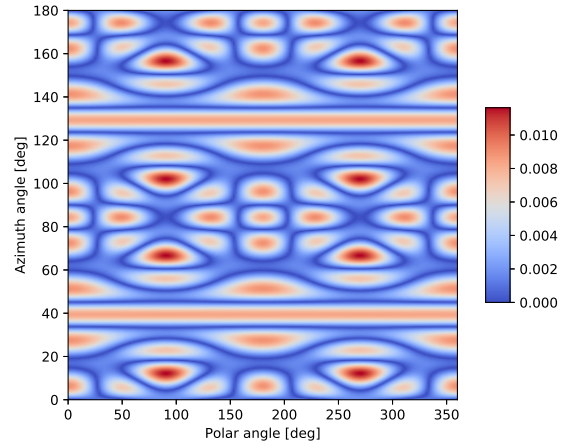
(d) Bažant and Oh 9th order
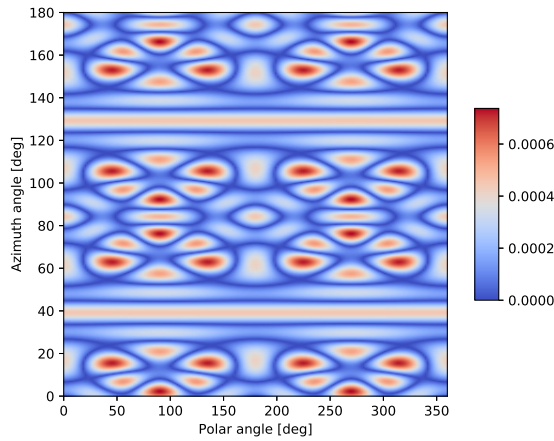
(e) Bažant and Oh 11th order
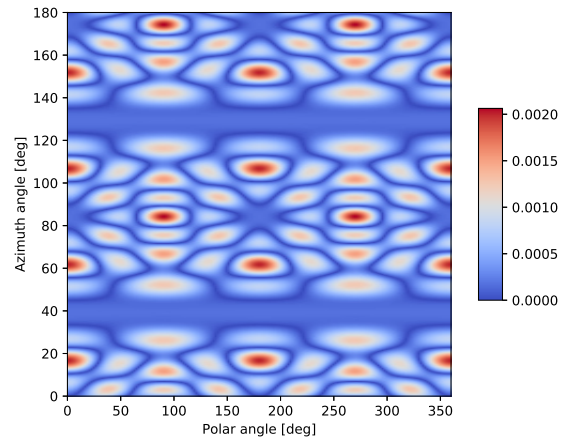
(f) Bažant and Oh 13th order

Figure C.9: Percentage error of integration schemes with respect to the reference solution under rotational transformations and shear loading to $\lambda = 5$

Appendix D

Linearisation of network dynamics

The implicit Euler technique requires the solution of a non-linear set of equation in order to find the updated value at the next time step. Consider the first order differential equation

$$\dot{u}(t) = f(u(t), t) , \tag{D.1}$$

and its implicit Euler discretisation

$$\frac{u_{t+1} - u_t}{\Delta t} = f(u_{t+1}, t+1) \tag{D.2}$$

or alternatively

$$u_{t+1} = \Delta t \, f(u_{t+1}, t+1) + u_t . \tag{D.3}$$

The residual r of the discretised form is given by

$$r = u_{t+1} - u_t - \Delta t \, f(u_{t+1}, t+1) = 0 \tag{D.4}$$

where u_{t+1} is treated as the unknown. The Newton-Raphson method can now be used to find the root for this equation and thereby finding u_{t+1}. Extending this approach to multiple dimensions is straight forward and provides a vector-valued residual

$$\boldsymbol{r} = \boldsymbol{u}_{t+1} - \boldsymbol{u}_t - \Delta t f(\boldsymbol{u}_{t+1}, t+1) = \boldsymbol{0} . \tag{D.5}$$

Performing a linearisation about $\boldsymbol{u}_{t+1}$ and neglecting higher order terms returns

$$\boldsymbol{r}_{t+1} = \boldsymbol{r}_t + \frac{\partial \boldsymbol{r}_t}{\partial \boldsymbol{u}} \Delta \boldsymbol{u} + O(\Delta \boldsymbol{u}^2) = \boldsymbol{0} \tag{D.6}$$

which results in the linear system

$$\frac{\partial \boldsymbol{r}_t}{\partial \boldsymbol{u}} \Delta \boldsymbol{u} = -\boldsymbol{r}_t \tag{D.7}$$

which can be solved iteratively to obtain a converged value for $\boldsymbol{u}_{t+1}$. The Jacobian is denoted as

$$\boldsymbol{A} = \frac{\partial \boldsymbol{r}_t}{\partial \boldsymbol{u}} \tag{D.8}$$

and must be well defined, i.e. $\det \boldsymbol{A} \geq 0$ for an inverse to exist such that the linear system has a solution.

For the discretisation of the network equations using the implicit Euler technique, the Jacobian needs to be formulated and evaluated at each iteration. This was performed with the symbolic algebra package `sympy` in python.

The residual is represented by

$$\boldsymbol{r}_t = \begin{bmatrix} r_1 \\ r_2 \\ r_3 \\ r_4 \end{bmatrix} , \tag{D.9}$$

where each term is given by (D.16) to (D.19) and the components of the Jacobian

$$\boldsymbol{A} = \begin{bmatrix} a_{11} & a_{12} & a_{13} & a_{14} \\ a_{21} & a_{22} & a_{23} & a_{24} \\ a_{31} & a_{32} & a_{33} & a_{34} \\ a_{41} & a_{42} & a_{43} & a_{44} \end{bmatrix} , \tag{D.10}$$

are given in (D.20) through to (D.35). The Jacobian serves another purpose in the stability analysis of these equations. For a stable solution to exist, the Jacobian must emit positive eigenvalues for the given material parameters. While this analysis is omitted here, it should be performed to gauge the validity of the differential equations for a given set of material parameters. To simplify the expressions for the residual and the Jacobian given by

$$\Delta n_a = n_a^{l+1} - n_a^l \tag{D.11}$$

$$\Delta n_{ia} = n_{ia}^{l+1} - n_{ia}^l \tag{D.12}$$

$$\Delta N_a = N_a^{l+1} - N_a^l \tag{D.13}$$

$$\Delta N_{ia} = N_{ia}^{l+1} - N_{ia}^l \tag{D.14}$$

where l is the previous time step and $l + 1$ is the next time step. If no index is given, it is assumed that is it is evaluated at $l + 1$. Common expressions were extracted and are provided (where applicable) before the simplified expression in the format

$$[(x_0, \text{expression})], [\text{simplified expression}] , \tag{D.15}$$

and should be read as 'substitute x_0 with expression in the simplifiedexpression'.

$$r_1 = \Delta t \left(-2n_a^{l+1} p_c \left(N_a^{l+1} + \frac{t\Delta N_a}{\Delta t} \right) e^{-N_a^{l+1} p_c t} + n_a^{l+1} p_s \left(N_a^{l+1} + \frac{t\Delta N_a}{\Delta t} \right) \right) + \Delta n_a$$

$$e^{-N_a^{l+1} p_s t} - n_{ia}^{l+1} p_c \left(N_{ia}^{l+1} + \frac{t\Delta N_{ia}}{\Delta t} \right) e^{-N_{ia}^{l+1} p_c t} \right) + \Delta n_a \tag{D.16}$$

$$r_2 = \left(-2n_a p_s \left(N_a \Delta t + t\Delta N_a \right) e^{N_{ia} t(p_c + p_s)} + n_{ia} \left(N_{ia}\Delta t + t \left(N_{ia} - N_{ia}^l \right) \right) \right.$$

$$\left. \left(2p_c e^{N_{ia} p_s t} - p_s e^{N_{ia} p_c t} \right) e^{N_a p_s t} + \left(n_{ia} - n_{ia}^l \right) e^{t(N_a p_s + N_{ia} p_c + N_{ia} p_s)} \right) e^{-t(N_a p_s + N_{ia} p_c + N_{ia} p_s)} \tag{D.17}$$

$$r_3 = 2N_a^2 p_c t e^{-N_a p_c t} + 2N_a^2 p_c \Delta t e^{-N_a p_c t} - 2N_a N_a^l p_c t e^{-N_a p_c t} + \frac{N_a N_{ia}^l n_{ia} p_c t e^{-N_{ia} p_c t}}{n_a}$$

$$- \frac{N_a N_{ia}^l n_{ia} p_c t e^{-N_{ia} p_c t}}{n_a} - \frac{2N_{ia}^2 n_{ia} p_c \Delta t e^{-N_{ia} p_c t}}{n_a} + \frac{2N_a N_{ia}^l n_{ia} p_c t e^{-N_{ia} p_c t}}{n_a} \tag{D.18}$$

$$r_4 = - \frac{N_a^2 n_a p_s t e^{-N_a p_s t}}{n_{ia}} - \frac{N_a^2 n_a p_s \Delta t e^{-N_a p_s t}}{n_{ia}} + \frac{N_a N_a^l n_a p_s t e^{-N_a p_s t}}{n_{ia}}$$

$$- \frac{N_a^2 n_a p_s \Delta t e^{-N_a p_s t}}{n_{ia}} - \frac{2N_a N_{ia} n_a p_s \Delta t e^{-N_a p_s t}}{n_{ia}} + \frac{2N_a N_{ia} n_a p_s t e^{-N_a p_s t}}{n_{ia}}$$

$$- \frac{2N_a N_{ia} n_a p_s \Delta t e^{-N_a p_s t}}{n_{ia}} + N_{ia}^2 p_s t e^{-N_{ia} p_s t} + N_{ia}^2 p_s \Delta t e^{-N_{ia} p_s t} - N_{ia} N_{ia}^l p_s t e^{-N_{ia} p_s t} + N_{ia} - N_{ia}^l \cdot , \tag{D.19}$$

$$\frac{\mathrm{d}r_1}{\mathrm{d}n_a} = a_{11} = ([[(x_0, \quad N_a t), \quad (x_1, \quad x_0(p_c + p_s)), \quad (x_2, \quad N_a\Delta t + t\Delta N_a)], \quad [(-2p_c x_2 e^{p_s x_0} + p_s x_2 e^{p_c x_0} + e^{x_1}) e^{-x_1}]) \tag{D.20}$$

$$\frac{\mathrm{d}r_1}{\mathrm{d}n_{ia}} = a_{12} = -p_c \left(N_{ia}\Delta t + t\Delta N_{ia} \right) e^{-N_{ia} p_c t} \tag{D.21}$$

$$\frac{\mathrm{d}r_1}{\mathrm{d}N_a} = a_{13} = ([[(x_0, \quad N_a t), \quad (x_1, \quad t(N_a\Delta t + t\Delta N_a))],$$

$$\left[n_a \left(2p_c (p_c x_1 - t - \Delta t) e^{p_s x_0} + p_s (-p_s x_1 + t + \Delta t) e^{p_c x_0} \right) e^{-x_0(p_c + p_s)} \right]]) \tag{D.22}$$

$$\frac{\mathrm{d}r_1}{\mathrm{d}N_{ia}} = a_{14} = ([[(x_0, \quad p_c t)], \quad [n_{ia} p_c (-t - \Delta t + x_0 (N_{ia}\Delta t + t\Delta N_{ia})) e^{-N_{ia} x_0}]) , \tag{D.23}$$

112

$$\frac{\mathrm{d}r_2}{\mathrm{d}n_a} = a_{21} = -2p_s\left(N_a\Delta t + t\Delta N_a\right)e^{-N_a p_s t} \tag{D.24}$$

$$\frac{\mathrm{d}r_2}{\mathrm{d}n_{ia}} = a_{22} = ([(x_0,\quad N_{ia}t),\quad (x_1,\quad x_0\left(p_c+p_s\right)),\quad (x_2,\quad N_{ia}\Delta t + t\Delta N_{ia})], \tag{D.25}$$

$$\left[\left(2p_c x_2 e^{p_s x_0} - p_s x_2 e^{p_c x_0} + e^{x_1}\right)e^{-x_1}\right])$$

$$\frac{\mathrm{d}r_2}{\mathrm{d}N_a} = a_{23} = ([(x_0,\quad p_s t)],\quad [2n_a p_s\left(-t-\Delta t + x_0\left(N_a\Delta t + t\Delta N_a\right)\right)e^{-N_a x_0}]) \tag{D.26}$$

$$\frac{\mathrm{d}r_2}{\mathrm{d}N_{ia}} = a_{24} = ([(x_1,\quad t\left(N_{ia}\Delta t + t\Delta N_{ia}\right)),\quad (x_2,\quad t+\Delta t)], \tag{D.27}$$

$$\left[n_{ia}\left(2p_c\left(-p_c x_1 + x_2\right)e^{p_s N_{ia}t} - p_s\left(-p_s x_1 + x_2\right)e^{p_c N_{ia}t}\right)e^{-N_{ia}t(p_c+p_s)}\right]),$$

$$\frac{\mathrm{d}r_3}{\mathrm{d}n_a} = a_{31} = \left(\left[(x_0,\quad N_a N_{ia}),\quad (x_1,\quad N_{ia}^l t),\quad (x_2,\quad 2N_{ia}^2)\right],\right. \tag{D.28}$$

$$\left.\left[-\frac{n_{ia}p_c\left(-N_a x_1 + 2N_{ia}x_1 + tx_0 - tx_2 + \Delta t x_0 - \Delta t x_2\right)e^{-N_{ia}p_c t}}{n_a^2}\right]\right)$$

$$\frac{\mathrm{d}r_3}{\mathrm{d}n_{ia}} = a_{32} = \frac{p_c\left(N_a - 2N_{ia}\right)\left(N_{ia}\Delta t + t\Delta N_{ia}\right)e^{-N_{ia}p_c t}}{n_a} \tag{D.29}$$

$$\frac{\mathrm{d}r_3}{\mathrm{d}N_a} = a_{33} = ([(x_0,\quad p_c t),\quad (x_1,\quad N_a x_0),\quad (x_2,\quad e^{-x_1}),\quad (x_3,\quad 4x_2),\quad (x_4,\quad p_c\Delta t),\quad (x_5,\quad 2x_2), \tag{D.30}$$

$$(x_6,\quad N_a^l x_5),\quad (x_7,\quad N_{ia}x_0),\quad \left(x_8,\quad \frac{n_{ia}e^{-x_7}}{n_a}\right),\quad (x_9,\quad p_c^2),\quad (x_{10},\quad t^2 x_9),\quad (x_{11},\quad N_a^2 x_5)\Big],$$

$$\left[N_a x_{10}x_6 + N_a x_3 x_4 + N_{ia}x_4 x_8 - N_{ia}^l x_0 x_8 - t\Delta t x_{11}x_9 - x_0 x_6 + x_1 x_3 - x_{10}x_{11} + x_7 x_8 + 1\right]\right)$$

$$\frac{\mathrm{d}r_3}{\mathrm{d}N_{ia}} = a_{34} = ([(x_0,\quad p_c t),\quad (x_1,\quad N_{ia}\Delta t),\quad (x_2,\quad 2N_{ia}),\quad (x_3,\quad t\Delta N_{ia}),\quad (x_4,\quad x_0\left(x_1+x_3\right))], \tag{D.31}$$

$$\left[\frac{n_{ia}p_c\left(-N_a\left(-t-\Delta t + x_4\right) - 2x_1 + x_2 x_4 - x_2\left(t+\Delta t\right) - 2x_3\right)e^{-N_{ia}x_0}}{n_a}\right]),$$

$$\frac{\mathrm{d}r_4}{\mathrm{d}n_a} = a_{41} = \frac{p_s\left(-N_a + 2N_{ia}\right)\left(N_a\Delta t + t\Delta N_a\right)e^{-N_a p_s t}}{n_{ia}} \tag{D.32}$$

$$\frac{\mathrm{d}r_4}{\mathrm{d}n_{ia}} = a_{42} = \left(\left[\left[(x_0,\ N_a t),\ (x_1,\ N_a^2),\ (x_2,\ 2N_{ia})\right],\right.$$
$$\left.\left[\frac{n_a p_s\left(-N_a\Delta t x_2 + N_a^l t x_2 - N_a^l t x_0 + t x_1 + \Delta t x_1 - x_0 x_2\right)e^{-p_s x_0}}{n_{ia}^2}\right]\right) \tag{D.33}$$

$$\frac{\mathrm{d}r_4}{\mathrm{d}N_a} = a_{43} = \left(\left[\left[(x_0,\ p_s t),\ (x_1,\ N_a\Delta t),\ (x_2,\ t\Delta N_a),\ (x_3,\ x_0\left(x_1+x_2\right))\right],\right.$$
$$\left.\left[\frac{n_a p_s\left(N_a x_3 - N_a\left(t+\Delta t\right) - 2N_{ia}\left(-t-\Delta t + x_3\right) - x_1 - x_2\right)e^{-N_a x_0}}{n_{ia}}\right]\right) \tag{D.34}$$

$$\frac{\mathrm{d}r_4}{\mathrm{d}N_{ia}} = a_{44} = \left(\left[\left[(x_0,\ p_s t),\ (x_1,\ N_{ia}x_0),\ (x_2,\ e^{-x_1}),\ (x_3,\ 2x_2),\ (x_4,\ p_s\Delta t),\right.\right.$$
$$\left.\left.(x_5,\ N_{ia}^l x_2),(x_6,\ p_s^2),\ (x_7,\ t^2 x_6),\ (x_8,\ N_a x_0),\ \left(x_9,\ \frac{2n_a e^{-x_8}}{n_{ia}}\right),\ (x_{10},\ N_{ia}^2 x_2)\right],\right.$$
$$\left.\left[N_a x_4 x_9 - N_a^l x_0 x_9 + N_{ia}x_3 x_4 + N_{ia}x_5 x_7 - t\Delta t x_{10}x_6 - x_0 x_5 + x_1 x_3 - x_{10}x_7 + x_8 x_9 + 1\right]\right]\right). \tag{D.35}$$